MASARYK UNIVERSITY

Faculty of Science

Vlastimil Křápek

Excitonic structure of absorption edge in quantum dots

Doctoral thesis

Supervisor: Prof. RNDr. Josef Humlíček, CSc.

Brno 2008

Bibliographic data

Name and surname of the author:	Mgr. Vlastimil Křápek
Title of the doctoral thesis in English:	Excitonic structure of absorption edge in quantum dots
Title of the doctoral thesis in Czech:	Excitonová struktura absorpční hrany kvantových teček
Study program:	Physics
Study branch:	Solid state physics
Supervisor:	Prof. RNDr. Josef Humlíček, CSc.
Year of the defence:	2008
Keywords in English:	quantum dots, theory, photoluminescence, magneto-luminescence, III-V semiconductors
Keywords in Czech:	kvantové tečky, teorie, fotoluminiscence, magnetolu-miniscence, polovodiče III-V

© Vlastimil Křápek, Masaryk University (Brno, Czech Republic), 2008.

Acknowledgements

I would like to express my thanks to all people who supported me during my doctoral studies, namely to:

- Prof. Josef Humlíček for guidance and steady support during my work on this thesis, as well as for arranging contacts with my collaborators. His preference of quality over quantity is a source of inspiration for me. Not least I appreciate that he gave me a freedom to find my own way.
- Doc. Dominik Munzar for introduction to the field of nanoscience. He was the first who gave me real scientific papers to read and was always ready to answer my questions.
- Dr. Eduard Hulicius for kind invitation at Institute of Physics in Praha. He also recommended me my first scientific meeting in Jaszowiec and encouraged me to write a grant proposal.
- Dr. Alice Hospodková for cooperation on vertically stacked dots, her enthusiasm and ideas; this all while looking after three children.
- Dr. Karla Kuldová for magnetophotoluminescence spectra and taking me to Grenoble High Magnetic Field Laboratory. I also enjoyed our joint preparation of a manuscript in five nights.
- Dr. Jiří Oswald for photoluminescence measurements and stimulative discussions.
- Jiří Pangrác and Karel Melichar for sample growth.
- Prof. Dieter Bimberg for kind hospitality during my stay at TU Berlin. He supported my work on elongated dots although he was convinced that there is nothing like an elongated dot (as well as a flying dot, by the way).
- Dr. Andrei Schliwa for introduction to TUB computer code, python scripts, valuable discussions, and improvement of my social life in Berlin. He also believe that there *is* something like an elongated dot (contrary to a flying dot).
- Ondřej Caha for meaningful usage of my strain-field code and drinking a huge amount of beer, Adam Dubroka for reviewing first three chapters and more (and this 'more' is more important, in fact), Jiří Chaloupka for sharing his postscript knowledge, Milan Orlita for his shady (yet helpful) acquaintances, Olga Zrzavecká (that one with variable first surname) for AFM scans and her skeptic nature.
- Last but not least to many people who helped me by just being here. In particular to those of them who are not here anymore.

Abstrakt

Tato dizertační práce si klade dva cíle: (i) vyvinout teoretický model popisující elektronovou strukturu a optické vlastnosti kvantových teček a (ii) aplikovat jej na některá zajímavá témata z oblasti fyziky kvantových teček.

Jako vhodná teoretická metoda pro popis kvantových teček byla zvolena metoda efektivní hmotnosti, která představuje rozumný kompromis mezi nároky na přesnost a úplnost popisu na straně jedné a jednoduchost, srozumitelnost výsledků a rychlost výpočtů na straně druhé. V jejím rámci jsem vyvinul metodu aproximativní separace proměnných, která umožňuje numericky nenáročné nalezení vlnových funkcí a energií vázaných stavů v plochých kvantových tečkách libovolného tvaru. Dále byla pro několik důležitých charakteristických tvarů teček (kužel, čočka, válec) implementována variační metoda řešení Schrödingerovy rovnice, která poskytuje přesnější výsledky za cenu pomalejších výpočtů a menší obecnosti metody. Obě metody poskytují kvalitativně správné výsledky a s ohledem na omezenou znalost strukturních parametrů jsou vhodné pro vysvětlení experimentálních dat. Pro srovnání byla použita implementace osmipásové k.p teorie vyvinutá na Technische Universität Berlin.

Důležitým cílem technologie kvantových teček je dosažení dlouhovlnné luminiscence v kvantových tečkách InAs/GaAs, konkrétně komunikačních vlnových délek 1.3 μm a 1.55 μm. K tomuto účelu lze použít vícevrstvé systémy kvantových teček. K červenému posunu luminiscence dochází jednak díky rozprostření vlnové funkce přes tečky ve všech vrstvách, jednak kvůli ovlivnění růstu horních teček spodními – tečky ve vyšších vrstvách jsou větší. Srovnáním experimentu s modelem určujeme podíl těchto faktorů na červeném posunu (u objemu dále rozlišujeme zvětšení laterálních a vertikálních rozměrů) pro různé tloušťky oddělovací vrstvy a počet vrstev v systému.

Velkých hodnot vlnových délek luminiscence lze dosáhnout také překrytím teček ternární vrstvou InGaAs snižující elastické napětí. Uplatní se přitom vliv nižšího elastického napětí na polohy energiových pásů, snížení potenciálové bariéry ze strany ternární vrstvy a zvětšení objemu teček vlivem nižšího napětí a odlišného chemického složení při růstu krycí vrstvy. Srovnáním experimentu s modelem opět určujeme význam jednotlivých faktorů.

V poslední části se věnujeme magnetooptickým vlastnostem kvantových teček. Diskutujeme vliv strukturních vlastností teček a možnost stanovit tvar z naměřených magnetooptických spekter. Ukazujeme citlivost spekter na laterální protažení vlnových funkcí, které může souviset s laterálním protažením teček nebo s piezoelektrickým polem.

Abstract

The goal of the thesis is twofold: (i) to develop a theoretical model describing electronic structure and optical properties of quantum dots, and (ii) to apply it to some interesting topics of the quantum dot physics.

Effective mass theory was chosen as the appropriate theoretical method for a description of quantum dots, which represents a reasonable trade-off between accuracy and completeness on the one hand, and simplicity, easy interpretation of results and short calculation time on the other hand. In the framework of this approach I have developed a method of approximate variable separation, which enables a numerically simple retrieval of wave functions and energies of bound states in flat quantum dots of arbitrary shape. For a set of important characteristic quantum dot shapes (cone, lens, cylinder), I further implemented a variational method of solution of the Schrödinger equation, which gives more accurate results at the price of slower calculations and lower generality. Both methods provide qualitatively correct results and, regarding limited knowledge of quantum dot structure, are suitable for the interpretation of experimental data. An implementation of eight band $\vec{k} \cdot \vec{p}$ theory developed at Technische Universität Berlin was used for comparison.

An important goal of quantum dot technology is to achieve long wavelength luminescence from InAs/GaAs quantum dots, namely communication wavelengths of $1.3\,\mu$m and $1.55\,\mu$m. Multilayer quantum dot systems may be used for this purpose. The red shift is caused by the wave function extension over the dots in the stack, and by the influence of the lower layer to the upper dot layer growth – the dots in upper layers are usually larger. Comparing experimental data with our model, we determine the proportion of these factors in contributing to the red shift (differentiating further between the increased lateral or vertical dimensions for the case of increased volume) for various values of the spacer layer thickness and number of layers in the system.

Long luminescence wavelengths can also be achieved by using ternary InGaAs strain-reducing capping layers. The red shift is due to a lower strain influencing the band energies, lower potential barrier on the capping layer side, and increased dot volume due to modified strain and chemical composition during the growth of the capping layer. Comparing experimental data with the model results, we again determine the importance of the factors mentioned above.

The last part of the thesis is dedicated to magneto-optical properties of quantum dots. We discuss the effect of structural properties on the magnetooptical properties and a possibility to determine the shape of the dots from measured magnetooptical spectra. We demonstrate a fair sensitivity of the spectra to the lateral elongation of the wave functions, which may be connected with lateral elongation of the quantum dots or with piezoelectric fields.

Contents

1 Introduction **9**
- 1.1 Unique properties of quantum dots . . . 10
- 1.2 Growth . . . 12
- 1.3 Structural characterization . . . 13
- 1.4 Optical characterization . . . 14
- 1.5 Selected applications . . . 14

2 Modeling of quantum dots **18**
- 2.1 k.p theory . . . 19
- 2.2 Envelope function theory . . . 23
- 2.3 Strain . . . 25
  - 2.3.1 Valence force field model . . . 25
  - 2.3.2 Continuum elasticity model . . . 27
  - 2.3.3 Impact on the electronic structure . . . 28
- 2.4 Piezoelectric field . . . 29
- 2.5 Magnetic field . . . 31
- 2.6 Few-particle states: Configuration interaction method . . . 32

3 Implementation and basic properties of the models **34**
- 3.1 Strain field . . . 35
  - 3.1.1 Implementation of Valence force field model . . . 35
  - 3.1.2 Implementation of Continuum elasticity model . . . 42
  - 3.1.3 Comparison of both models . . . 49
- 3.2 Variable thickness well approximation . . . 50
- 3.3 Variational method . . . 66
- 3.4 Eight band k.p model developed at TU Berlin . . . 74

4 Vertically stacked quantum dots **77**
- 4.1 Introduction . . . 77
- 4.2 Experimental data . . . 78
- 4.3 Electronic states . . . 81
- 4.4 Interpretation of measurements . . . 84
- 4.5 Conclusions . . . 86

5 InGaAs strain reducing layer **87**
5.1 Introduction . . . 87
5.2 Experimental results . . . 87
5.3 Interpretation of measurements . . . 89
5.4 Conclusions . . . 93

6 Magnetooptical properties of quantum dots **94**
6.1 Elongation of InAs/GaAs quantum dots . . . 95
6.1.1 Introduction . . . 95
6.1.2 Theory . . . 96
6.1.3 Experiment . . . 100
6.1.4 Results and discussion . . . 101
6.1.5 Conclusions . . . 109
6.2 Interrelation of structural and magnetooptical properties . . . 109
6.2.1 Magnetooptical properties in general . . . 111
6.2.2 Exciton in magnetic field . . . 113
6.2.3 Lateral elongation . . . 114
6.2.4 Other structural parameters . . . 119
6.2.5 Effect of piezoelectric field . . . 125
6.2.6 Conclusions . . . 128

Summary **129**

Outlook **131**

List of publications **140**

Chapter 1

Introduction

Quantum dots (QDs) are nano-sized heterostructures, i.e., small islands of one material embedded in a matrix composed by another material with different chemical composition. The size of the dots is comparable with de Broglie wavelength of electrons in all three directions; this leads to the quantization of the electron motion and discrete energy levels, strongly depending on the shape and size of the dots. Such structures provide unique properties, they are interesting from both fundamental physics and application point of view. Since the first preparation of coherent quantum dots [1, 2, 3] a considerable effort is continuously devoted to this subject.

The thesis is organized as follows: In this chapter we provide a short general introduction to the field of QDs. Chapter 2 deals with the theoretical modeling: $\vec{k} \cdot \vec{p}$ theory and envelope function theory are derived, influence of the strain field, piezoelectric field, and external magnetic field is added to the model, and configuration interaction method is presented. Two numeric implementations of general theoretical approaches are subject of Chapter 3: a simple but efficient variable-thickness-well approximation and a more complex variational method, both based on single-band envelope function theory. Likewise an eight-band envelope function theory based model developed at Technische Universität Berlin is briefly described in Chapter 3, although it was not developed within this thesis; however, it was used for some calculations. Elementary properties of the models are compared. Subsequent chapters are devoted to the explanation of optical experiments carried out on InAs/GaAs MOVPE prepared quantum dot systems. Chapter 4 deals with vertically stacked quantum dots. The aim of the stacking is the reduction of transition energies to the values suitable for communications, i.e., 0.95 eV and 0.80 eV (1.30 μm and 1.55 μm, respectively). Comparing photoluminescence (PL) measurements and theoretical prediction, we identify the factors leading to the PL red shift (wave function spreading and dot enlargement) and their proportion. In the following Chapter 5 the dots capped by ternary InGaAs capping layers are studied. Analogous to the vertical stacking, the ternary capping decreases the transition energies and allows to reach the communication energies. We determine the factors leading to the PL red shift (strain relaxation, dot enlargement, confinement decrease) and their proportion from the comparison of optical measurements and a theoretical modelling. The last part of this thesis, Chapter 6, is devoted to the interrelation of the structural and magnetooptical properties of quantum dots. We discuss the influence of the shape and size of quantum dots to the transition energies and their shifts in external magnetic field; particular interest is devoted to the effect of the lateral elongation, vertical profile, and squareness of the bases. We also discuss the possibil-

ity to retrieve the shape from the magnetooptical measurement. For a number of samples the lateral elongation of quantum dots has been determined from the magnetophotoluminescence measurements. Comparing this elongation with the values measured by atomic force microscopy on the reference uncapped samples provides an important insight into the shape modification due to the capping process.

1.1 Unique properties of quantum dots

Discrete energy spectrum The size of the dots is comparable with de Broglie wave length of electrons in all three directions; this leads to the quantization of the electron motion and discrete energy levels, depending strongly on the shape and size of the dots. The most prominent property of QDs is undoubtedly their discrete energy spectrum. It even gave rise to the denomination of quantum dots as "artificial atoms"; however, unlike atoms, quantum dots offer many advantageous properties, such as defined position, possibility to build QD molecules or even arrays with diverse lay-out, possibility to add contacts and produce electronic devices, etc.

The density of states in a single dot has a δ-like character, which is favorable for applications requiring high and narrow density of states, such as lasers.

Carrier localization The energy quantization is closely connected with the localization of carriers in the dot. The Coulomb interaction of the charge carriers is heavily enhanced in comparison with the bulk. The complexes, such as excitons, biexcitons and trions, exist even at elevated temperatures. The carrier localization is also used in so-called modulation doping, which allows spatial separation of dopants and excessive charge carriers, decreasing their scattering rate.

Size dependent properties Important feature of quantum dots is the size dependence of their properties. Parameters such as lowest transition energy or carrier lifetime can thus be tuned in a wide range of values. For example, InAs/GaAs QDs with the lowest PL band between 0.9 and 1.3 eV were reported at low temperatures [4, 5]. Furthermore a modification of the chemical composition (ternary or quaternary materials) can be used for tailoring of desired properties.

Strain Typical quantum dots prepared by self-organization are, as a matter of fact, heavily strained. For example, the lattice mismatch between InAs and GaAs is approximately 7 %; the strain in the dots is slightly lowered since the strain relaxation is the driving force for the dot creation by means of self-organization, but still close to 7 %. The corresponding stress exceeds the fracture limit of the bulk material, such a large strain can therefore exist only in nanosized structures, where the strain energy per dot is smaller than the activation energy of dislocation. The large strain is accompanied by a fairly high piezoelectric field in heterostructures composed of polar material.

The strain present around the dots is favorable for the preparation of the vertical quantum dot molecules. When a multilayer quantum dot system is grown, the strain distribution leads to the stacking of dots from the subsequent layer directly on the top of dots of the preceding layer.

Inhomogeneity Many experiments performed on quantum dots and many related devices employ dot ensembles rather than a single dot. It is important to notice that the dots in the ensemble are not identical due to the stochastic nature of the growth, they exhibit a random distribution of sizes and shapes. The δ-like density of states of single dot transforms to the bands, which are often well described by Gaussians with a typical width of several tens meV. Some applications such as lasers require rather narrow bands, while for others (e.g., memories based on a spectral hole burning) broad bands are preferable.

Device temperature stability The discrete energy spectrum leads to an improvement of the temperature stability of the devices such as semiconductor lasers. The properties of bulk semiconductor lasers depend on temperature. The charge carriers populate energy bands of a width comparable with the thermal energy; Consequently, the luminescence efficiency decreases and the threshold current increases roughly exponentially as the temperature increases, which is unfavorable for the laser operation. In quantum dots, the first excited level is separated from the ground level by the energy higher than the thermal energy at fairly high temperatures, resulting in the negligible population of the excited levels. The quantum dot based semiconductor lasers therefore exhibit a good temperature stability and can easily operate at room temperature [6, 7, 8].

Coulomb blockade effect A very peculiar transport feature, called Coulomb blockade, is related to the Coulomb interaction of particles in dots. Consider a metallic dot connected to two metallic electrodes, denoted as source and drain. The dot is separated from the electrodes by insulator layers, sufficiently thin to allow the tunneling between the dot and the electrodes but thick enough that it is plausible to consider the charge on the dot quantized in multiples of the elementary charge. The transport through the system requires a transfer of a single electron from the source to the dot, followed by the transfer of a single electron from the dot to the drain, or vice versa, extraction of a single electron to the drain followed by the insertion of a single electron from the source. The dot can be described as capacitor with the capacity C related to its dimension; for a spherical dot of the diameter R embedded in a dielectric with the relative permitivity ϵ_r, the capacity is determined by the relation $C = 4\pi\epsilon_0\epsilon_r R$, where ϵ_0 is the vacuum permitivity. Both extraction and insertion of a single electron from/to electrically neutral dot increases the energy of the system by the charging energy $E_C = e^2/2C$. Using $\epsilon_r = 10$, E_C exceeds for $R < 1\,\mu$m the thermal energy at 4 K and for $R < 2.8$ nm at room temperature (300 K). It means that the charge transport through the system is suppressed by the charging energy at sufficiently low temperature. If we apply a bias voltage to the system, the current remains zero until certain threshold voltage U_{th} is reached ($U_{th} = e/C$ for symmetric leads), which just compensates the charging energy. Above the threshold, the current increases as the voltage increases.

A single electron transistor is formed after adding a gate electrode to the system. Its principle can be described in a very simple way. Application of a gate voltage leads to a charging of the dot with a charge Q. Mathematically, Q may be any real number, but in fact the charge in the dot has to be an integer multiple of the elementary charge e. When the ratio Q/e is integer, the tunneling is suppressed by the Coulomb barrier E_C and the Coulomb blockade takes place. When it is an integer plus one half $(N + 1/2)$, the energies for N and $N + 1$ electrons are degenerate and non-zero tunneling current occurs even for very low bias

voltage. The first experimental realization of the single electron transistor has been reported by Fulton and Dolan [9].

If the dot is small enough the space quantization energy has to be taken into account as well; this applies particularly to the devices operating at the room temperature.

The unique properties described above, as well as many others, make quantum dots a popular topic of contemporary semiconductor research.

1.2 Growth

A large variety of approaches has been used to prepare quantum dots. Various lithographic methods provide dots suitable for the measurements of transport properties [10], selective substrate etching is used to create strain-free AlAs/GaAs dots [11, 12]. The dots studied in this work have been prepared by self-organization [13, 14]. This elegant, efficient and widely used technique is based on the competition between strain and surface energy of a thin layer (formed e.g. by InAs) deposited on a substrate with lower lattice parameter (e.g. GaAs). If the thickness of the layer exceeds a critical value, which is 1.7 monolayer (ML) for InAs layer on GaAs substrate, the layer roughens and forms small islands – quantum dots. Increased surface energy of the dots is compensated by the strain relaxation. The possibility to create semiconductor islands by self-organization was discussed in papers of Stranski and Krastanow in 1937 [13], the preparation of coherent (defect free) quantum dots was reported for the first time in 1993 by several groups [1, 2, 3].

Molecular Beam Epitaxy (MBE) and Metal-Organic Vapor Phase Epitaxy (MOVPE) are most extensively used methods for the deposition of the thin layer. In case of MBE, the heated substrate is placed in ultra high vacuum chamber. Effusive Knudsen cells are filled in with high purity elements, such as indium and arsenic, and their openings directed towards the substrate. The cells are heated, the material evaporates, flows towards the substrate and is adsorbed, forming the thin layer. The advantages of MBE consist in high material purity and abrupt interfaces; the main disadvantage is rather low growth rate, which influences industrial applications. High vacuum enables in-situ monitoring of the growth using methods such as reflection high-energy electron diffraction (RHEED) and other.

MOVPE reactors contain a holder with heated substrate. The carrier gas (usually hydrogen) passes through the bubblers with metal-organic precursors (e.g., trimethyl-gallium or trimethyl-indium). Group V components are often introduced in the form of hydrides, such as arsine. Precursors react with hydrides at the heated substrate, producing a semiconductor (e.g. InAs) and an alkane gas (e.g. methane). The quality of the samples resembles MBE and the growth rate is higher. The main disadvantage is a serious hazard related to handling the highly toxic hydrides. The in-situ monitoring is not as convenient as for the MBE, but still possible; reflection anisotropy spectroscopy (RAS) is used for this purpose [15, 16].

The shape and size of the islands formed on the top of thin layer is dependent on many parameters, such as the thickness of the thin layer, the temperature of the substrate, the growth speed, the partial pressure of reactants in case of MOVPE, and the growth interruption after the layer deposition, which is usually introduced to facilitate the dot formation [14]. Another important issue is the growth of the capping layer. The dots for most of the applications have to be capped by several tens nanometer layer of (usually substrate) material to prevent the contact of the electrons and holes with surface of the sample, which would lead to the fast

non-radiative surface recombination. Songmuang et al. reports a drastic change in the dot shape (lateral elongation and a decrease of the height) during the growth of capping layer [17]. However, as we demonstrate in this work, the elongation is related to the surface profile only, the underlying dot is not involved [18, 19]. The decrease of the height is accompanied by a blueshift of transition energies, which is undesirable for some applications involving lasers for communications. We demonstrate a favorable effect of ternary capping to the blueshift [20].

1.3 Structural characterization

As already mentioned, the properties of quantum dots are strongly dependent on their shape and size [21]; good knowledge of them is therefore essential. Optical methods cannot provide such information due to a small size of the dots in comparison with the wavelength of light. X-ray based methods provide useful information on the chemical composition and strain field [22]. However, they suffer from the small dot volume and inhomogeneity of the dot ensembles; using of strong x-ray intensities provided by synchrotron radiation and homogeneous dots with aligned positions [23, 24] are therefore advantageous. Shape and size of a single dot, as well as some other parameters, can be retrieved using transmission electron microscopy (TEM) or some of the scanning probe microscopy (SPM) techniques, such as atomic force microscopy (AFM) or scanning tunneling microscopy (STM).

Transmission electron microscopy employs a beam of accelerated electrons with energy up to 200 keV directed onto the sample. Transmitted electrons provide information on the chemical composition and strain in single dots with the resolution reaching atomic level. The critical issue of the measurements is the sample preparation; it has to be thinned to the thickness of several tens of nanometer. Both plan-view [25] and cross-section [26] imaging is possible. Careful analysis of the experimental data allows to distinguish between the strain and chemical contrast. The advantage of the method over SPM is its capability to display the dots covered by the capping layer [27, 28]. However, the measurements are very demanding.

Atomic force microscopy [29] uses a sharp tip mounted on a flexible cantilever. The tip is moved to close proximity to the sample, where it experiences atomic and molecular forces (e.g., van der Waals force). These forces cause deflection of the cantilever, which is monitored optically using a laser reflected from a small mirror attached to the cantilever. Moving the tip over the sample, it is possible to retrieve the profile of the surface. The sensitivity to the chemical composition is lacking in comparison with TEM or STM. The resolution is restricted by the tip diameter, it reaches subatomic scale vertically and about 10 nm laterally (although the atomic lateral resolution has been reported for a special experimental setup). The method is suitable for plan-view imaging; the main disadvantage consists in limitations in measuring capped dots [18, 19]. Scanning tunneling microscopy (see [30, 31] for the description of the technique and [32, 33] for recent applications to quantum dot systems) is similar to AFM; the metal tip is biased and the measured quantity is the tunneling current between the tip and conducting sample. Since the tunneling current is extremely sensitive to the width of the barrier, the spatial sensitivity of the method is extremely good, better than atomic laterally and several hundredths of nanometer vertically. Both plan-view and cross-section imaging is possible. Furthermore it is possible to measure the current-voltage characteristics at each tip position; this so-called scanning tunneling spectroscopy is capable to image the wave functions of bound states in the dots [34, 35].

1.4 Optical characterization

Optical measurements play an important role in the characterization of quantum dots due to a direct access to their electronic structure. The most frequently used method is photoluminescence (PL) together with its modifications such as photoluminescence excitation spectroscopy (PLE), micro-photoluminescence (μ-PL), magnetophotoluminescence (MPL), and time-resolved photoluminescence. Other methods used in QDs characterization are absorption spectroscopy and cathodoluminescence (CL).

Photoluminescence set-up is very simple: the sample is illuminated by the beam of excitation light; its photon energy has to be higher than the lowest transition energy in QD. The valence electrons are excited to the conduction states, leaving holes in the valence states. The excited electrons (holes) usually decay non-radiatively to the ground electron (hole) state. Here they can recombine radiatively, emitting a photon with the energy corresponding to the lowest exciton energy in quantum dot. The main drawback of the method is that it provides information on the energies only, it is not suited for the determination of the oscillator strength due to a very complex carrier dynamics involved. Usually the lowest transition energy is measured, but also higher transitions are achievable in case of high excitation power, when the lower transitions are saturated. The method is used on QDs ensembles, single dots can be studied by means of μ-PL.

PLE is a modification of the standard PL: the intensity of emission is recorded as a function of the excitation energy, while the detection energy is held fixed. The method provides the information on the higher transitions.

Measurements on single dots are performed using μ-PL. This method is not basically different from the ordinary PL; the only difference is that the luminescence light is collected from a small number of dots only. This is often achieved using a shadow mask with small apertures. The aperture diameter less than 100 nm is usually sufficient to obtain spectrum with distinguished transitions from different dots. Another possibility involves the use of near field.

Photoluminescence in external magnetic field is used to study the influence of the field to the exciton properties. The influence of electric field is usually studied by means of electroluminescence – the quantum dot layer is sandwiched in p-i-n structure and the light is generated by an injection of electrons and holes via an external current.

Time resolved photoluminescence is used to probe the life time of the excitons. It employs a pulse excitation and a time resolved detection.

Transmission measurements provide an insight into the oscillatory strength and also to the excited transitions. These measurements are not used very often due to demanding sample preparation.

Cathodoluminescence uses STM setup to generate excited electrons in quantum dots. This method offers an excellent spatial resolution, allowing to probe single dots. Another advantage is that by varying the tip-sample bias, it is possible to probe charged exciton complexes (trions).

1.5 Selected applications

Numerous promising applications were proposed based on nanosized heterostructures in general, and on quantum dots in particular (see e.g. [21, 36, 37] and references therein). They

involve an improvement of existing devices as well as a design of novel applications which are not available using standard materials. Quantum wells and layered materials are presently widely used in industry. Lasers in DVD drives, magnetic storage media with huge capacities, resistance standard used in metrology, and many others are based on two-dimensional systems. Not least several Nobel prizes were awarded to researchers in this field – Esaki in 1973 for tunneling phenomena in semiconductors, von Klitzing in 1985 for quantized Hall effect, Alferov and Krömer in 2002 for developing semiconductor heterostructures used in high-speed- and opto-electronics, and Fert and Grünberg in 2007 for Giant Magnetoresistance. On the other hand, applications based on quantum dots are often at the level of laboratory operation; their industrial exploitation is hindered mainly by the technologically demanding preparation. Steady intensive research shall also here lead to many prominent industrial applications, not omitting lasers, qubits, single electron transistors or single photon on-demand sources. In the following paragraphs we present some of the applications.

Modulation doping Scattering by ionized impurities limits the carrier mobility in semiconductor material at low temperatures. This can be worked around by using the modulation doping, first proposed by Störmer [38]. The idea consists in a spatial separation of ionized impurities from the active part of the semiconductor, while the charge carriers are transported to the active part. The realization is indeed very simple. Two materials, which have almost identical lattice parameters but different band gaps are brought together to form a heterojunction. The material with the larger gap is doped with shallow impurities (donors or acceptors). After the ionization of impurities, the excessive charge carriers relax into the lower gap material, reducing thus their energy. The transferred charge results in an electric field, which subsequently confines the charge carriers in two-dimensional potential well formed at the lower-gap side of the heterojunction. Since the charge carriers are separated from the ionized impurities, they are only weakly scattered by them. Using this method carrier mobilities exceeding $10^6\,\mathrm{cm}^2.\mathrm{V}^{-1}.\mathrm{s}^{-1}$ have been achieved in GaAs at low temperatures.

Persistent spectral hole burning memory This device uses inhomogeneous broadening of quantum dots to store a lot of information to a small volume. The idea was proposed by Muto [39]. The storage medium is an ensemble of quantum dots with a large inhomogeneous broadening. Writing is realized by a spectrally sensitive photoexcitation pulse. The pulse creates an electron-hole pair in those dots, whose lowest transition energy is equal to the photon energy of radiation used for the excitation. The electrons are subsequently extracted from the system in order to prevent the recombination. This is ensured for example by inserting the dots inside a Schottky contact, where the built-in electric field causes the tunneling of the excited electrons out of the dot. The reading is carried out by applying a radiation pulse and measuring a photoinduced current, which depends on the presence of the hole, i.e., on the stored information. Experimental realization of the device was reported by Imamura [40]. It utilizes InAs dots with an inhomogeneous broadening of 73 meV embedded in GaAs matrix incorporated in the Schottky contact. The retention time of the holes was 0.27 ms at room temperature. The memory capacity can be as high as $10\,\mathrm{Tb.cm}^{-2}$ [41], which is indeed a huge number, making the persistent hole burning memories an important for further research and possible applications.

Quantum dot laser Laser is used for a generation of highly coherent collimated intensive light. Two essential parts necessary for the laser operation are the active medium and the optical resonator. The resonator is formed by two parallel mirrors, one of them semi-transparent. A waveguide can be formed by coating the walls of the resonator by a low refraction index material in order to increase the performance. The light propagates through the active medium inside the resonator, where it undergoes absorption and stimulated emission. The stimulated emission rate has to be larger than the absorption rate in order to amplify the light; this is not possible if the system is in thermal equilibrium. The lasing takes place between two levels, for which a population inversion is achieved, i.e., the high-energy level occupation is higher than the low-energy level occupation. This is ensured by the external power source, which pumps the electrons to the excited level. Very often a light source is used for the pumping, either incoherent or another laser, but in case of semiconductor lasers (i.e. with semiconducting active medium) the electric pumping prevails. The active medium is embedded in a p-n junction and pumped by an electric current; electrons (holes) inserted into the active medium relax to the upper (lower) lasing level. The advantage of the semiconductor lasers is small dimensions and easy integration into the semiconductor electronic devices.

Quantum dot laser is a type of semiconductor laser which employs the dots as the active medium. Intriguing properties of such a device have been predicted theoretically in early 1980s [42, 43]: ultralow threshold current, extremely good temperature stability, and narrow spectral linewidth are expected as a consequence of a high material and differential gain, which are caused by the discrete density of states. The material gain g_{mat} is defined as a relative amplification of the light intensity per unit distance (it is an analogue of absorption coefficient, differing only in the sign) and it depends on pumping current j. The optical wave propagating through the waveguide overlaps only partly with the quantum dots, we therefore introduce the modal gain as $g_{mod} = \Gamma g_{mat}$, where the optical confinement factor Γ is approximately equal to the ratio of the total dot volume and the total waveguide volume. In order to achieve the lasing, the modal gain has to overcome the losses caused by the scattering of the light in the waveguide and mirror losses. The lowest pumping current for which this happens is referred to as a threshold current j_{th}. The temperature dependence of the threshold current is approximately described by an exponential, $j_{th}(T) = j_{th}(T_1)\exp[(T - T_1)/T_0]$, introducing the characteristic temperature T_0. High values of T_0 are required in order to achieve a good performance at room temperature.

There are two facts which make the quantum dot laser so promising. First, the gain is proportional to the joint density of states on the lasing energy, which is extremely high in quantum dots. Consequently the gain is high for a given pumping current, and the threshold current is therefore low. Second, virtually all charge carriers inserted into the active layers reach the lasing levels. The energy separation between these and higher energy levels prevents thermal evaporation of the carriers and notably improves the temperature stability of the device.

It is evident that a fundamental requirement for a real quantum dot laser is a homogeneous quantum dot ensemble; the inhomogeneous broadening of the density of states deteriorates their performance. The first realization of quantum dot laser has been reported in 1994 [44]. Since then a considerable progress has been achieved (see the review [45] and the references therein). In particular, ultralow threshold current density ($6\,\mathrm{A.cm^{-2}}$ per QD sheet) and high internal quantum efficiency of 98 % have been achieved for a triple-sheet laser at $1.15\,\mu$m. Output power of 12 W corresponded to a power density of $18\,\mathrm{MW.cm^{-2}}$ [46, 47]. Long wavelength lasers at $1.3\,\mu$m with a threshold current density of $40\,\mathrm{A.cm^{-2}}$, 5 W output power

for the 100 μm stripe and 300 mW output power for the 7 μm stripe edge emitters, and large T_0-values of 150 K up to 50 °C have been reported, as well as 1.5 μm edge emitting lasers with a reasonable threshold current density of the order of 1 kA.cm^{-2} [48, 49]. Also the dynamic properties of the quantum dot lasers are very interesting.

From the construction point of view the quantum dot laser does not differ substantially from the other types, some peculiarities are related to its nanoscopic/mesoscopic character. The structure itself is usually prepared using an epitaxial method (most often MBE or MOVPE) and consists of several layers. The lasers can be divided into edge-emitting (light propagates parallel with the layers) and surface-emitting (light propagates along the growth direction). In the following we concern the edge-emitting laser. On the top of the substrate (e.g. GaAs) a buffer layer is grown epitaxially in order to increase the structural quality. Afterwards the lower cladding layer, active region, and upper cladding layer are grown. Cladding layers have lower refractive index than the active region and their purpose is to create the optical waveguide and to confine the optical wave around the active region. Typical thickness of the cladding layers is of the order of light wavelength. The active region can contain several sheets of QDs in order to increase the active volume; the number is limited by the strain. The upper cladding layer is usually covered by some capping layer preventing the cladding degradation. The layers below and above the active region are doped with opposite type of dopants in order to create a p-n junction, which allows the electric pumping. The active layer itself is composed of intrinsic semiconductors. Metallic electrodes are attached to the top and bottom of the structure. Optical resonator is fabricated simply by the cleavage of facets, which have reflectivities of about 30 % for GaAs and InP based devices. With a high reflection coating values of 99 % or higher can be achieved [21].

For the surface emitting laser the resonator length is extremely short (below 1 μm), the losses at the mirrors are dominant. High reflectivity mirrors are therefore required, realized by distributed Bragg reflectors, each composed of about 20 periods of a multilayer, often AlAs/GaAs. The active region is sandwiched between the mirrors, cladding layers are not used. First quantum dot based vertical cavity surface emitting laser has been reported by Saito in 1996 [50].

Chapter 2

Modeling of quantum dots

In this section we review thoroughly several possible approaches to modeling of the electronic structure and optical properties of QDs.

A typical dot contains from thousands to hundreds of thousands atoms. Moreover, the wave function extends to a host material, which has to be included in the modeling. The problem is therefore very demanding and with no doubt we have to start the solution of Schrödinger equation by introducing adiabatic approximation and single electron approximation.

The problem is still too complex to be solved by traditional methods of computational physics, such as local density approximation or Hartree-Fock method. However, there exist some works which stop doing approximations at this stage and solve the problem using semi-empirical pseudopotential [51, 52, 53, 54, 55] or tight binding approach [56, 57, 58]. The fundamentals of both of these methods are described in introductory solid state physics textbooks [36], their adaption for QD systems in corresponding research papers; the detailed description is beyond the scope of this thesis. Both these methods deal with atomistic nature of quantum dots; their predictive power is, in principle, superior to less exact methods. However, their vast complexity prevents their extensive applications.

In this work, as well as in most other works, another approach is used. It is quite easy to retrieve the band structure of crystalline materials because of the benefit of translational symmetry. This symmetry is lifted in heterostructures; however, it is reasonable to assume that the crystalline properties of the constituents of the heterostructure are somehow included in the properties of the heterostructure itself. This is the idea behind the envelope function theory: the particles in bulk crystal are considered "free", the periodic potential is embedded in (energy dependent) effective mass of the particle. The wave function is a product of the free-particle plane wave and a periodic part of Bloch wave. In the heterostructure a potential well is formed by band edges of the heterostructure constituents; the wave functions of effective particles in this well are called envelope functions, the wave functions of real particles are constructed as a product of the envelope function and the periodic part of Bloch wave. The envelope function method was compared to the pseudopotential calculations ([52, 53]; several differences were found, e.g., in band gaps or lateral anisotropy) and a technique of "linear combination of bulk bands" which produces results similar to a full direct diagonalization pseudopotential calculation, at a cost comparable to the envelope function method. On the other hand, the differences are not very significant if the uncertainty of quantum dot structure and composition is taken into account, which is always present when experimental data are

modeled. Thus, the simplicity of multiband envelope function method and the fair quality of the results imply its extensive application in the QD modeling.

In Sec. 2.1, we introduce the $\vec{k} \cdot \vec{p}$ theory, a corner-stone of the envelope function theory. Section 2.2 provides a derivation of the envelope function theory. We proceed by incorporating the effect of the strain (Sec. 2.3), piezoelectric field (Sec. 2.4), and external magnetic field (Sec. 2.5) into the envelope function theory. In Sec 2.6 we describe configuration interaction method, which is used to construct few-particle excitations (excitons, biexcitons, trions, etc.) from the single particle states.

2.1 k.p theory

In this section we derive the $\vec{k} \cdot \vec{p}$ theory. It was originally developed to describe the band structure of a crystal in a vicinity of a given k-vector $\vec{k}_0$. When $\vec{k}_0$ is set to the Γ-point, a convenient description of the absorption edge of direct band-gap semiconductors is possible. The importance of the method for quantum dots description consists in its close connection to the envelope function theory.

We consider an ideal crystal with translational symmetry. Within the framework of single particle approximation, the energy structure is described by the Schrödinger equation

$$\left[-\frac{\hbar^2}{2m_0}\nabla^2 + V(\vec{r})\right]\psi(\vec{r}) = E\psi(r), \tag{2.1}$$

where the effective potential $V(\vec{r})$ is periodic, i.e.,

$$V(\vec{r} + \vec{R}_m) = V(\vec{r}) \tag{2.2}$$

for each lattice vector $\vec{R}_m$.

A concrete form of the periodic effective potential $V(\vec{r})$ is not important; the final Hamiltonian contains several parameters, which are fitted to the measured band structure instead of calculating them. In other words, $\vec{k} \cdot \vec{p}$ theory belongs to the semi-empirical methods.

According to the Bloch theorem, the wave functions have a form of Bloch waves,

$$\psi(\vec{r}) = \exp(i\vec{k}\vec{r})u_{n\vec{k}}(\vec{r}), \tag{2.3}$$

where $u_{n\vec{k}}$ is a periodic part of the Bloch wave (referred to as u-function below),

$$u_{n\vec{k}}(\vec{r}) = u_{n\vec{k}}(\vec{r} + \vec{R}_m), \tag{2.4}$$

and $\vec{k}$ fulfils the Born-Karmán periodic boundary conditions. Inserting 2.3 into 2.1, we obtain the equation for the u-function $u_{n\vec{k}}$:

$$\left[-\frac{\hbar^2}{2m_0}\nabla^2 + \frac{\hbar}{m_0}\vec{k}.\vec{p} + \frac{\hbar^2 k^2}{2m_0} + V(\vec{r})\right]u_{n\vec{k}}(\vec{r}) = E_n(\vec{k})u_{n\vec{k}}(\vec{r}). \tag{2.5}$$

In this equation $\vec{p} = -i\hbar\nabla$ denotes the momentum operator to illustrate the origin of the name $\vec{k} \cdot \vec{p}$ theory. In the following we set up a k-vector of interest; without loss of generality we choose the Γ-point: $\vec{k}_0 = 0 \equiv \Gamma$. The set of u-functions at Γ-point $\{u_{m0}\}$ is complete on the space of all u-functions; we can therefore expand the solution of 2.5 as the series

$$u_{n\vec{k}} = \sum_m c_{nm\vec{k}} u_{m\Gamma}. \tag{2.6}$$

We insert the expansion 2.6 into Equation 2.5, multiply by $u^*_{l\Gamma}$, and integrate over the unit cell volume. Using the orthogonality of the set $\{u_{m\Gamma}\}$ and the relation

$$\left[-\frac{\hbar^2}{2m_0}\nabla^2 + V(\vec{r})\right] u_{n\Gamma}(\vec{r}) = E_n(\Gamma) u_{n\Gamma}(\vec{r}), \tag{2.7}$$

we finally obtain the set of equations for the coefficients $c_{nm\vec{k}}$:

$$\sum_m H_{lm}(\vec{k}) c_{nm\vec{k}} = E_n(\vec{k}) c_{nl\vec{k}}, \tag{2.8}$$

where the matrix elements of the Hamiltonian are

$$H_{lm}(\vec{k}) = \left[E_m(\Gamma) + \frac{\hbar^2}{2m_0}\right]\delta_{lm} + \frac{\hbar}{m_0}\vec{k}\langle u_{l\Gamma}|\vec{p}|u_{m\Gamma}\rangle. \tag{2.9}$$

Heretofore, no approximation beyond the single electron approximation has been used. In principle, solving the system 2.8 provides the exact band structure. In practice, however, we have to restrict the expansion 2.6 to a finite set of u-functions. For example, if we are interested in the absorption edge of the semiconductor, we use the valence and conduction bands for the expansions, and eventually some other bands. The more bands we use, the more precise are the results at the cost of the increased calculation complexity. The distant bands can be still included perturbatively.

The $\vec{k}\cdot\vec{p}$ Hamiltonian for the zinc-blende semiconductors was for the first time introduced by Luttinger [59]. The basis consists of six p-type valence u-functions $|Xs\rangle$, $|Ys\rangle$, $|Zs\rangle$, which transform as an atomic orbitals p_x, p_y, p_z respectively under the symmetry operations of the crystal; spin orientation s takes the values $\uparrow$ and $\downarrow$. Due to the symmetry thirty six matrix elements of the Hamiltonian are determined by only three parameters (so-called Luttinger parameters), which can be obtained by fitting the measured band structure. Kane introduced an eight-band Hamiltonian including the conduction band Bloch function $|Ss\rangle$ [60], later on, the effects of the external magnetic field were included by Pidgeon and Brown [61]. The eight-band Hamiltonian describes well the vicinity of Γ-point in direct gap semiconductors. The description of the whole Brillouin zone, or of indirect gap semiconductors, is provided by further extension of the basis to the fourteen-band [62] or even thirty-band model [63].

The eigenfunctions of the eight band $\vec{k}\cdot\vec{p}$ Hamiltonian at the Γ point are given in Table 2.1 [64]. The Hamiltonian in the basis of eigenfunctions $\{u_1, \cdots, u_8\}$ reads (only upper triangle of the Hermitian matrix is given)

$$H_{8kp} = \begin{pmatrix} E_{EL} & -\sqrt{2}P_z & P_z & \sqrt{3}P_+ & 0 & -P_- & -\sqrt{2}P_- & 0 \\ & E_{LH} & G_1 & \sqrt{2}G_+ & P_+^+ & 0 & -\sqrt{3}G_- & G_2 \\ & & E_{SO} & -G_+ & \sqrt{2}P_+^+ & \sqrt{3}G_- & 0 & \sqrt{2}G_2 \\ & & & E_{HH} & 0 & -G_2 & -\sqrt{2}G_2 & 0 \\ & & & & E_{EL} & -\sqrt{2}P_z & P_z & \sqrt{3}P_- \\ & & & & & E_{LH} & G_1 & \sqrt{2}G_- \\ & & & & & & E_{SO} & -G_- \\ & & & & & & & E_{HH} \end{pmatrix}. \tag{2.10}$$

labelling	name	$\|j, m_j\rangle$	energy	expansion
u_1	electrons	$\|1/2, 1/2\rangle$	E_g	$\|S\uparrow\rangle$
u_2	light holes	$\|3/2, 1/2\rangle$	0	$(\|(X+iY)\downarrow\rangle - 2\|Z\uparrow\rangle)/\sqrt{6}$
u_3	so-splitted h.	$\|1/2, 1/2\rangle$	$-\Delta$	$(\|(X+iY)\downarrow\rangle + \|Z\uparrow\rangle)/\sqrt{3}$
u_4	heavy holes	$\|3/2, 3/2\rangle$	0	$\|(X+iY)\uparrow\rangle/\sqrt{2}$
u_5	electrons	$\|1/2, -1/2\rangle$	E_g	$\|S\downarrow\rangle$
u_6	light holes	$\|3/2, -1/2\rangle$	0	$(-\|(X-iY)\uparrow\rangle - 2\|Z\downarrow\rangle)/\sqrt{6}$
u_7	so-splitted h.	$\|1/2, -1/2\rangle$	$-\Delta$	$(-\|(X-iY)\uparrow\rangle + \|Z\downarrow\rangle)/\sqrt{3}$
u_8	heavy holes	$\|3/2, -3/2\rangle$	0	$\|(X-iY)\downarrow\rangle/\sqrt{2}$

Table 2.1: The eigenfunctions of the eight band $\vec{k}\cdot\vec{p}$ Hamiltonian at the Γ point. j and m_j denotes the total angular momentum of the carrier and its projection along the z-axis, respectively. The energy is counted from the top of the valence band, E_g is the band gap, Δ is the spin-orbit split-off energy. The last column indicates coordinates of the eigenfunctions in the Kane basis. After Eppenga [64].

Here the following notation is used:

$$\begin{gathered}
E_{EL} = E_g + s\tilde{e}, \quad E_{LH} = -\gamma_1\tilde{e} - \gamma_2\tilde{e}_1, \quad E_{SO} = -\Delta - \gamma_1\tilde{e}, \quad E_{LH} = -\gamma_1\tilde{e} + \gamma_2\tilde{e}_1, \\
\tilde{e} = \hbar^2/(2m_0)(k_x^2+k_y^2+k_z^2), \quad \tilde{e}_1 = \hbar^2/(2m_0)(2k_x^2-k_x^2+k_y^2), \quad e_2 = \hbar^2/(2m_0)(k_x^2-k_y^2), \\
P_z = \sqrt{1/3}(iPk_z + Bk_xk_y), \quad P_\pm = \sqrt{1/6}[iP(k_x \pm ik_y) + Bk_z(k_y \pm ik_x)], \\
G_1 = \sqrt{2}\gamma_2\tilde{e}_1, \quad G_2 = -\sqrt{3}\gamma_2 e_2 + i2\sqrt{3}\gamma 3k_xk_y, \quad G_\pm = \sqrt{6}\gamma_3 k_z(k_x \pm ik_y),
\end{gathered} \tag{2.11}$$

and $P = -i\langle S|p_x|X\rangle$ is the matrix element of the momentum component, which is sometimes substituted by the energy $E_P = (2m_0/\hbar^2)P^2$. The superscript + denotes Hermitian conjugation (which is actually complex conjugation for this Hamiltonian; however, later on we will replace the k-components by operators). The energy is counted from the top of the valence band, E_g is a band gap, Δ is a spin-orbit split-off energy.

The terms in Hamiltonian have the following meaning: the terms linear in k-vector describe the coupling between the conduction and three valence bands, whose strength is determined by the parameter P. These terms originate in the $\vec{k}\cdot\vec{p}$ term of the Hamiltonian matrix elements (2.9). No direct interaction between the three valence bands is present due to symmetry. The influence of the distant bands, included perturbatively, is expressed by the terms quadratic in k-vector. Its strength is determined by the parameter s for the conduction band, and modified Luttinger parameters γ_1, γ_2, γ_3 for the valence bands. B is Kane parameter describing the inversion asymmetry.

We further discuss the determination of the parameters of the Hamiltonian (2.10). The energies E_g and Δ are obtained directly from the Γ-point band energies and the coupling parameters P, s, γ_1, γ_2, γ_3 can be obtained from the Γ-point effective masses (details are given in [64]). This setting provides a good description of the band structure in the vicinity of Γ-point; however, in some cases a good coincidence of the model and band structure at distant parts of the Brillouin zone may be required and therefore different parameters setting may be used. The parameter sets used in this thesis are given in the appropriate sections. We note that B is usually set to 0 and many authors use $s = 1$.

It should be noted that Hamiltonian 2.10 is given in various forms by different authors; the differences are mainly in the order of vectors in the basis 2.1 or their signs.

The $\vec{k}\cdot\vec{p}$ theory provides a useful formula for the effective mass m_{eff}. Consider n-th band having an extreme at Γ-point, we expand the energy nearby this point into a Taylor series up to the second order:

$$E_n(\vec{k}) = E_n(\Gamma) + \frac{\hbar^2}{2m_0} \sum_{i,j\in\{x,y,z\}} \left(\frac{1}{m_{eff}}\right)_{ij} k_i k_j. \tag{2.12}$$

On the other hand, it is possible to retrieve the energy $E_n(\vec{k})$ using $\vec{k}\cdot\vec{p}$ theory, where only single band is used for the expansion, including the remaining bands perturbatively. We obtain

$$E_n(\vec{k}) = E_n(\Gamma) + \frac{\hbar^2}{2m_0}\vec{k}^2 + \sum_{m\neq n} \frac{|H_{nm}|^2}{E_n(\Gamma) - E_m(\Gamma)}. \tag{2.13}$$

Comparing (2.12) a (2.13) and using (2.9) for the matrix elements of the Hamiltonian we obtain the formula for the tensor of reciprocal effective mass:

$$\left(\frac{1}{m_{eff}}\right)_{ij} = \delta_{ij} + \frac{2}{m_0} \sum_{m\neq n} \frac{\mathrm{Re}\left[(\vec{i}\vec{p}_{nm})(\vec{j}\vec{p}_{mn})\right]}{E_n(\Gamma) - E_m(\Gamma)}, \tag{2.14}$$

where $\vec{i}, \vec{j}$ are unit vectors in a given direction and p_{ab} are the momentum matrix elements. In particular, using the eight-band k.p approximation we obtain the effective masses of electrons and heavy holes as

$$\begin{aligned}
\frac{1}{m_{el}^{\perp}} &= 1 + \frac{E_P}{3}\left(\frac{2}{E + E_{el} - E_{lh}} + \frac{1}{E + E_{el} - E_{so}}\right), \\
\frac{1}{m_{el}^{\parallel}} &= 1 + \frac{E_P}{6}\left(\frac{3}{E + E_{el} - E_{hh}} + \frac{1}{E + E_{el} - E_{lh}} + \frac{2}{E + E_{el} - E_{so}}\right), \\
\frac{1}{m_{hh}^{\parallel}} &= 1 + \frac{E_P}{3}\left(\frac{2}{E + E_{hh} - E_{el}}\right),
\end{aligned} \tag{2.15}$$

where all effective masses are expressed in units of free electron mass m_0, E is the energy of the bound state of interest, E_n are the band edge energies, the symbols $\perp$ ($\parallel$) denote vertical (lateral) directions, $E_P = 2|P|^2/m_0$, and P is the momentum matrix element between the valence and conduction states at Γ. Since the vertical heavy hole mass, $m_{hh}^{\perp}$, is affected only by remote bands, we assume here a constant value. The meaning of the energy E is as follows. In the bulk semiconductor it is zero. In the heterostructure the bound state is formed with energy exceeding the band minimum energy by some finite value referred to as a confinement energy. Due to the non-parabolicity of the energy dispersion relations this state feels slightly increased effective mass with respect to that in the bottom of the band. This approach corresponds formally to employing the Brillouin–Wigner perturbation series instead of the Rayleigh–Schrödinger perturbation series. Assuming the energy dependent masses slows down the calculations, since an iterative approach to solve the Schrödinger and mass equations has to be applied; on the other hand, we believe the advantage is improved accuracy of energies.

2.2 Envelope function theory

In this section we derive the envelope function theory, which was originally developed to describe the influence of external potential slowly varying in space to the crystal. Although these requirements are not met in the heterostructures (the boundaries of the heterostructure act as a step-like potential), the method proved extremely useful in modeling and it is most frequently used for this purpose.

Let us consider periodic crystalline Hamiltonian H_c with superimposed external potential V_p. The corresponding Schrödinger equation for this case has the following form

$$(H_c + V_p)\psi = E\psi. \tag{2.16}$$

Bloch functions $\phi_{n\vec{k}}$ form a complete set on the space of eigenfunctions and the solution of Equation (2.16) can be expanded into the series

$$\psi(\vec{r}) = \sum_n \int_{1.BZ} \tilde{f}_n(\vec{k})\phi_{n\vec{k}} d\vec{k}. \tag{2.17}$$

We further assume that the expansion contains only Bloch functions from the vicinity of the Γ-point of the k-space. It is then reasonable to assume that the dependence of the Bloch functions on k is given predominantly by the plane wave factor $\exp(i\vec{k}\vec{r})$, while the u-functions $u_{n\vec{k}}$ are only weakly dependent on k, $u_{n\vec{k}} \approx u_{n0}$:

$$\phi_{n\vec{k}} \approx \phi_{n0} \exp(i\vec{k}\vec{r}). \tag{2.18}$$

For simplicity we will further assume that only Bloch functions originating in a single band contribute significantly to the expansion 2.16 of the eigenfunction ψ (single band envelope function approximation). The inclusion of more bands is straightforward but complicates the derivation; the final result will be given below. With these assumptions we write

$$\psi(\vec{r}) \approx \phi_{n0}(\vec{r}) \int_{1.BZ} \tilde{f}(\vec{k}) \exp(i\vec{k}\vec{r}) d\vec{k} = \phi_{n0}(\vec{r}) f(\vec{r}), \tag{2.19}$$

where $f(\vec{r})$ is (except for a constant factor) a Fourier transform of $\tilde{f}(\vec{k})$ called an envelope function. In this approximation, the wave function ψ is therefore formed by a product of a Bloch function at Γ-point and an envelope function.

It remains to find the envelope function. We denote $E_n(\vec{k})$ the eigenenergy of the ideal periodic Hamiltonian H_c. Applying the Hamiltonian to the wave function ψ, we obtain

$$H_c\psi(\vec{r}) \approx \phi_{n0}(\vec{r}) \int_{1.BZ} \tilde{f}(\vec{k}) E_n(\vec{k}) \exp(i\vec{k}\vec{r}) d\vec{k}. \tag{2.20}$$

We further use the relation

$$\int \vec{k}^m \tilde{f}(\vec{k}) \exp(i\vec{k}\vec{r}) d\vec{k} = (-i\nabla)^m f(\vec{r}). \tag{2.21}$$

We expand the band energy dispersion on the right side of (2.20) in a power series in $\vec{k}$,

$$E_n(\vec{k}) = \sum_m a_m \vec{k}^m, \tag{2.22}$$

rewrite the integrals using (2.21), and add the resulting terms. We obtain

$$H_c\psi(\vec{r}) \approx \phi_{n0}(\vec{r})E_n(-i\nabla)f(\vec{r}). \tag{2.23}$$

We further apply the Hamiltonian $H_c + V_p$ to the wave function ψ and after a simplification we obtain the following equation for the envelope function:

$$[E_n(-i\nabla) + V_p(\vec{r})]f(\vec{r}) = Ef(\vec{r}). \tag{2.24}$$

Remember that E denotes the energy corresponding to the wave function ψ in Equation (2.16).

It remains to express appropriately the term $E_n(-i\nabla)$. A full derivation can be found in the work of Bastard [65], here we consider for simplicity a parabolic energy dependence

$$E_n(\vec{k}) = E_0 + \frac{\hbar^2}{2m_{eff}}k^2, \quad E_n(-i\nabla) = E_0 - \frac{\hbar^2}{2m_{eff}}\nabla^2, \tag{2.25}$$

where E_0 denotes the band edge energy and m_{eff} effective mass. We finally obtain the equation for the envelope function

$$\left[-\frac{\hbar^2}{2m_{eff}}\triangle + V_p(\vec{r})\right] f(\vec{r}) = (E - E_0)f(\vec{r}). \tag{2.26}$$

This equation has a straightforward physical interpretation: It is a Schrödinger equation for the particle with the mass m_{eff} in the potential V_p. The influence of the complex crystal potential is neatly hidden in the modified mass and the energy offset E_0.

Multiband envelope function approach has been derived in [65, 66]. It is based on retaining more bands in the expansion (2.17). The solution of (2.16) is assumed in the form

$$\psi(\vec{r}) = \sum_n f_n(\vec{r})u_{n0}(\vec{r}). \tag{2.27}$$

The envelope functions are determined by the set of equations

$$\sum_a [H_{ab} + (V_p)_{ab}]f_a(\vec{r}) = Ef_b(\vec{r}), \tag{2.28}$$

where $(V_p)_{ab}$ are the matrix elements of the additional potential in the basis of included u-functions, and H_{ab} are obtained from (2.9) changing all occurrences of k-vector by the differential operator

$$\vec{k} \to -i\nabla. \tag{2.29}$$

An important issue of operator ordering arises from the spatial dependence of the material parameters (E_P, γ_i, etc.), which do not commute with the operator ∇. Ad-hoc symmetrization rules were suggested by Eppenga [64]. They read

$$P(\vec{r})\partial_i \to \frac{1}{2}\left[P(\vec{r})\partial_i + \partial_i P(\vec{r})\right] \tag{2.30}$$

for linear terms and

$$P(\vec{r})\partial_i\partial_j \to \frac{1}{2}\left[\partial_i P(\vec{r})\partial_j + \partial_j P(\vec{r})\partial_i\right] \tag{2.31}$$

for quadratic terms.

For completeness we add the following note. As we have already noted, the above described envelope function method considers a smooth potential superimposed over the periodic crystal potential. In the heterostructures, this additional potential is formed by the band offsets on the boundaries and is rather steep. A modified envelope function method for the heterostructures was developed by Burt [67, 68]. The model is valid for the steep potential and relies only on the smooth variation of the envelope functions. The main difference in comparison with the standard envelope function model lies in a modified operator ordering. It is actually based on the fact that the whole Hamiltonian is hermitian, but individual matrix elements are not necessarily so, which was disregarded in the conventional approach. The questions related to this topic are discussed thoroughly in the work of Mlinar ([69] and references therein). In this work we refer to a massive application of the conventional envelope function approach in the modeling of quantum dots, yielding very good results, confirmed also by comparisons with superior methods [52], and use the conventional approach.

2.3 Strain

The quantum dots prepared by self-organization are essentially strained due to the lattice mismatch between the constituents of the heterostructure. The knowledge of the strain field is important for the following reasons: (1) It directly influences results of a number of measurements, particularly structural. TEM is directly sensitive to the strain and a separation of the composition and strain contrast has to be based on a good knowledge of the strain field. (2) The strain has a (very significant) impact on the electronic structure and therefore has to be included in any successful modeling. It can be incorporated very easily to the envelope function method – only band edges are shifted, other Hamiltonian parameters are intact. On the other hand, including the strain to the pseudopotential or tight-binding approaches is rather tricky, since it has an impact on the pseudopotential form-factors or tight-binding hopping amplitudes. (3) A shear component of the strain, which is always present in the strained dots, produces a piezoelectric field in polar semiconductors (actually, most of binary semiconductors). The piezoelectric field has an impact on the electronic structure, which is especially pronounced for large, high dots with abrupt interfaces.

In the following, we present two methods for the calculations of the strain and discuss its impact on the electronic structure.

2.3.1 Valence force field model

The valence force field (VFF) model is an atomistic model, in which the strain energy of the crystal is expressed in terms of stretching and bending of the bonds between adjacent atoms (which includes not only the nearest neighbors, but also other close atoms in some models).

A model for diamond-structure crystals, considering the nearest neighbor bonds only, was developed by Keating [70], and later extended for the zinc-blende crystals [71]. The strain energy is expressed as

$$V = \frac{1}{2}\sum_i \left[\frac{1}{4}\sum_{j=1}^{4} \frac{\alpha_{ij}}{\bar{a}_{ij}^2}(\vec{v}_{ij}^2 - 3\bar{a}_{ij}^2)^2 + \frac{1}{2}\sum_{j=1,k>j}^{4} \frac{\beta_{ijk}}{\bar{a}_{ij}\bar{a}_{ik}}(\vec{v}_{ij}\vec{v}_{ik} + \bar{a}_{ij}\bar{a}_{ik})^2 \right], \tag{2.32}$$

where α_{ij}, β_{ijk} are potential constants, $\vec{v}_{ij} \equiv \vec{r}_j - \vec{r}_i$ denotes the vector connecting the ith and the jth atom, $\vec{r}_i$ denotes the position of the ith atom and $4\bar{a}_{ij}$ is the lattice parameter. The

first sum runs over all atoms in the system and the sums over j and k run over the four nearest neighbor atoms. The first term in the expression refers to the bond length change from the strain-free state (bond stretching), the second refers to the change of the angle between bonds (bond bending).

The atom positions are determined by the condition of equilibrium,

$$\frac{\partial V}{\partial \vec{r}_i} = 0, \tag{2.33}$$

which is equivalent to the strain energy minimization. The set of equations (2.33) has to be solved by some iterative method. From the physical point of view, the following instabilities may arise: swapping of the positions of equivalent atoms (this is easily suppressed by the limiting the convergence step size) and drifting of the whole system (suppressed by fixed boundary conditions). The following iterative approach to the solution was suggested in [72]. At the beginning of the simulation, all atoms are placed on the unstrained substrate lattice. Subsequently, we allow atoms to deviate from their position. In each stage, only one atom position is displaced to its equilibrium position with other atoms held fixed. All atoms are displaced in sequence. The whole sequence is repeated until the requested accuracy of the solution is reached.

Keating reported expressions connecting the potential parameters α, β to the elastic compliances as follows [70]:

$$\alpha = (C_{11} + 3C_{12})\bar{a}, \tag{2.34}$$

$$\beta = (C_{11} - C_{12})\bar{a}. \tag{2.35}$$

Since this VFF model uses merely two potential parameters, C_{44} is not independent compliance anymore, but it is fixed to the value

$$C_{44} = \frac{\alpha\beta}{(\alpha + \beta)\bar{a}}. \tag{2.36}$$

The deviation of the real coefficient C_{44} from the value calculated from (2.36) is about 13 % for GaAs and 22 % for InAs. This is a rather serious drawback of the method. As demonstrated by Stier [73], the wrong value of the compliance C_{44} is a main source of the discrepancies between the strain profile in quantum dots calculated by the VFF model and continuum elasticity model; it means that VFF is less accurate than continuum elasticity. Later, Williamson [74] introduced a generalized version of the VFF model in which C_{44} has been reproduced correctly. As noted by Kane [75], the anharmonic terms are not treated correctly in the Keating model, since the elastic parameters are obtained from a linear continuum elasticity model. The correct treatment of the anharmonic terms was subsequently described in a number of works [76, 77]. On the other hand, the contribution of anharmonic terms to the total strain energy is not significant [78] and it is therefore possible to omit them or use the original Keating model without a notable loss of accuracy.

Appropriately designed VFF model is superior to the continuum elasticity model, which assumes slowly varying strain on length scale comparable with inter-atomic distances. The VFF model, on the other hand, treats the steep strain variations on the heterostructure interfaces properly. It is also capable to describe tiny effects connected with the atomic character of matter, such as the symmetry reduction in polar materials [73]. It is undoubtedly the first

choice if the method used for the computation of electronic structure is also atomistic (i.e., pseudopotential or tight binding). However, if a continuum approach, such as envelope function theory, is used for the electronic structure calculations, an atomistic strain model cannot fully unfold its potential. The reason is that during the mapping of the atoms displacement to the strain tensor, which is contained in the continuum Hamiltonian, the information is lost: a unit tetrahedron (e.g., one Ga atom with four As nearest neighbors) is described by 12 atomic displacements (four times three coordinates, taking the central atom as a reference with zero displacement), while the strain tensor contains only 6 independent parameters at each position. Therefore the continuum elasticity model is the optimal choice for the continuum electronic structure model.

2.3.2 Continuum elasticity model

In this model the deformation is described by the displacement field of each elementary volume element from its unstrained position $\vec{u}(\vec{r})$. The strain tensor is defined as

$$\varepsilon_{ij} = \frac{1}{2}\left(\nabla_j u_i + \nabla_i u_j\right),\ i,j \in \{x,y,z\}, \tag{2.37}$$

it is therefore symmetric by definition. The first drawback of the method applied to the heterostructures arises from this description: There is nothing like unstrained state and the displacement definition is a bit confused. There is however an unstrained state for each compound of the heterostructure; the problem remains on the boundaries, which are not, as a matter of fact, treated correctly in the continuum model.

The strain distribution in the heterostructure is determined by the equilibrium condition

$$\sum_{k\in\{x,y,z\}} (\nabla_k \sigma_{jk}) + f_j = 0, \tag{2.38}$$

where

$$\sigma_{jk} = C_{jklm}\varepsilon_{lm} \tag{2.39}$$

are the components of the stress tensor, C_{jklm} are elastic compliances, and f_j are the components of the volume force density. In a material of cubic symmetry, the compliance tensor has only three independent non-zero parameters, which are denoted as follows: $C_{iiii} \equiv C_{11}$, $C_{iijj} \equiv C_{12}$, $C_{ijij} \equiv C_{44}$. Corresponding elastic deformation energy is given by

$$U_{CM} = \frac{1}{2}\sum_{ijkl} C_{ijkl}\varepsilon_{ij}\varepsilon_{kl}. \tag{2.40}$$

The strain field can be obtained by minimizing the deformation energy. The most frequently used methods to do so are the finite element method (FEM) [79] and finite differences method (FDM) [73, 80]. However, these methods are rather time consuming, making them impractical for accurate strain calculation in large dot structures.

Elegant analytical method for calculation of the strain in a periodic array of dots is described in [81]. Its advantage over the FEM and FDM approach is a decreased computational complexity. We describe this method briefly here. The volume force density originates from the lattice mismatch at the boundaries of the dots. It is given by

$$f_j = -F\frac{\partial\Omega(\vec{r})}{\partial x_j},\ F = (C_{11} + 2C_{12})\Delta, \tag{2.41}$$

where $\Omega(\vec{r})$ is the shape function of the dot (1 in the dot volume, 0 otherwise; any real number between 0 and 1 may be used to describe graded structures, smooth boundaries and alloying effects) and Δ is the relative mismatch of the dot lattice with respect to the substrate lattice,

$$\Delta = \frac{a_{dot} - a_{host}}{a_{host}}, \tag{2.42}$$

a_{dot} is the dot lattice parameter and a_{host} is the host lattice parameter. At a free sample surface the boundary conditions

$$\sigma_{jk} n_k = 0 \tag{2.43}$$

have to be fulfilled, where $\vec{n}$ is the vector of the surface normal.

The displacement field is then expanded into the Fourier series in lateral directions. The Fourier coefficients depend on the vertical coordinate only, and can be calculated by solving ordinary differential equations. For a detailed description of this approach, see [81].

This method performed well for quantum wire systems, [81, 82]. Consequently, we assume that it can also be used for quantum dot systems; however, it should be applied with caution due to the approximations made there. Some basic properties of the method will be discussed later in Section 3.1.2.

2.3.3 Impact on the electronic structure

In the adiabatic approximation, the motion of the electrons is decoupled from the motion of atoms (more precisely, positive ions); the atomic positions enter the electronic Hamiltonian as parameters. The displacement of the atoms from their original position leads to the modification of the effective potential seen by electrons and therefore to the modification of their energies (i.e., the band energies). The constant displacement of all atoms in the sample is a mere translation of the sample, which of course cannot modify the energies; the gradient of the displacement is therefore required. The gradient can be decomposed into two parts: antisymmetric, which describes the rotation of the sample and also cannot influence the energies, and symmetric, which is actually the strain tensor. It is therefore possible to expand the energy differences induced by the displacement into a power series of a strain tensor components. The coefficient in such expansion are referred to as deformation potentials. The expansion is in most cases restricted to the linear terms; this is slightly surprising, because non-linear terms may play an important role in the highly strained quantum dots, but almost no effort has been dedicated to studying non-linear effects.

The presence of the inhomogeneous strain field violates translational symmetry. However, if the strain-induced energy shifts vary slowly in the space, it is very reasonable to assume that the band structure is preserved, only with spatially dependent energies. The energy modifications than play the role of the slowly varying potential, which can be treated by the envelope function method described above. Of course the strain field may couple and mix the bands, as in the case of any additional potential lacking translational symmetry.

The strain Hamiltonian for the zinc-blende semiconductors considering eight bands near the band gap was derived by Bir and Pikus [83, 84]. The underlying symmetry is the same as in the case of eight band $\vec{k} \cdot \vec{p}$ Hamiltonian H_{8kp} (2.10). The strain Hamiltonian H_{strain} can be obtained from the H_{8kp} by the following substitutions:

1. The energies E_g, Δ are substituted by 0, the value of the conduction-valence band coupling P (E_P) is preserved.

2. The Luttinger parameters γ_1, γ_2, γ_3 and the conduction band curvature parameter s are replaced by the deformation potentials in the following way: s is replaced by the conduction band hydrostatic deformation potential a_c, γ_1 by the valence band hydrostatic deformation potential a_v, $-2\gamma_2$ by the biaxial deformation potential b, and $-2\sqrt{3}\gamma_3$ by the shear deformation potential d.

3. Terms quadratic in $\vec{k}$ are substituted by the pattern

$$\frac{\hbar^2}{2m_0} k_i k_j \rightarrow \varepsilon_{ij};\ i,\ j \in \{x, y, x\}. \tag{2.44}$$

4. Terms linear in $\vec{k}$ are substituted by the pattern

$$k_i \rightarrow -\sum_{j\in\{x,y,x\}} \varepsilon_{ij} k_j;\ i \in \{x, y, x\}; \tag{2.45}$$

the components of $\vec{k}$ are subsequently substituted by $\vec{k} \rightarrow -i\nabla$.

The strain field apparently results in the band coupling and mixing. An evaluation of the Hamiltonian H_{strain} at particular points of space and a pointwise diagonalization of 8×8 matrices provide a very useful insight into the "band edges", which actually form the confinement potential for the motion of the particles. If we want to employ only single band envelope function method in the following calculations of the single particle states, we simply neglect the off-diagonal elements. The expressions for the energy shifts ΔE of the band energies at the Γ-point in the presence of strain are given below. The shifts are denoted by subscripts EL, HH, LH, and SO, referring to the conduction band (electrons), heavy-hole band, light-hole band, and spin-orbit split-off band, respectively.

$$\Delta E_{EL} = a_c H,\ \Delta E_{HH} = -a_v H - bB,\ \Delta E_{LH} = -a_v H + bB,\ \Delta E_{SO} = -a_v H, \tag{2.46}$$

where the hydrostatic part of the strain is defined as $H = \varepsilon_{xx} + \varepsilon_{yy} + \varepsilon_{zz}$ and the biaxial part as $B = \varepsilon_{zz} - (\varepsilon_{xx} + \varepsilon_{yy})/2$. The shear component of the strain has no impact on the energy shifts within this single band description.

Finally, we briefly discuss a general impact of the strain field on the electronic structure of quantum dots. The lateral strain (ε_{xx}, ε_{yy}) inside the dots is, as a rule, compressive (accommodation to the substrate), which results in the tensile vertical strain. The hydrostatic part of the strain is negative, the biaxial part is predominantly positive (it may change the sign on the top of spiky structures such as tall pyramids). The bands are usually shifted in the following way: the electrons are shifted to higher energies (band gap is increased), the holes are not shifted pronouncedly due to the much smaller hydrostatic deformation potential (which is about one tenth of the conduction band value), but are splitted due to the biaxial strain shifting the heavy holes up and the light holes down. This reduces the band gap (though the increase due to the electrons is not fully compensated) and favors the heavy holes in the ground valence state (which is further supported by a larger confinement energy due to their higher effective mass).

2.4 Piezoelectric field

Piezoelectricity is the ability of some materials to generate an electric polarization in response to applied mechanical stress. The crystals are piezoelectrically active if they lack the inversion

symmetry and the bonds between the atoms are polar, which is the case of all III-V semiconductors. Considering linear piezoelectric effect, the relation between the polarization vector and strain tensor is described by the third order electromechanical tensor; for zinc-blende structure it has only one independent non-zero component e_{14}. The polarization is given as

$$\vec{P}_1 = 2e_{14} \begin{pmatrix} \varepsilon_{yz} \\ \varepsilon_{xz} \\ \varepsilon_{xy} \end{pmatrix}. \tag{2.47}$$

It was pointed out recently that the quadratic piezoelectric effect plays an important role in the electronic structure of the quantum dots due to the huge strain present in them [54]. The relation between the polarization vector and strain tensor in zinc-blende structure is described by three independent components of the fifth order electromechanical tensor B_{114}, B_{124}, B_{156} and reads

$$\begin{aligned} \vec{P}_2 = 2B_{114} & \begin{pmatrix} \varepsilon_{yz}\varepsilon_{xx} \\ \varepsilon_{xz}\varepsilon_{yy} \\ \varepsilon_{xy}\varepsilon_{zz} \end{pmatrix} + \\ + 2B_{124} & \begin{pmatrix} \varepsilon_{yz}(\varepsilon_{yy}+\varepsilon_{zz}) \\ \varepsilon_{xz}(\varepsilon_{xx}+\varepsilon_{zz}) \\ \varepsilon_{xy}(\varepsilon_{xx}+\varepsilon_{yy}) \end{pmatrix} + \\ + 4B_{156} & \begin{pmatrix} \varepsilon_{xy}\varepsilon_{xz} \\ \varepsilon_{xy}\varepsilon_{yz} \\ \varepsilon_{xz}\varepsilon_{yz} \end{pmatrix}. \end{aligned} \tag{2.48}$$

Piezoelectric charge ρ_{piezo} arises from the total polarization $\vec{P} = \vec{P}_1 + \vec{P}_2$:

$$\rho_{piezo} = -\nabla \vec{P}. \tag{2.49}$$

The piezoelectric potential V_{piezo} can be obtained in the following way: We expand the right hand side of the Gauss law $\rho_{piezo} = \nabla \vec{D}_{piezo}$ using the linear relation between the electric displacement and intensity $\vec{D} = \epsilon_0 \epsilon_r \vec{E}$ and the definition of potential $\vec{E}_{piezo} = \nabla V_{piezo}$. The resulting equation is

$$\rho_{piezo} = \epsilon_0 \nabla \left[\epsilon_r \nabla V_{piezo} \right] \tag{2.50}$$

(the static dielectric constant ϵ_r is material dependent and therefore does not commute with the differential operator ∇). From here we directly obtain the Laplace equation

$$\nabla^2 V_{piezo} = \frac{\rho_{piezo}}{\epsilon_0 \epsilon_r} - \frac{1}{\epsilon_r} \nabla V_{piezo} \cdot \nabla \epsilon_r, \tag{2.51}$$

where the first term on the right hand side refers to the real charge density while the second is the contribution of so-called image charge (polarization interface charge) caused by a discontinuity of ϵ_r on the heterostruture boundaries.

The shear strain is crucial for both components of the polarization. While the quadratic part plays important role only in the dot volume due to the product with the diagonal terms of the strain tensor, the linear part is distributed also to a large surrounding of the dot. The shape of the piezoelectric potential is structure dependent, but, in general, it has octopole-like structure. It has an important impact on the symmetry of the wave functions: The shapes of

the dots used in the modeling are often highly symmetric (C_{4v} for pyramids, boxes etc. or even $C_{\infty v}$ for lenses etc.). The symmetry of the underlying lattice is T_d (tetrahedral), but it is not treated properly by the continuum models – single band envelope function model is isotropic, multiband envelope function model leads to the anisotropic effective mass with O_h (cubic) symmetry, the elastic tensor has the same symmetry. On the other hand, piezoelectricity respects this lattice symmetry, reducing the symmetry of the highly symmetric dots to C_{2v}. As revealed by pseudopotential calculations, the piezoelectricity is not the only atomistic effect reducing the symmetry, but only this is usually incorporated in the continuum description.

In the case studied by Bester [55], which was a lens-shaped InAs/GaAs quantum dot, the second order piezoelectric potential has approximately the same magnitude as the linear one, but the sign was opposite. Both terms canceled each other, resulting in a piezoelectricity free quantum dot. Many other structures were studied in [85, 86], confirming qualitatively the opposite sign of both terms, but some non-zero residual piezoelectricity is usually present. The importance of the piezoelectricity is higher for the dots with large volume, high aspect ratio (height to the lateral dimension) and abrupt boundaries.

2.5 Magnetic field

Magnetic field is introduced into quantum mechanics by the Peierl's substitution

$$\vec{p} \to \vec{p} - q\vec{A}, \tag{2.52}$$

where p is the momentum operator, q is the charge of the particle, and A is a vector potential describing the magnetic field, defined as $\vec{B} = \operatorname{curl} \vec{A}$. The vector potential is not determined uniquely, the magnetic field is invariant under the transformation

$$\vec{A} \to \vec{A} + \operatorname{grad} \chi \tag{2.53}$$

for arbitrary scalar field χ, which follows directly from the identity

$$\operatorname{curl} \operatorname{grad} \chi(\vec{r}) = 0. \tag{2.54}$$

The transformation 2.53 is called gauge transformation. Two frequently used gauges for the homogeneous magnetic field with induction of magnitude B directed along the z-axis are: Landau gauge

$$\vec{A} = (0, Bx, 0), \tag{2.55}$$

and symmetric gauge

$$\vec{A} = (-By/2, Bx/2, 0). \tag{2.56}$$

Although the Hamiltonian itself is gauge invariant, as well as its eigenstates, the invariance may be broken by the approximative numeric methods employed to obtain the eigenstates. This issue has been studied for eight-band $\vec{k}\cdot\vec{p}$ envelope function Hamiltonian discretized using finite differences approach. The differences between the eigenenergies for different gauges were observed [87, 88, 89] and the gauge invariant discretization was developed [69], based on a lattice gauge theory [90]. It has been shown that the differences between the gauge invariant discretization and standard discretization are negligible if the origin of the coordinate system is placed at the center of the dot.

In principle, the eight-band $\vec{k} \cdot \vec{p}$ envelope function Hamiltonian in the presence of the magnetic field is derived following the procedure described in Sections 2.1 and 2.2 and using the Peierl's substitution 2.52 at the appropriate steps. Here we just summarize the result. The Hamiltonian 2.10 is extended to the non-zero magnetic field by Peierl's substitution in the differential operators, which in this case reads

$$-i\hbar\nabla \rightarrow i\hbar\nabla - q\vec{A}, \tag{2.57}$$

and by adding the Zeeman energy term [59, 61]. The Zeeman term arises from the fact that the bands exhibit non-zero magnetic momenta; it is linear in field, and the matrix elements can be found in the references listed above.

2.6 Few-particle states: Configuration interaction method

Until this point we have restricted ourselves to the single particle states. However, quantum dots normally contain more than a single electron or hole; at least one electron and hole are required for intra-band optical transitions and even more charge carriers may be present. Consequently the multiparticle excitations such as excitons, charged excitons (trions) and biexcitons play an important role in quantum dot properties and a good understanding of them is essential.

There is an important difference between the exciton in bulk, or partially confining heterostructures (quantum wells and wires), and quantum dot zero-dimensional exciton. In the former case, the exciton is formed by attractive Coulomb interaction; beside the excitons there are always free charge carriers present in the system and the overall properties depend on their mutual ratio. The exciton can dissociate into free electron-hole pair; it is stable at low temperatures only. Both particles forming the exciton are heavily correlated. On the other hand, the excitons (and excitonic complexes) in quantum dots are held together by the confining potential; the Coulomb interaction acts only as a perturbation. Consequently, no free charge carriers exist, excitons are very stable and cannot dissociate. This allows creating very intriguing excitonic complexes, even those which are antibinding and which cannot exist in structures of higher dimensionality.

Another important consequence is rather low correlation of electrons and holes forming exciton (or of particles forming the excitonic complex). In other words, the wave function of the exciton is very well approximated by an (antisymmetrized) product of single particle state (which is of course not possible for structures of higher dimensionality, where the Coulomb interaction is dominant). This is a key point for a successful application of Configuration interaction method (CI) for calculations of the multiparticle states.

Configuration interaction is a linear variational method for solving the few-particle Schrödinger equation. The wave function of a few-particle system (which is an excitonic complex in our case) is expanded into a series of so-called configuration wave functions (CWFs). A CWF is an antisymmetrized (since the fermions are indistinguishable) product of single particle wave functions. It is advantageous, though not necessary, to use the eigenstates of an empty quantum dot to construct CWFs. In such case, individual CWFs describe the few-particle states without interaction. Switching the interaction on leads subsequently to a mixture of different CWFs in a few-particle wave function.

Full configuration interaction includes all CWFs, which can be constructed from a given set of single-particle orbitals. This form of the CI is not appropriate for the description of

large excitonic complexes since the number of configurations increases exponentially with the number of particles forming the excitation. There exist a feasible restriction of CWFs for such case: The number of the excited single particle states involved in each CWF can be limited to one (single excitation CWF, single CI), two (single-double excitation CWF, single-double CI), or another reasonably small number.

It remains to discuss the form of the interaction between the particles. Since the Bohr radius of the exciton is usually much higher than the lattice parameter (Frenkel exciton), we use standard Coulomb interaction with dielectric constant of the dot material, $V = e_1 e_2 / 4\pi\epsilon_0\epsilon_r r_{12}$. A thorough discussion of the matrix elements of this interaction is given in [91].

Chapter 3

Implementation and basic properties of the models

The aim of this chapter is twofold. First, we describe here the specific implementation of the models used within this work. We explore their properties, such as numerical stability, convergence rate, calculation complexity, and, last but not least, precision of results. We also compare relative merits of the models and discuss their suitability for particular problems. Second, we review some basics properties of the dots themselves. In particular we aim at answering the question "What happens with transition energies (and some other properties), if we modify the size and shape of the dots?" The discussion of the interaction between dots in a stack is left to Chapter 4 and the effect of external magnetic field is treated in Chapter 6.

We employ a few models of different complexity ranging from very simple to rather complex. At first sight the more complex models may be considered as superior to the simpler ones, but the situation turns out to be not so easy. Simple models have the following advantages:

1. Probably the most important is that simple models often allow a direct physical interpretation of the results. As an example we can distinguish between the lateral and vertical confinement effects when employing the variable well thickness approximation (Section 3.2), which is not possible in the variational approach (Section 3.3). Of course this understanding is only approximative, since in fact both confinements are coupled, but it may still be useful.

2. Another advantage is a lower computational complexity. This allows us to investigate a larger number of systems, to vary more parameters at once, and to obtain dense dependencies.

3. The electronic structure of quantum dots is sensitive to their size and shape, as well as to the chemical composition. When the modeling is used to interpret experimental data, a good knowledge of all these structural parameters is essential. However, the determination of the structural parameters is very difficult and our knowledge of them is usually rather poor. Employing the complex models with high accuracy brings no advantage in such cases, since the limiting factor for the precision of modeling is the accuracy of the structural data.

The advantages of the complex models are clear: they provide better accuracy, and may involve new physical phenomena (band coupling, piezoelectricity); they can also be used for testing the correctness and accuracy of the simple models.

We start this chapter by discussing the strain calculations (one implementation of atomistic valence force field (VFF) and one of continuum elasticity (CE)) and their comparison (Section 3.1). After choosing the proper strain model we proceed with the calculations of the electronic structure. Very simple approximation scheme based on the separation of coordinates, named Variable Thickness Well Approximation (VTWA), is introduced in Section 3.2. Section 3.3 presents the standard variational solution of single band $\vec{k} \cdot \vec{p}$ problem. To check the validity of both models as well as for some targeted calculations we used the eight band $\vec{k} \cdot \vec{p}$ based code developed at Technische Universität Berlin; some basic properties of it are discussed in Section 3.4.

3.1 Strain field

3.1.1 Implementation of Valence force field model

The implementation is based on the theory outlined in Section 2.3.1. The strain energy is expressed in terms of stretching and bending of the bonds between adjacent atoms; in the Keating model [70] it has the form of Eq. 2.32. The equilibrium condition is equivalent to the minimization of the strain energy; for the system containing N atoms it is expressed by the set of $3N$ cubic equations (2.33). We use the iterative approach described in [72] to solve these equations (see also Sec. 2.3.1): Atoms are placed at the host lattice points first. At each iteration, we go through all atoms and shift each to its equilibrium position, leaving the remaining ones fixed. Thus, we have to solve only N systems of 3 cubic equations within each iteration. This is repeated, until requested accuracy is reached.

Solving a system of three cubic equations is still rather time consuming and inappropriate for large systems. Instead, additional simplification is introduced with non-linear terms in cubic equations substituted with constant values obtained at the previous step. Another option is to use the Kane potential [75], in which the non-linear terms are neglected. Both approaches are compared below.

material	InAs	GaAs
α[N.m^{-1}]	35.18	41.19
β[N.m^{-1}]	5.50	8.95
C_{11}[GPa]	83.3	118.8
C_{12}[GPa]	45.3	53.8
C_{14}[GPa]	39.6	59.4
a[nm]	0.60583	0.56532

Table 3.1: Material parameters used for strain calculations: the Keating potential parameters α, β are taken from Martin [71], the elastic compliances C_{11}, C_{12}, C_{44} and the lattice parameters a from Landolt-Börnstein [92].

The parameters used in the calculations (two potential parameters and the lattice constant) are listed in Table 3.1. Geometric mean value of the parameter β have been used for the ternary configuration of atoms (i.e., Ga-As-In): $\beta_{\mathrm{Ga-As-In}} = \sqrt{\beta_{\mathrm{Ga-As}} \cdot \beta_{\mathrm{In-As}}}$.

To assess the accuracy of the solution, we introduce following parameters: the shift of an atom during one iteration (s_{acc}), the distance of an atom from its final position in the converged solution (Δ_{acc}), the difference of the distance between adjacent atoms between the actual and final position (d_{acc}). Since the accuracy of the solution is limited by the most diverted atom, we find the maximum values of all parameters over all atoms in the system. Only the first parameter is available during the iteration and may be therefore used to control program run; however, the accuracy of the solution is determined by the others (in particular, Δ_{acc} describes the accuracy of the displacement field, while d_{acc} determines the accuracy of the strain field). It is therefore desirable to explore the relations between all the parameters.

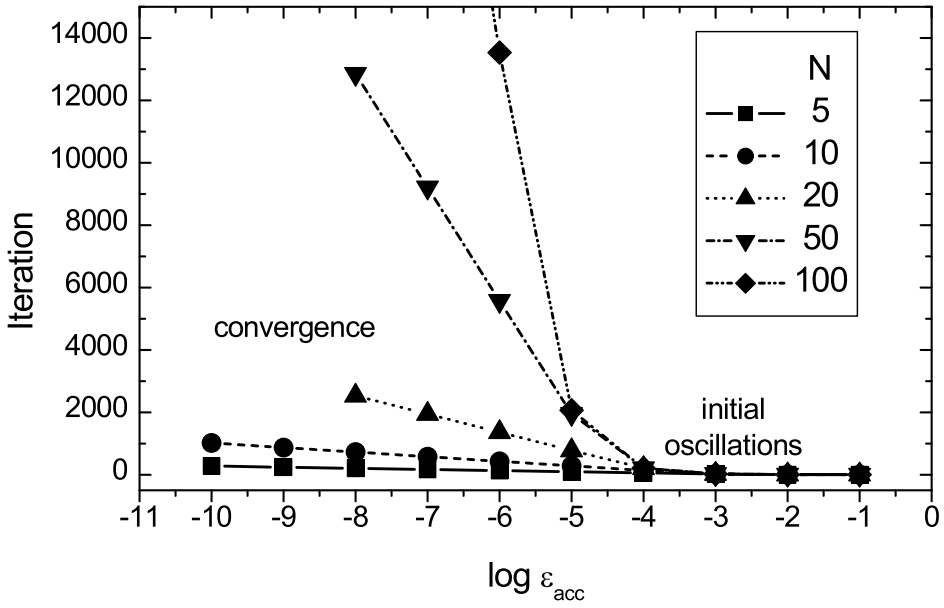

Figure 3.1: Number of iterations required to reach the accuracy ε_{acc} for a single InAs monolayer covered by GaAs. The total height of the system is N elementary cells. The zones of initial oscillations and convergence ranges are indicated.

The convergence properties of the method have been investigated in the system composed of a single InAs layer and a small number of GaAs layers. The periodic boundary conditions of the GaAs lattice were applied (although non-physical, they are convenient for such a study). The lateral size of the system is one elementary cell, the number of elementary cells in the vertical direction is denoted by N. The system therefore contains $8N$ atoms. We introduce a dimensionless accuracy parameter ε_{acc} defined as the ratio of the maximal shift during one iteration, s_{acc}, and the distance between the nearest neighbors in the lattice, $\sqrt{3}a/4$, where a is the lattice parameter. Figure 3.1 shows the number of iterations I required to reach

the accuracy of ε_{acc} for various system sizes N. Analyzing the dependencies, we found the approximate relation

$$I \sim -N^2 \log \varepsilon_{acc}. \tag{3.1}$$

This relation can be generalized with some caution to more complex systems; then, our calculations suggest that the size of the system N has to be replaced by some characteristic linear dimension of the system. The total time complexity is determined by the product of the required number of iterations and the duration of one iteration, which is proportional to N.

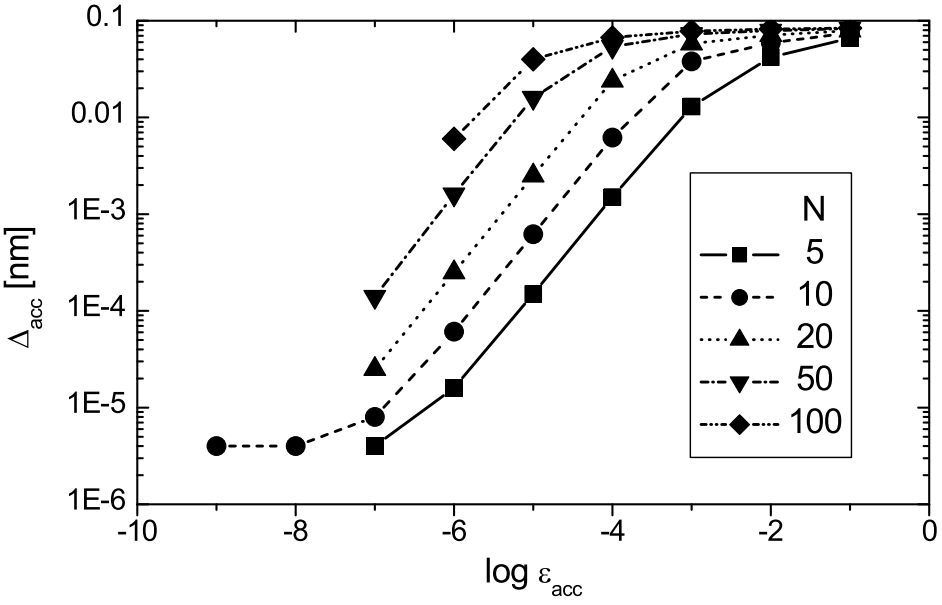

Figure 3.2: The dependence between the accuracy parameter ε_{acc} and the maximal displacement Δ_{acc} for a single InAs monolayer covered by GaAs. The total height of the system is N elementary cells.

Figure 3.2 displays the relation between the accuracy parameters Δ_{acc} and ε_{acc}. There is an initial oscillatory phase, in which the parameter ε_{acc} decreases rapidly without improving the accuracy Δ_{acc}. In the middle part, a decrease of ε_{acc} by one order of magnitude results in the same decrease of Δ_{acc}. In the final part, the accuracy limit has been reached. A very similar result is obtained for the parameter d_{acc}. The initial oscillatory part can also be seen in Fig. 3.1 as the rapid drop of ε_{acc}; this part is composed of a few iterations only. If we replot Fig. 3.1 (i.e., number of iterations required to reach a particular accuracy) versus Δ_{acc} rather than ε_{acc}, the oscillatory part is removed and the graphs are linear in the whole range. These results are displayed in Figure 3.3.

In the next part we discuss the boundary conditions. It is natural to use the periodic boundary conditions in the in-plane directions. It corresponds to the fact that the dots are not isolated, but surrounded by other dots. Although they are not ordered in a regular

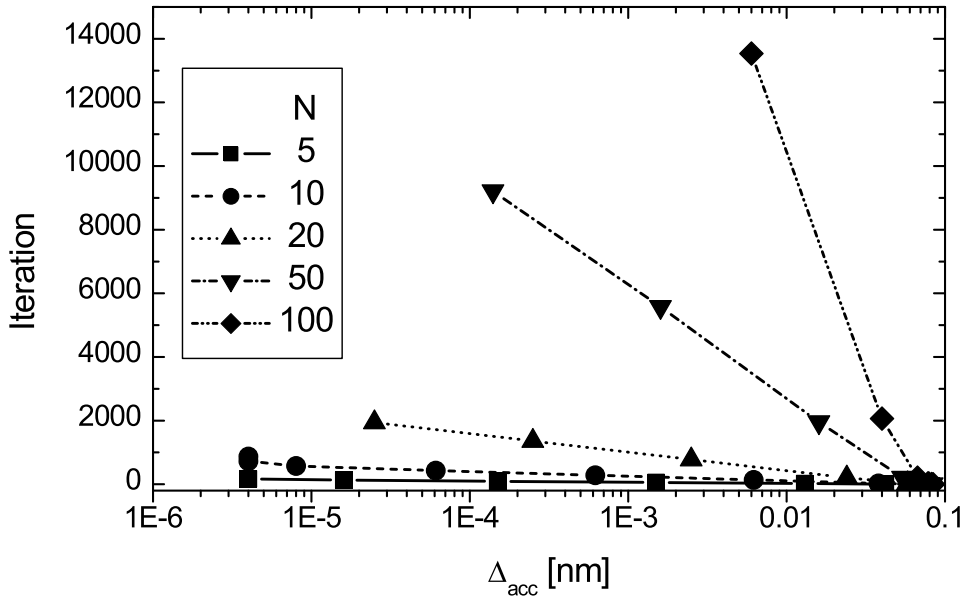

Figure 3.3: Number of iterations required to reach the maximal displacement Δ_{acc} for a single InAs monolayer covered by GaAs. The total height of the system is N elementary cells.

matrix, the periodic boundary conditions can still describe their mean elastic interaction. The appropriate size of the box should be close to the mean interdot distance. Furthermore the substrate imposes its lattice constant to the dots, which therefore limits their lateral stretching. Therefore the lateral periodic boundary conditions may be appropriate even for the box size considerably smaller than the mean interdot distance.

For the vertical direction, it is reasonable to assume that the strain does not penetrate too deep into the substrate; the boundary conditions assuming atoms fixed at the lattice nodes are appropriate. As the atoms at the surface are free to move, zero force boundary conditions may be applied. However, such an approach results into a very poor stability of the calculations. As an example we show in Figure 3.4 the strain energy versus the number of iterations for the system containing four InAs monolayers covered with six GaAs monolayers. In the inset we can see the oscillatory character of the solution. Furthermore, the surface boundary condition is not physically reasonable, since the surface structure is different from the structure inside the crystal. If the atoms followed the ordering of the crystal at the surface, two bonds per atom would be unsaturated. The atoms are therefore reordered in order to saturate all the bonds – this phenomenon is referred to as the surface reconstruction. We suggest here a different approach to treat the free surface: we apply the periodic boundary condition with the period extended by some offset with respect to the GaAs lattice. The offset corresponds to the vertical extension of the InAs material due to its lateral compression. The value of the offset is to minimize the strain energy; the proper value has to be found numerically. As an example, we present in Figure 3.5 the dependence of the strain energy versus the offset for a sample consisting of a single monolayer of InAs embedded in GaAs matrix. The total vertical

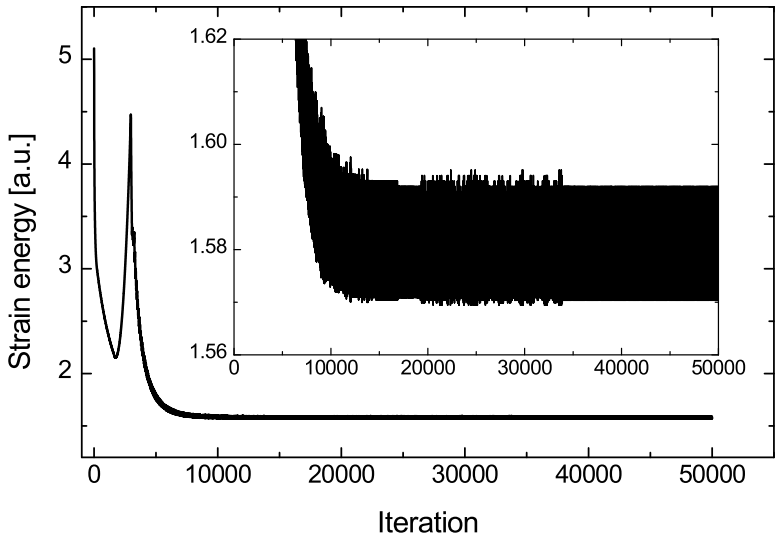

Figure 3.4: The strain energy of the actual configuration plotted vs. the number of iterations in the system of 4 ML of InAs capped by 6 ML of GaAs. Free surface boundary condition has been used in the vertical direction.

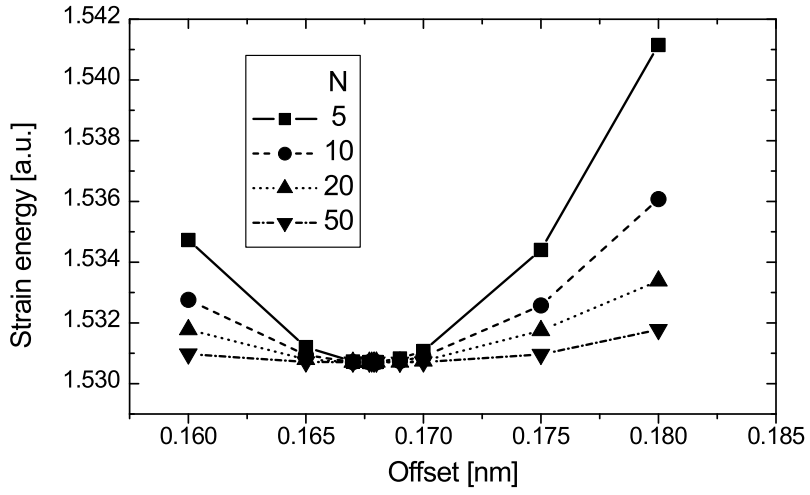

Figure 3.5: The strain energy of a single InAs monolayer covered by GaAs for various values of the offset. The periodic boundary condition has been used in the vertical direction, the offset is added to the GaAs lattice size in order to emulate the free surface. The total height of the system is N elementary cells.

size of the sample in elementary cells is denoted by N. We have found that the optimal offset value is independent of N. This is natural, since all the systems contain the same amount of InAs, which is responsible for the increase of the volume. Another significant feature is approximately parabolic dependence of the energy in the vicinity of the minimum, with a steep slope for small N and a smaller slope for large N; the large systems naturally allow a better relaxation of the strain if the offset is not chosen properly.

In the last part of this section we examine the strain field calculated using the implementation of the valence force field model. The results were published in part in [78].

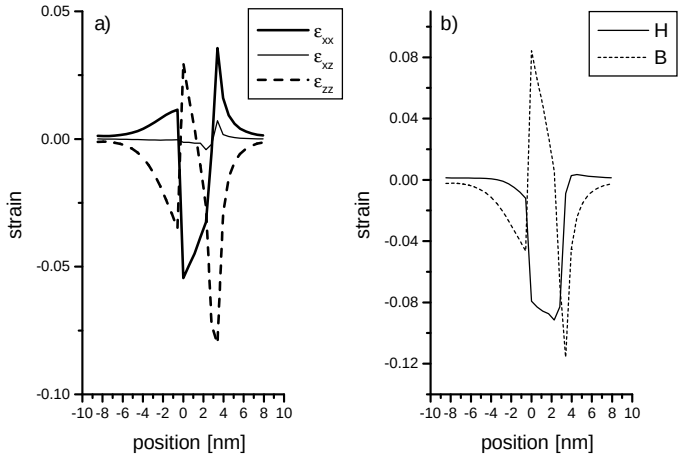

Figure 3.6: The strain distribution computed using the VFF model in and around an InAs pyramid within a GaAs matrix, along the axis of the pyramid: (a) strain components ε_{xx}, ε_{xz}, ε_{zz}, (b) hydrostatic (H) and biaxial (B) components of the strain, $H = \varepsilon_{xx} + \varepsilon_{yy} + \varepsilon_{zz}$, $B = \varepsilon_{zz} - (\varepsilon_{xx} + \varepsilon_{yy})/2$.

Figure 3.6 shows the strain tensor components ε_{xx}, ε_{xz}, ε_{zz} and the hydrostatic and biaxial components of the strain in a pyramidal quantum dot along its axis, calculated according to the VFF model. The dot lattice is matched to the substrate lattice, the component ε_{xx} related to the GaAs lattice is continuous at the dot-substrate boundary. Inside the dot, near its base, a region of normal strain exists, where the dot material is laterally compressed due to the thick substrate below the dot, and therefore vertically stretched in order to decrease the strain energy. Near the apex, however, a region of inverse strain exists, with a tensile lateral strain and a compressive vertical strain. The reason for this inverse strain is the match of the dot to the capping rather than to the substrate. This gives rise to the compressive vertical strain, while the tensile lateral strain arises from the compressive vertical strain decreasing the strain energy.

The ε_{xz} profile of Fig. 3.6 illustrates the correct atomic symmetry of the VFF model. According to the CE model, the strain tensor has C_{4v} symmetry in the (001) plane, for which the ε_{xz} component vanishes along the axis of the dot. The tetrahedral configuration of the nearest neighbors in the VFF model leads to the C_{2v} symmetry, for which no such condition

holds. Another example, often used for demonstrating the lowered symmetry of the VFF model, is the difference of the strain profiles along the [110] and [1$\bar{1}$0] directions, see [73].

The hydrostatic part of the strain tensor, representing the energy of dilatation, is almost constant inside the dot and does not extend to the substrate and capping. On the other hand, the biaxial part of the strain tensor, representing the energy of distortion, varies in space and extends to the outward material.

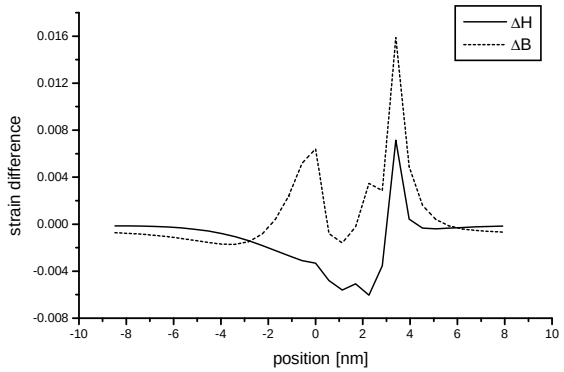

Figure 3.7: Differences of the hydrostatic (ΔH) and biaxial (ΔB) part of the strain, calculated using the linearized Keating model and the Keating model, respectively.

Figure 3.7 shows the difference between the strain profiles calculated using the linearized Keating (Kane) model and the Keating model. Both models give almost the same results, differing only near the apex of the pyramid. The apex consists of only a few atoms of the dot material and therefore is very sensitive to the choice of the model. Inside the dot, in the surrounding material, and even at the substrate-dot boundary, the results of both models agree perfectly. Thus, our results are comparable also with results obtained using the linearized Keating model.

Figure 3.8 shows the strain tensor components, ε_{xx}, ε_{xz}, ε_{zz}, and the hydrostatic and biaxial part of the strain in a lens-shaped quantum dot calculated using the VFF model. Similarly to the case of the pyramid, the dot is laterally matched to the substrate, the tensile strain in one direction is compensated by the compressive strain in the other direction, the non-zero ε_{xz} component reveals the lowered symmetry of the VFF model. The hydrostatic part of the strain is localized inside the dot and is almost constant in its volume. On the contrary, there is no region of the inverse strain and the biaxial component of the strain is almost constant inside the dot. The absence of the region of the inverse strain can be explained by recalling the fact, that there is no area at the dot boundary, for which the vertical coupling with the capping material is more important than the lateral coupling with the substrate. The constant biaxial part of the strain originates in the slab-like geometry, with the profile of the dot varying slowly along the vertical position. The strain profile in the lens-shaped quantum dot is quite similar to the strain profile in the slab.

Due to the high mismatch-induced strain occurring in dots, the possibility of alloying of the dot and host materials on the boundaries has to be taken into account. Clearly, a presence

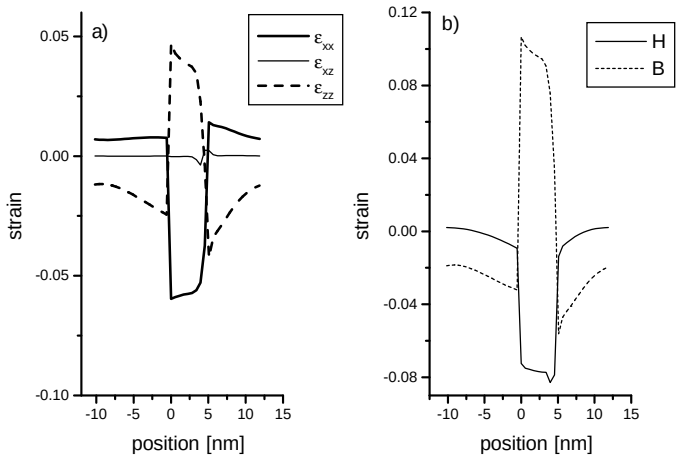

Figure 3.8: The strain distribution computed using the VFF model in and around an InAs lens within a GaAs matrix, along the axis of the lens: (a) strain components ε_{xx}, ε_{xz}, ε_{zz}, (b) hydrostatic (H) and biaxial (B) components of the strain, $H = \varepsilon_{xx} + \varepsilon_{yy} + \varepsilon_{zz}$, $B = \varepsilon_{zz} - (\varepsilon_{xx} + \varepsilon_{yy})/2$.

and the amount of alloying depend on the growth method and conditions, particularly on the growth temperature. The alloying leads to a further strain relaxation. We have studied laterally alloyed quantum dots of both pyramidal and lens shapes. In our model systems, the InAs content has been chosen to decrease linearly with the lateral distance from the dot boundary, replacing the step-like change. The relative InAs content was set up to one half at the dot boundary in order to preserve approximately the total amount of InAs in the alloyed dot. We have simulated the atomistic alloying pseudocontinually by means of effective $\mathrm{In}_x\mathrm{Ga}_{1-x}$ atoms, with their properties interpolated linearly between the properties of In and Ga atoms.

Figure 3.9 shows the difference of the hydrostatic and biaxial components of the strain between alloyed and unalloyed dots of both pyramidal and lens shapes, calculated using the VFF model. An observable difference occurs only at the top of the dots, where the alloying takes place. The effect is more significant for the pyramidal dot, where the sharp apex is more affected by alloying than the smooth top of the lens-shaped dot. The alloying affects the strain profile significantly, but only locally, close to the area of the ternary region.

3.1.2 Implementation of Continuum elasticity model

The algorithm used for calculations is described in detail in Refs. [81, 82]. Our implementation is only a minor extension of the code provided by V. Holý; a few novel shapes were added, and one improvement of the model was suggested. We therefore do not discuss the computational properties of the implementation; we only compare in Subsection 3.1.3 the results obtained from the model with those obtained from VFF model. Here we review the properties of the calculated strain field and the effect of the dot shape.

Figure 3.10 displays the strain tensor components in the lens-shaped quantum dot with the basis radius of 20 nm and the height of 5 nm in the xz-plane sections along the dot axis.

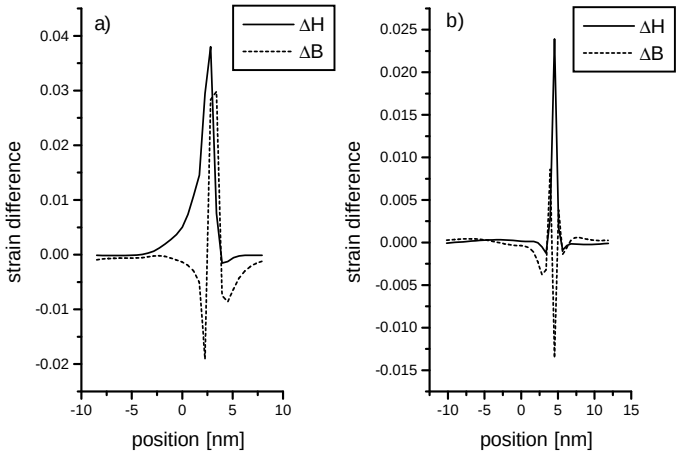

Figure 3.9: Differences of the strain distribution between an alloyed and unalloyed dot, computed using the Keating model, along the axis of the dot: (a) hydrostatic (ΔH) and biaxial (ΔB) components of the strain in the pyramidal dot (b) hydrostatic (ΔH) and biaxial (ΔB) components of the strain in the lens-shaped dot.

The coordinate system is parallel with the main crystallographic directions, with x, y, and z parallel to [100], [010], and [001], respectively. This notation will be used throughout this thesis. Both of the lateral diagonal components, ε_{xx} and ε_{yy}, exhibit a good accommodation to the substrate. The dot material is still slightly (up to 0.01) extended with respect to the GaAs lattice. This leads to the compressive "wings" in the ε_{xx} map, which touch the dot at its maximal lateral diameter. The lateral size of the wings is comparable to the dot radius. Of course, there are no wings visible in the ε_{yy} map, since it describes the strain perpendicular to the plane of the cut. The accommodation to the substrate is also clearly seen in the profiles of ε_{0xx}, which is the xx-component related to the GaAs lattice. Another interesting property of the lateral components (both ε_{xx} and ε_{yy}) is the existence of the area of tensile strain in the substrate below and above the dot, which extends vertically to the whole sample (referred to as a "cloud" hereafter). Its origin will be explained later.

The vertical diagonal component ε_{zz} is tensile in the whole volume of the dot, which is caused by the lateral compression. In consequence, the area below and above the dot exhibits compressive strain (in fact, this is the reason for the tensile lateral strain mentioned in the last paragraph) in order to compensate the dot extension. The area acts therefore in the same manner as the "wings" for lateral strain, but it is much more extended. The vertical diagonal component with respect to the GaAs substrate, ε_{0zz}, is also displayed in Fig. 3.10. Particularly notable is the homogeneity of all the diagonal components (vertical as well as lateral) inside the dot volume.

The shear strain is represented by ε_{xz}, the only non-zero component in the xz-plane. Its quadrupole shape implicates the octopole character of the piezoelectric potential. The symmetry requires that the non-diagonal elements are symmetric in the coordinate not included in the subscript. However, this is true only for the continuum elasticity and not in the case when the reduced atomistic symmetry is taken into account.

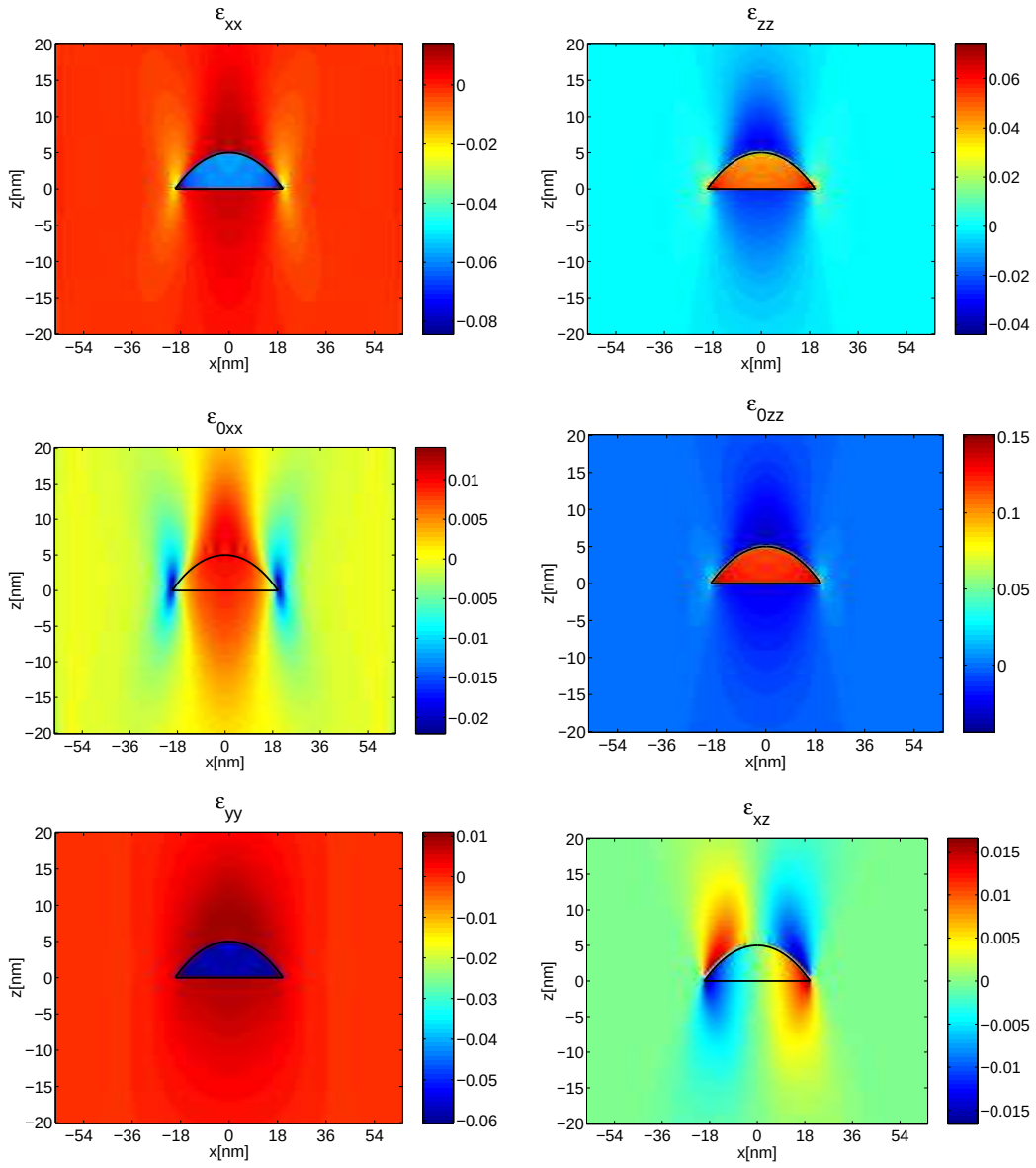

Figure 3.10: The strain field in the lens-shaped quantum dot with the basis radius of 20 nm and the height of 5 nm. The xz-plane cuts along the dot axis are displayed. The components denoted with the subscript 0 are related to the GaAs lattice instead to the intrinsic lattice.

Figure 3.11 shows the hydrostatic and biaxial components of the strain. The hydrostatic part, corresponding to the variations of the volume, is rather homogeneous in both dot and its surroundings. This is due to the compensating tendency in the inhomogeneous strain field: the compressive lateral strain generates the tensile vertical strain and vice versa. The dot volume is compressed, no pronounced volume variation is found in the surroundings. The biaxial part is also fairly homogeneous in the dot volume, which is caused by the homogeneity of the diagonal components of the strain tensor inside the dot. The deviations from the

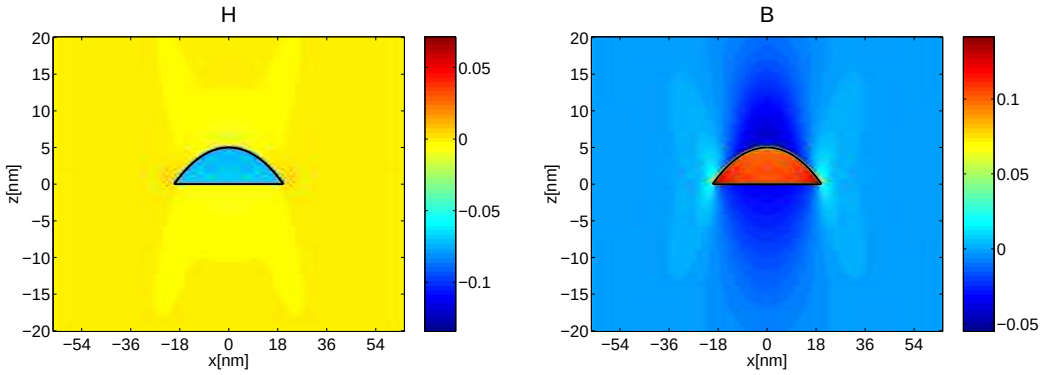

Figure 3.11: The hydrostatic and biaxial components of the strain field in the lens-shaped quantum dot with the basis radius of 20 nm and the height of 5 nm. The xz-plane sections along the dot axis are displayed.

homogeneity in the host material are significant, and follow the areas of the non-zero strain, i.e., lateral "wings" and vertical "clouds". Positive values occur inside the dot and the wings, slightly negative in the "clouds". Note that for rather tall dots, the biaxial component looses its homogeneity even in the dot volume and may even change the sign. We have already demonstrated this using the VFF model for the pyramidal dot (see Fig. 3.6), and will demonstrate it again using CE model (Fig. 3.13).

Restricting our model to the single band description, the strain influences the band energies according to Eqs. 2.46. The deformation potential used in these equations and energies involved in the band edges are listed in Table 3.2. Furthermore, following [93] we assume the offset energy of the conduction bands between both InAs and GaAs to have the value of 0.88 eV; consequently, the valence band offset is 0.22 eV.

material	InAs	GaAs
a_c[eV]	-6.66	-9.3
a_v[eV]	0.66	0.7
b[eV]	-1.8	-2.0
E_g[eV]	0.42	1.52
Δ[eV]	0.38	0.33

Table 3.2: Material parameters used in the calculations of band edges in the strained dots: the deformation potentials a_c, a_v, b, d, the band gap energy E_g, and the spin-orbit split-off energy Δ are taken from [94]. The energy values are for zero temperature.

The resulting band edges are displayed in Figure 3.12 for electrons, heavy holes, and light holes. The influence of the strain is most pronounced in the dot volume: both electrons and heavy holes are shifted in the same direction (upwards on the absolute scale). The band gap is therefore only slightly increased. The height of the potential well is decreased for electrons and increased for heavy holes. The light holes are shifted to the opposite side,

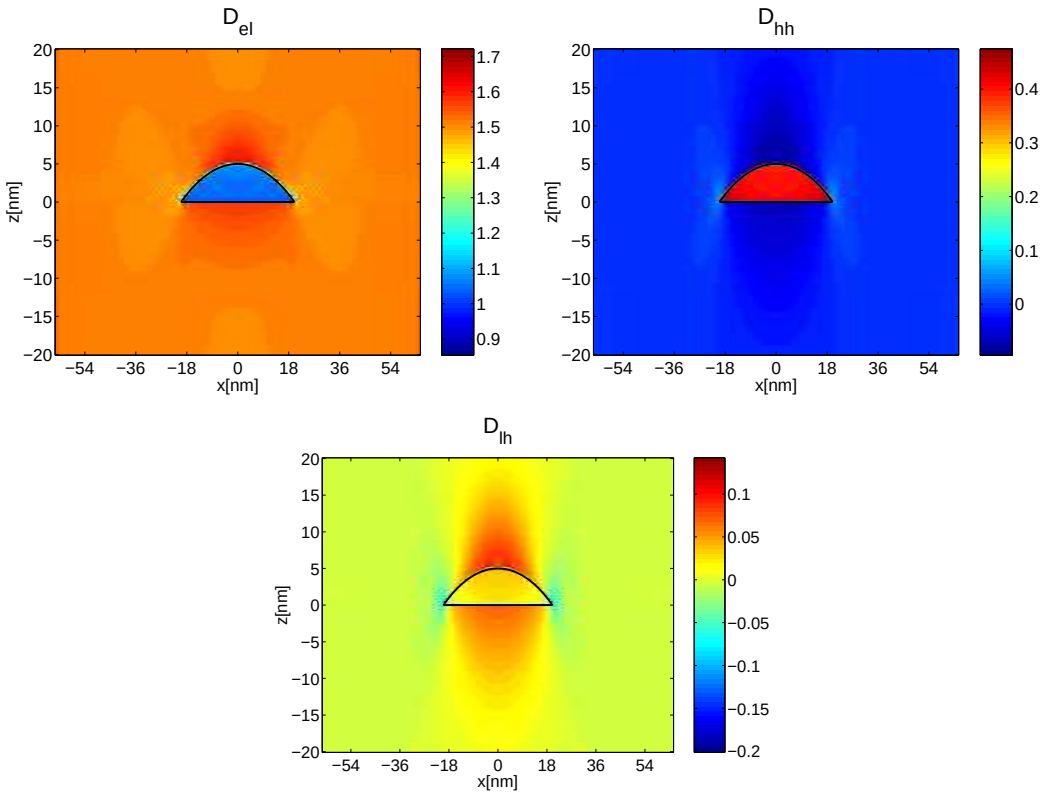

Figure 3.12: The band edges (including the effect of strain) in the lens shaped quantum dot with the basis radius of 20 nm and the height of 5 nm. The xz-plane cuts along the dot axis are displayed. The zero energy is set as a strain free top of the valence band in the host material (GaAs).

approximately to their energy level in the host material; the confinement is practically absent. This decreases the heavy and light hole band coupling and mixing within the multiband $\vec{k} \cdot \vec{p}$ description, and makes the single band approach more plausible. The energy shifts in the host material are less pronounced and not very important for the electronic levels; in general, the vertical confinement is slightly increased and lateral confinement slightly decreased for both electrons and heavy holes. The homogeneity of all the energies inside the dot is rather good. This is not the case of the host material due to the inhomogeneous wings and clouds; the inhomogeneity is more pronounced for the valence bands due to their sensitivity to the biaxial strain. These considerations lead us to the following conclusion: in order to simplify the model of the electronic structure, it is quite reasonable to neglect the inhomogeneities and to substitute the complex space-dependent potential by the simpler step-like potential, especially when some less elaborate method to retrieve the electronic structure is employed. We apply this simplification for all single band calculations in this work.

The dependence of the strain field on the shape of a quantum dot is examined in Figure 3.13. The strain field was calculated for several vertical profiles of the dot (cone, lens, cylinder) of the same height (5 nm) and radius (20 nm), and for lenses of various heights (2, 5, and 10 nm). Fig. 3.13 clearly shows that the homogeneity of the strain field inside the

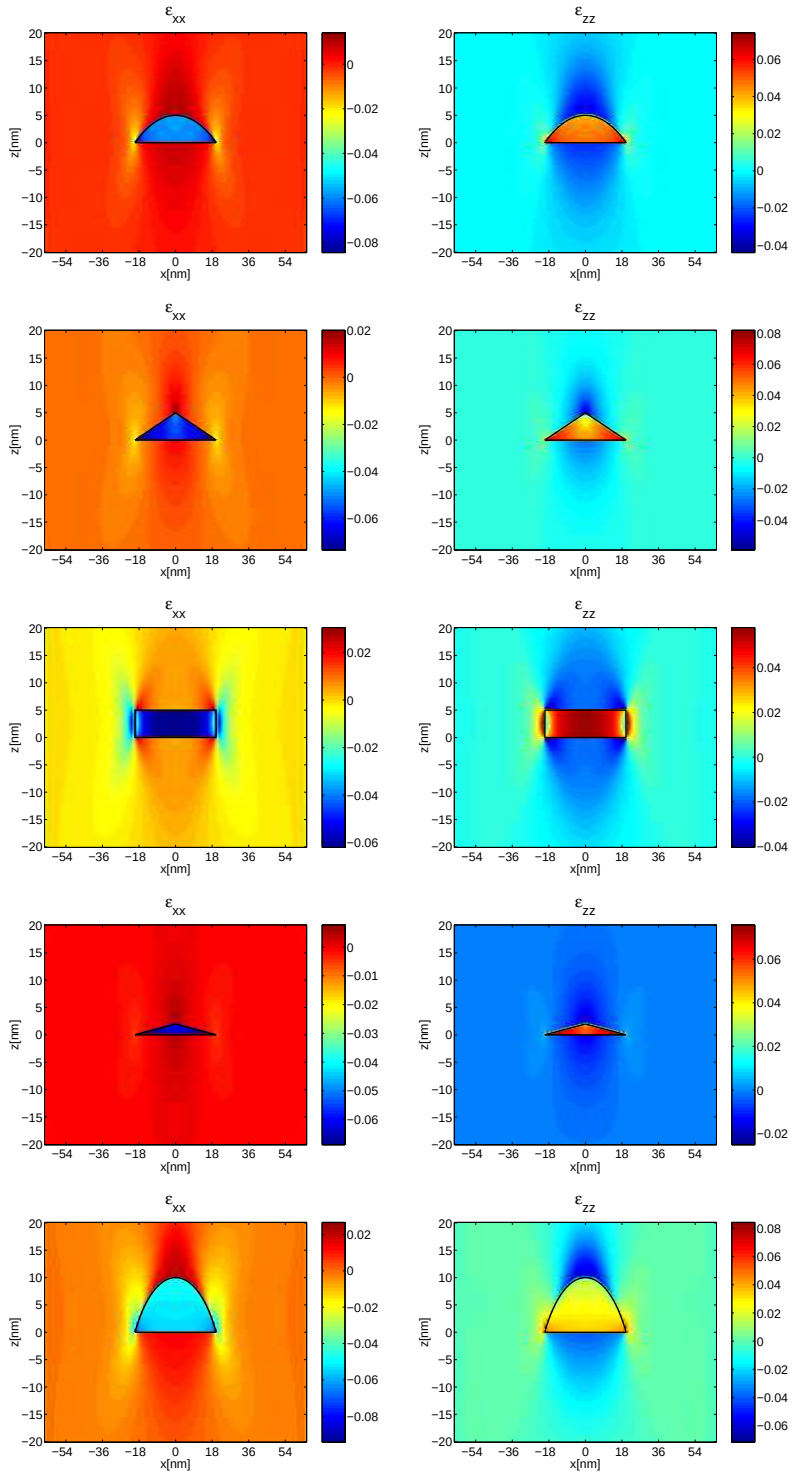

Figure 3.13: The lateral (ε_{xx}) and vertical (ε_{zz}) components of the strain field in the quantum dots of various shapes: lens, cone and cylinder with the basis radius of 20 nm and the height of 5 nm, and the lens with the basis radius of 20 nm and the of height 2 nm and 10 nm. The xz-plane sections along the dot axis are displayed.

dot is improved when decreasing its height and sharpness (i.e., moving from the cone to the cylinder) of the dot. The character of the wings and clouds is influenced as well. Since it is difficult to compare complex dependences on separate graphs, we concentrate on the linear scans shown below in separate graphs.

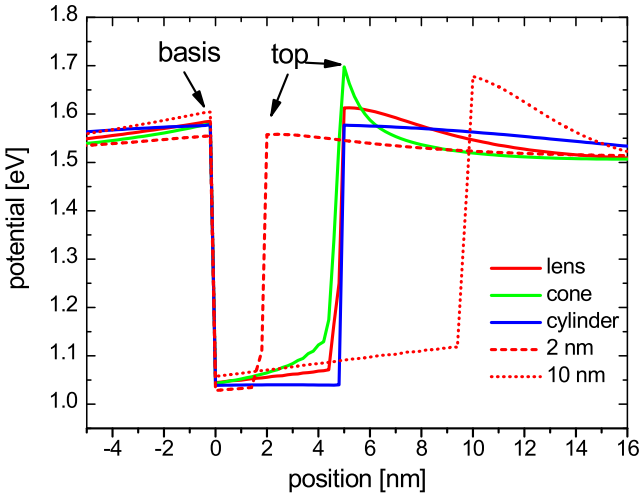

Figure 3.14: The conduction band edge (including the effect of strain) in various quantum dots, shown along the dot axis. Dots with various vertical profile and aspect ratio are compared: cone (green), lens (red), and cylinder (blue) with a height 5 nm and the lenses with the height of 2 nm (dashed line) and 10 nm (dotted line). The radius of all dots is 20 nm. The zero energy is set as the top of the valence band in the host material (GaAs) without any strain.

Figures 3.14 and 3.15 display the band edges along the dot axis for electrons and heavy holes, respectively. A notable feature is that the less is the dot profile varying along the axis, the more homogeneous is the strain field. We can assess the inhomogeneity by the magnitude (maximal difference from some mean value) and the rate (spatial gradient of the strain tensor). Nearby the sharp tip of the cone, we observe rapid and strong strain oscillations; on the other hand, in the cylinder, the strain exhibits only a step-like change on the boundaries, with an excellent homogeneity in both heterostructure constituents. Both magnitude and rate of the strain inhomogeneities are therefore increased in the structures with vertically varying profile. For the lenses of different height, the inhomogeneity rate is more or less identical in the dot volume. The magnitude becomes larger in tall dots due to their larger height. In the host material, both magnitude and rate increase with increasing height. We have to keep in mind that not the height itself, but rather the aspect ratio (the ratio of the height and lateral dimension) is responsible for the pronounced inhomogeneities.

The magnitude of the strain is also varied slightly with the shape. This can be explained qualitatively in the following way: in a quantum well, the material matches fully the substrate laterally, and extend vertically accordingly. In the dot, the compressive lateral strain is partly relaxed in comparison with the well, but the host material along the dot sides causes

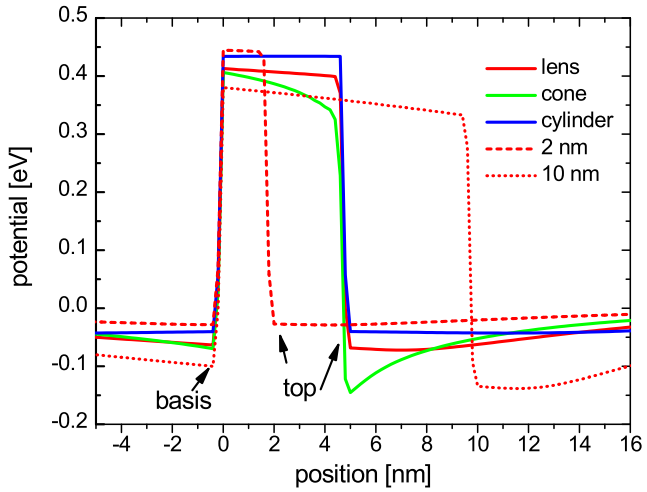

Figure 3.15: The heavy hole band edge (including the effect of strain) in various quantum dots, shown along the dot axis. Dots with various vertical profile and aspect ratio are compared: cone (green), lens (red), and cylinder (blue) with the height of 5 nm and the lenses with the height of 2 nm (dashed line) and 10 nm (dotted line). The radius of all dots is 20 nm. The zero energy is set as the top of the valence band in the host material (GaAs) without any strain.

a vertical compression. Consequently, the volume compression and the band gap increase when the shape changes from the slab-like to three-dimensional. This is clearly observed in Figure 3.16, where the mean values of the band edges for electrons are shown: the deepest potential well results for the thin lens-shaped dot, followed by the cylindrical, lens-shaped and conic dot of medium height, respectively. The bottom of the well for the tall lens-shaped dot is most highly, 55 meV above the bottom for the thin lens. The same tendency arises for the heavy holes, where the energy difference amounts to 85 meV. The host material below and above the dot is also more compressed, changing the shape from the slab-like to three-dimensional, which gives rise to a similar behavior, also observable in Figs. 3.14–3.16. The height of the potential wells is therefore more or less preserved for all shapes considered here.

The lateral variations are less pronounced than the vertical ones. We have studied the strain profile along the line going just above the dot basis, parallel with the [100] direction, intersecting the dot axis. The profiles of the electron band edge display no significant dependency on the dot shape, the profiles for the heavy holes are displayed in Figure 3.17. The results for the lens-shaped dots of several height values differ only by a constant energy offset. The lens and cone favor the outlying parts of the dots, while in the cylinder, the localization is stronger in the center.

3.1.3 Comparison of both models

Figure 3.18 shows the difference between the strain profiles calculated according to the Keating and CE models. It should be noted that we use an approximative approach to the solution of the CE model; this comparison should therefore be used as the test of the approximations

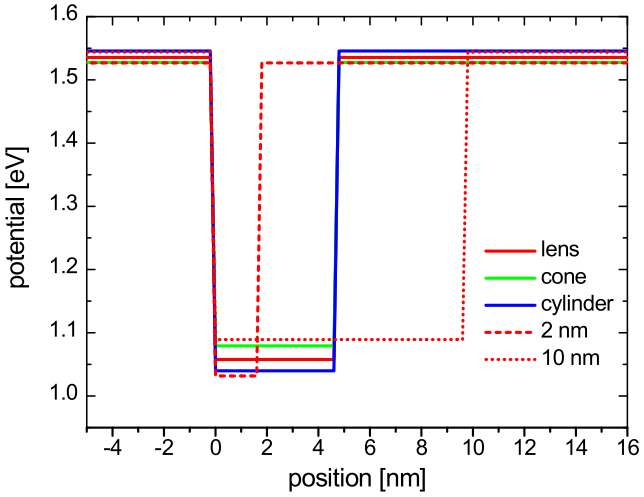

Figure 3.16: The homogenized conduction band edge (including the effect of strain) in various quantum dots, shown along the dot axis. The energy values were taken as averages of the values along the dot axis inside the dot and outside up to 5 nm from the boundaries. Dots with various vertical profiles and aspect ratios are compared: cone (green), lens (red), and cylinder (blue) with the height of 5 nm and the lenses with the height of 2 nm (dashed line) and 10 nm (dotted line). The radius of all dots is 20 nm. The zero energy is set as the top of the valence band in the host material (GaAs) without any strain.

made within the particular CE model, and not for testing the differences between the Keating and CE schemes. The only problematic approximation made in [81] is the following: the compliances of the inner and outward material are the same within this model; the authors recommend to use the outward material compliances in the equilibrium equation (2.38), and the inner material compliances in the equation for the volume force density (2.41). With this option, the differences between both models were rather high, making the approximative approach useless. Instead, we have decided to use the same parameters (those of the inner material) in both equations. The agreement of the approximative CE model with the exact solution within the Keating model inside the dot volume and the host material becomes reasonable, as shown in Figure 3.18. The difference is pronounced only close to the boundaries. Hence, this form of the CE model, requiring only a fraction of the computational time consumed by the Keating model, represents a method convenient for a fast estimation of the strain field in the quantum dot systems.

3.2 Variable thickness well approximation

This section is dedicated to the simplest of three methods for calculations of the electronic structure of quantum dots used through this work, so-called variable thickness well approximation (VTWA). We intend to use VTWA for a routine interpretation of experimental data, while the purpose of more elaborate methods will be twofold – first, to check the validity and accuracy of VTWA; second, to describe some peculiar features which do not result from the

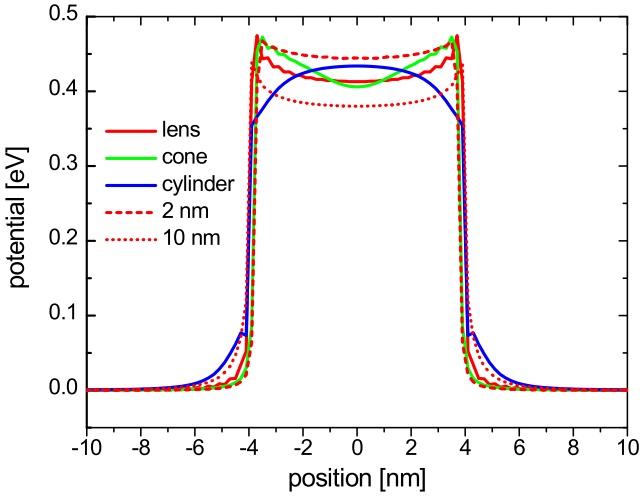

Figure 3.17: The heavy hole band edge (including the effect of strain) in various quantum dots, shown along the line going through the dot center (i.e., intersecting the dot axis) parallel with the basis slightly above it. Dots with various vertical profiles and aspect ratios are compared: cone (green), lens (red), and cylinder (blue) with the height of 5 nm and the lenses with the height of 2 nm (dashed line) and 10 nm (dotted line). The radius of all dots is 20 nm. The zero energy is set as the top of the valence band in the host material (GaAs) without any strain.

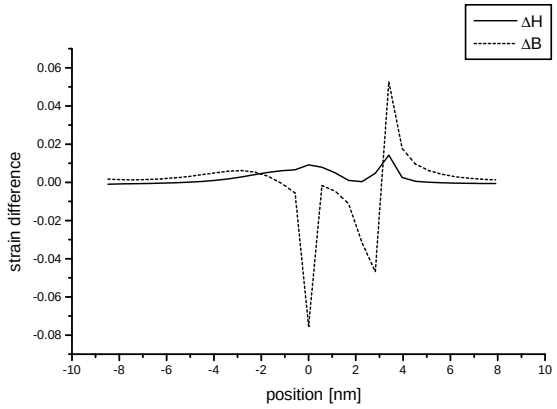

Figure 3.18: Differences of the hydrostatic (ΔH) and biaxial (ΔB) components of the strain, calculated using the CE and Keating models, respectively.

simplified description. The results presented in this and the following sections were published in [95], the method itself has been applied successfully in a number of studies [4, 20, 96, 97].

The proper method for obtaining the energy levels in quantum dots, suitable for interpreting systematically experimental data, should have the following properties: (i) It should be as fast as possible, while keeping a reasonable level of accuracy. (ii) The errors introduced by the selection of a particular physical model and by numerical approximations should not exceed

the errors of experimentally obtained dot sizes and shapes. The errors of the dot parameters originate not only from the limited accuracy of measurements, but also from the fact, that the experimental response is usually averaged over an ensemble with differing shapes and sizes. (iii) Since the dot parameters vary from one sample to another, the method has to be general enough to allow to treat all these different dots in the same manner.

We introduce here a simple, efficient technique for approximative solutions for flat dots of arbitrary shape (the only restriction is the flatness of the dots), based on the potential separation. The solution can be improved by adding perturbative corrections.

We start with a flat, quasi two-dimensional quantum dot. Such structure is similar to a quantum well, which provides the framework for search of the solution in the dot. The eight-band $\vec{k} \cdot \vec{p}$ Hamiltonian defined by (2.10) is diagonal in the basis listed in Table 2.1 for the quantum well in the center of its two-dimensional Brillouin zone. We expect that the band mixing is small for the flat dot; this assumption has been confirmed by the results of multiband calculations, particularly by the in-plane polarization of optical transitions, which exhibits the heavy hole character of the hole states [98]. Consequently, we will use the single-band theory.

Within the single-band effective mass approximation, the eigenstate of the particle in the heterostructure is assumed to have the form of the product of a periodic part of the appropriate Bloch function and the envelope function, which is denoted $\chi(\vec{r})$ in the following. The envelope function is determined by the quasi-Schrödinger equation (2.26), which we rewrite here in the form

$$\left[-\frac{\hbar^2}{2}\nabla\frac{1}{m(\vec{r})}\nabla + V(\vec{r})\right]\chi(\vec{r}) = E\chi(\vec{r}). \tag{3.2}$$

The confining potential $V(\vec{r})$ is assumed here to be determined solely by the band offsets between the adjacent materials, which are strongly affected by the presence of the strain field according to Eq. (2.46). Since the inhomogeneity of the strain field in the particular material is rather low, we will use the mean strain in our description in order to significantly simplify and speed-up the calculations. Hence, the assumed effective confining potential is rectangular. An example of the calculated vertical profiles of the confining potential is shown in Figure 3.19 for the 5 nm high InAs dot embedded in GaAs. The nontrivial influence of the strain is most pronounced in the potential profiles seen by the heavy- and light-holes, and in the non-negligible shift of the band energies in GaAs, extending rather deep into the substrate and capping materials.

The effective masses of the particles depend on the strain and energy of the state. We use Eq. (2.1) for them, the calculated dependencies are displayed in Figure 3.20. Since the effective masses are energy-dependent, the Schrödinger equation (3.2) and the mass equation (2.1) have to be solved iteratively. Details of the solution of the Schrödinger equation are given below.

For the quantum well, the potential is separable and the problem of electronic states is reduced to the solution of one-dimensional Schrödinger equation. A flat quantum dot can be described as a quantum well with laterally varying thickness. If the thickness variations are small compared to the vertical size of the dot, we may treat the thickness as a parameter, not influencing dynamical effects. In other words, the dot wave-function at the fixed lateral point $[x_0, y_0]$ has the same profile along the dynamic coordinate z as the wave-function of the quantum well of the given thickness. We can write

$$\chi_{DOT}(x = x_0, y = y_0, z) = f(\{x_0, y_0\})\chi_{WELL}(z, \{x_0, y_0\}), \tag{3.3}$$

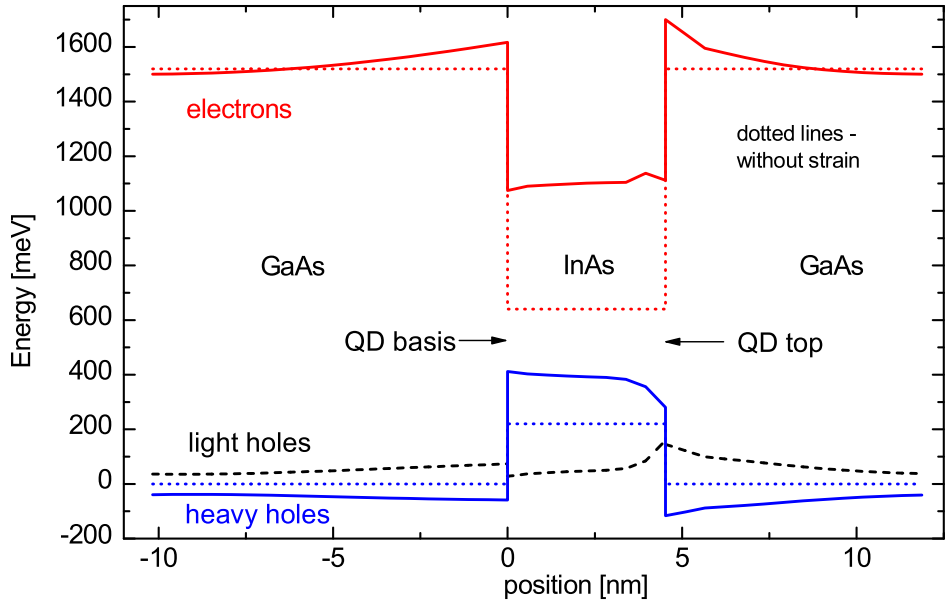

Figure 3.19: Band edges for electrons, heavy holes, and light holes in the lens-shaped dot of a height 5 nm and a radius 20 nm depicted along the dot axis. Dotted lines display the band edges in unstrained material, the energies depicted by solid lines include the effect of strain.

where

$$\left[-\frac{\hbar^2}{2}\nabla_z\frac{1}{m}\nabla_z + V(z,\{x_0,y_0\})\right]\chi_{WELL}(z,\{x,y\}) = \mathcal{E}(\{x_0,y_0\})\chi_{WELL}(z,\{x,y\}). \tag{3.4}$$

Inserting χ_{DOT} into (3.2), we obtain

$$\left[-\frac{\hbar^2}{2}\nabla_{xy}\frac{1}{m}\nabla_{xy} + \mathcal{E}(\{x,y\})\right] f(x,y)\chi_{WELL}(z,\{x,y\}) = Ef(x,y)\chi_{WELL}(z,\{x,y\}). \tag{3.5}$$

This system of equations is, in general, insolvable. However, we recall the flatness of the dot and neglect the derivatives of χ_{WELL}, obtaining

$$\left[-\frac{\hbar^2}{2}\nabla_{xy}\frac{1}{m}\nabla_{xy} + \mathcal{E}(\{x,y\})\right] f(x,y) = Ef(x,y). \tag{3.6}$$

The last equation has an obvious physical interpretation – the lateral motion of a particle is restricted by the potential formed by eigenenergies of the vertical problem. Solving both equations for the vertical and lateral motions, we obtain the electronic structure of the dot.

The contribution ΔE of the terms neglected in (3.5) has to be added to the total energy. Its magnitude with respect to the total energy is the measure of the accuracy of the approximation.

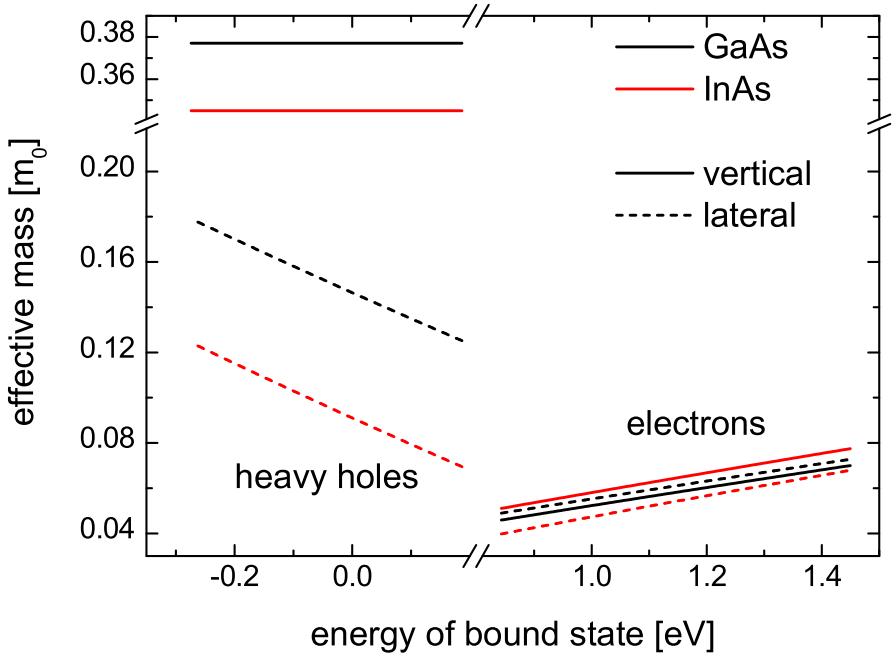

Figure 3.20: Energy dependent effective masses for electrons (positive energies) and heavy holes (negative energies) calculated according to Eqs. 2.1.

The lateral problem (3.6) still consists of the 2D Schrödinger equation. Taking into account the small effect of the lateral confinement, we can replace the inseparable potential $\mathcal{E}(x, y)$ by the separable potential

$$\mathcal{E}_{sep}(x, y) = \mathcal{E}(x, 0) + \mathcal{E}(0, y) - \mathcal{E}(0, 0). \tag{3.7}$$

The effect of the potential difference will be treated perturbatively and its magnitude with respect to the total energy is again a suitable measure of the accuracy of the approximation.

The material parameters involved in the calculations are: band gap energy E_g, spin-orbit split-off energy Δ, momentum matrix element E_P, hydrostatic deformation potentials a_c (conduction band) and a_v (valence bands), biaxial deformation potential b, elastic compliances C_{11}, C_{12}, C_{44}, lattice constant a, heavy hole mass along the growth direction $m_{hh}^{\perp}$, and valence band offset V_{vbo}. Their values are listed in Table 3.3. They are taken from [94], except for $m_{hh}^{\perp}$ and V_{vbo}, which are taken from [93]. Note minor differences of the values of elastic compliances from those listed in Table 3.1; they have no significant impact on the results, though. All calculations of the electronic structure presented in this work, performed using either VTWA or the variational method (Sec. 3.3), use these values of material parameters.

We now describe some important implementation steps and explore the properties of the approach described above. The procedure starts with the calculation of the strain distribution and the selection of proper homogeneous approximation, from which the confinement potentials for electrons and heavy holes arise. The vertical problem (3.4) is solved on a two-dimensional lateral grid of appropriate size and density of points. We have found that the

Parameter	InAs	GaAs
E_g	0.418 eV	1.519 eV
Δ	0.38 eV	0.33 eV
E_P	22.2 eV	25.7 eV
a_c	−6.66 eV	−9.3 eV
a_v	0.66 eV	0.7 eV
b	−1.8 eV	−2.0 eV
C_{11}	83.29 GPa	121.1 GPa
C_{12}	45.26 GPa	54.8 GPa
C_{44}	39.59 GPa	60.4 GPa
a	0.60583 nm	0.56532 nm
$m_{hh}^{\perp}$	$0.345\,m_0$	$0.377\,m_0$
V_{vbo}	0.22 eV	–

Table 3.3: Values of the material parameters used in VTWA calculations.

doubled lateral dimension of the dot, and two hundreds points in each direction, provide a good accuracy of the solution while keeping the calculation time reasonable. Solving the single lateral problem resembles the textbook example of a rectangular potential well except for the space dependent effective masses, we therefore do not describe it in detail here. Using the rectangular potential is, in fact, a significant simplification leading to much faster calculations. The differential Schrödinger equation can be reduced to an algebraic equation which, in turn, has to be solved numerically. For energies the following equation holds

$$\frac{\kappa}{k}\frac{m^*_{QD}}{m^*_{HOST}} = \begin{cases} \tan\frac{kL}{2} \\ -\cot\frac{kL}{2} \end{cases}, \tag{3.8}$$

where

$$k = \sqrt{\frac{2m^*_{QD}}{\hbar^2}E}, \quad \kappa = \sqrt{\frac{2m^*_{HOST}}{\hbar^2}(V-E)},$$

V is the height of the potential well, L is its thickness (equal to the dot height at the given point $[x_0, y_0]$), and m^*_{QD}, m^*_{HOST} are the effective masses in the dot and host material, respectively.

The left hand side of Eq. (3.8) is a real continuous decreasing function of E, positive-valued for the distinct energies of bound states, $E \in \langle 0, V\rangle$. The right hand side is composed of branches; it assumes always two values for each argument (except of multiples of $\pi/2$), one of them being negative. The positive branch runs through all real values when varying the argument of the goniometric function between two adjacent multiples of $\pi/2$. The function at the left hand side intersects each positive branch on the right hand side once. That means that there is always a single solution of Eq. (3.8) in each interval $((n-1)\pi/2, n\pi/2\rangle$ of the argument $kL/2$ (n is arbitrary non-negative integer here), provided the energy $E = \hbar^2k^2/(2m^*_{QD})$ corresponds to a bound state. The energies therefore lie in the intervals

$$E_n \in \frac{\hbar^2}{2m}\left(\frac{\pi}{a}\right)^2((n-1)^2, n^2\rangle, \tag{3.9}$$

and the total number of bound states (the maximum value of n) is

$$n_{max} = \left\lceil \frac{\sqrt{2m^*_{QD}}}{\hbar} \frac{L}{\pi} \sqrt{V} \right\rceil . \tag{3.10}$$

Since the intervals containing the roots of Eq. (3.8) are known, we apply the bisection to find the roots, particularly due to its robustness.

The vertical problems lead to a two-dimensional lateral potential, which is subsequently approximatively decomposed into two one-dimensional problems. The lateral problems are solved using the shooting method, following the approach described by Harrison [99]. In this approach, derivatives are substituted by the differences first, transforming the differential Schrödinger equation to a set of algebraic equations. We approximate subsequently the solution on the left hand side of a grid in the following way: The values of the wave function on two leftmost grid points are set to $f_0 = 0$ and $f_1 = 1$, respectively. Harrison [99] provides some arguments supporting this ansatz. Knowing the energy, we can calculate directly the wave function at all grid points. The energies of the bound states are then found as follows. We start with the zero value of energy (the bottom of the potential well). At each step, we calculate the wave function and increase the energy by some appropriate value ΔE, monitoring the values of the wave function at the rightmost point f_N of the grid. The boundary condition requires the vanishing value for sufficiently large grid. Since the wave functions are real, the change of the sign of the wave function at the rightmost point f_N after adding ΔE to the actual energy localizes the eigenenergy between the original and increased energy. A bisection is employed afterwards to find the solution. The step ΔE has to be smaller than the smallest distance between the eigenenergies to prevent multiple eigenenergies in the current interval. For realistic quantum dots, the value of 1 meV has been found suitable.

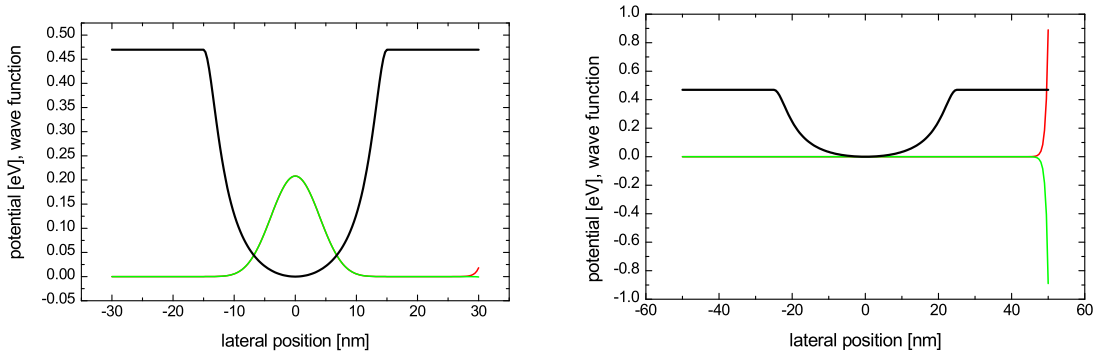

Figure 3.21: The black lines show the effective lateral confinement potentials for electrons in the lens-shaped of the height of 5 nm and the radius of 15 nm (left) and 25 nm (right). The red and green lines show the normalized wave functions for two energies localizing the eigenenergy at the end of the bisection procedure. The relative difference of both energies was 10^{-15}.

The rightmost value of the wave function is extremely sensitive to the energy, which is a serious drawback of the method. While this sensitivity favors the accurate determination of the energy, the determination of the wave function is badly hindered. This fact is illustrated in Figure 3.21, where the lateral wave functions are displayed for the lens-shaped quantum dots of the height of 5 nm and the radius of 15 nm and 25 nm, obtained for two energies localizing the eigenenergy at the end of the bisection procedure. The relative difference of both energies is 10^{-15}, about the maximum accuracy achievable by "double" data type. Despite this excellent accuracy of the energy, we observe differences between the corresponding wave functions of acceptable magnitude for the radius of 15 nm, but completely intolerable in the case of the radius of 25 nm. Note that these differences do not originate in numerical errors, they indeed occur due to the extreme sensitivity to energies. We have therefore employed user-defined data types with arbitrary precision in order to retrieve the wave functions with reasonable accuracy. In some cases we have used as many as three hundreds of significant figures to achieve this goal.

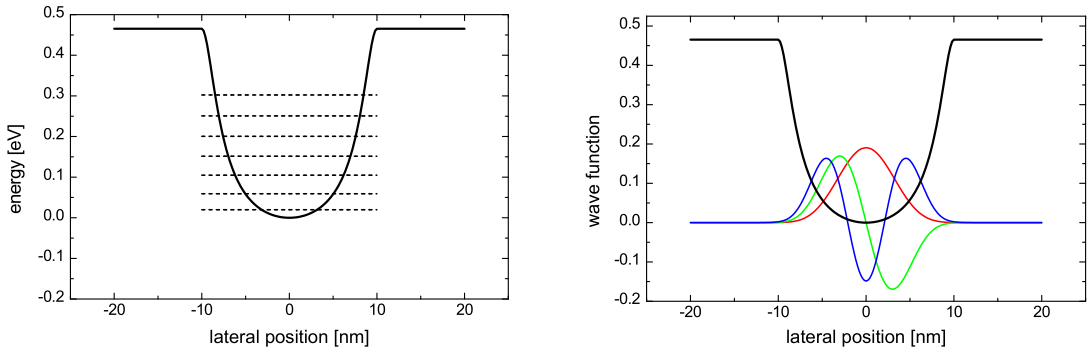

Figure 3.22: Effective lateral confinement for electrons the in lens-shaped quantum dot with the height of 5 nm and the radius of 10 nm (solid black line). The energies of bound states are displayed in the left part, and the corresponding densities in the right part of the figure.

An example of the effective lateral confinement potential $\mathcal{E}(x, 0)$ is displayed in Figure 3.22 for the lens-shaped quantum dot with the height of 5 nm and the radius of 10 nm. At first sight it seems to be close to a truncated parabolic potential, but a closer analysis reveals also pronounced biquadratic part (with a positive coefficient) in the area inside the dot. The energy levels of bound states are also shown in the left part of Fig. 3.22. The levels are almost equidistant; the energy separation between the levels increases slightly as the number of level increases, which is the consequence of the biquadratic component of the potential. The densities (square moduli of the wave functions) are shown in the right part of Fig. 3.22.

The steps described so far provided the wave functions. The values of energy can still be improved with two "perturbative" corrections (the quotation marks are used because the vertical correction does not result from the standard perturbation theory). Both consist in principle of the mean values of the Hamiltonian terms neglected in the preceding steps, particularly of the derivatives of χ_{WELL} in the system (3.5) ("vertical" or "kinetic" correction) and the term $\mathcal{E}(x, y) - \mathcal{E}_{sep}(x, y)$ resulting from the decomposition of lateral potential (3.7) ("lat-

eral" or "potential" corrections). The magnitude of the corrections determines the accuracy of the approximations used here.

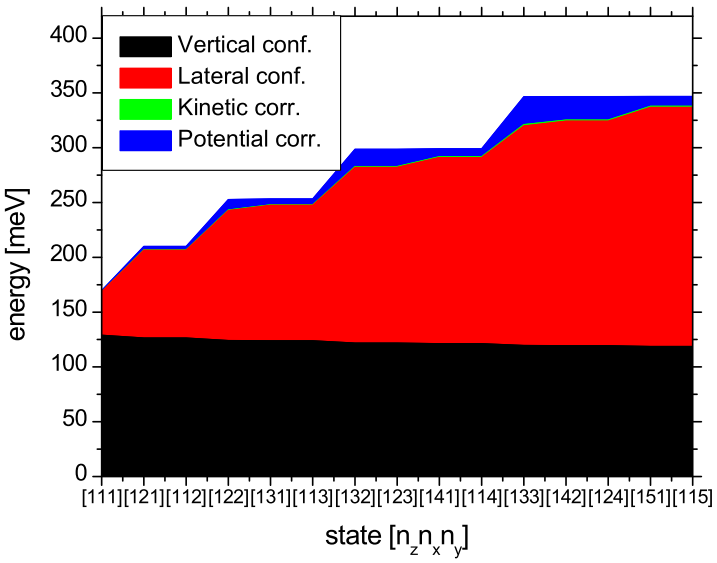

Figure 3.23: The lowest electron energy levels and their composition in the lens-shaped quantum dot with the height of 5 nm and the radius of 10 nm.

Figure 3.23 displays the energies of fifteen lowest-lying bound states of electrons in the lens-shaped quantum dot of the height of 5 nm and the radius of 10 nm. The decomposition of the three-dimensional confinement to the three one-dimensional contributions allows us to identify each state by three quantum numbers, n_z, n_x, n_y, corresponding to the order of eigenstate in the individual directions. The energies obtained by the method can naturally be decomposed into four constituents, namely, the energies of vertical and lateral confinement and vertical and lateral corrections. All fifteen lowest electron levels displayed in Fig. 3.23 are derived from the ground vertical state. The vertical energy slightly decreases when the total energy increases; this is caused by an increase of the effective mass (see Fig. 3.20). The kinetic correction is found to be negligible for all states (0.5 % of the total energy at most) which justifies the corresponding approximation, i.e., neglecting the lateral derivatives of χ_{WELL} in Eq. (3.5). The lateral confinement contributes significantly to the total energy; its proportion is 23 % even for the ground state, and it becomes the dominant part of the energy for laterally excited states. We have to keep in mind that there are two lateral dimensions; the confinement energy per dimension is therefore halved. Nevertheless, the resulting magnitude of the lateral confinement energy might be surprising. Considering a very simple model of quantum dot, namely, the infinite rectangular potential well with the dimensions of the dot, a contribution of the lateral confinement would be only 1/9 of the total energy for the ground state. However, the profile of the lateral potential differs significantly from the vertical one, and the comparison with infinite potential well might be misleading. Since the profile of

the lateral potential is narrower than that of vertical, In fact, the realistic proportion of the lateral energy is higher than in the case of infinite potential well, since the lateral potential is narrower than the vertical. The potential correction turns out to be below 1 % of the total energy for the ground state, and up to 8 % for other states displayed in Fig. 3.23, which is still reasonably small. A notable feature is that the states with identical lateral "excitations" $n_x + n_y$ are approximately degenerate as in the case of the harmonic potential. Even more interestingly this is due to the potential corrections, while the pure lateral energies differ remarkably.

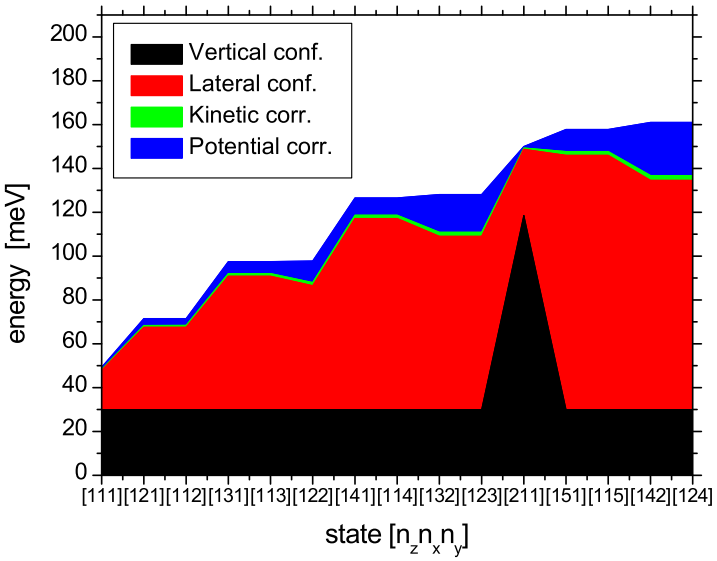

Figure 3.24: The lowest heavy hole energy levels and their composition in the lens-shaped quantum dot with the height of 5 nm and the radius of 10 nm.

The energies of heavy holes in the same quantum dot are displayed in Figure 3.24. Almost any conclusion concerning electrons holds for holes as well; here we describe the differences and some new features. The vertical energy of states with given n_z is identical for holes, provided the vertical effective mass is energy independent in our model (we recall that only distant bands, not involved in the eight band $\vec{k} \cdot \vec{p}$ treatment, influence the mass). The lateral confinement energy is more significant here than for electrons, amounting to 36 % of the total ground state energy. This is easily explained by the anisotropic effective mass of heavy holes, which is lower in lateral directions than in vertical direction (see Fig. 3.20). Both corrections, kinetic and potential, are remarkably higher in comparison with electrons, which is basically also due to the lower lateral mass of holes. Particularly, the kinetic correction is 0.8 % of the total energy for the ground state, and at most 1.5 % for fifteen lowest levels; the potential correction is 2 % of the total energy for the ground state and at most 15 % for fifteen lowest levels. The potential correction changes also the ordering of the laterally excited states: from those with identical $n_x + n_y$, the levels with lower $|n_x - n_y|$ have lower lateral energies for both

types of particles; they have also lower total (i.e., including potential correction) energies for electrons, but higher for holes. Although this fact is indeed interesting, we believe that it is of no practical importance and therefore we omit here the explanation. Another consequence of the pronounced lateral confinement is the presence of a vertically excited state ($n_z = 2$) among the fifteen lowest levels.

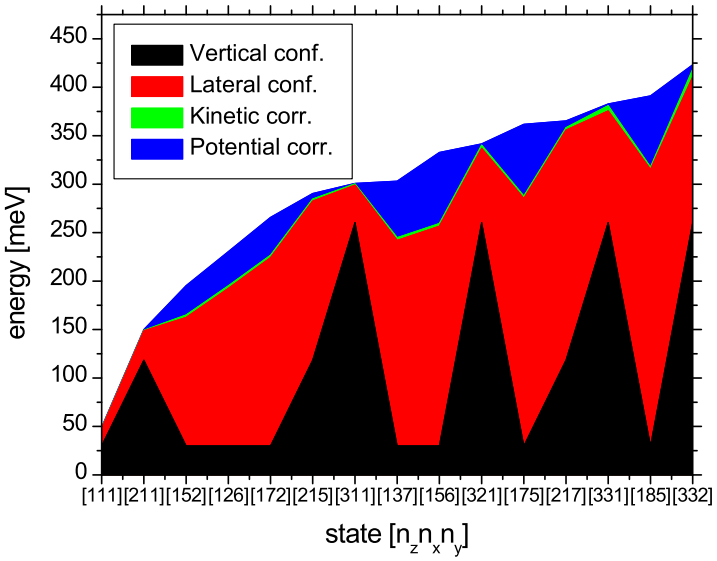

Figure 3.25: Heavy hole energy levels and their composition in the lens-shaped quantum dot with the height of 5 nm and the radius of 10 nm. Each tenth level is displayed.

Our method provided 33 electron bound states and 111 heavy hole bound states in the studied quantum dot. Naturally the prediction might be good only for a few low-lying states due to all the approximations involved in the model. Considering the upper states realistic would be misleading, but they may still provide an interesting insight into the method itself. We therefore discuss the energies of upper states here. Figure 3.25 displays the energies of heavy holes and their composition in the considered lens-shaped quantum dot. Each tenth bound state (i.e., 1^{st}, 11^{th}, etc.) is shown. The kinetic correction is very small for all states, which means that our assumption about the wave function shape defined by the factorization (3.3) is extremely reasonable.

The electronic structure as a whole can be represented conveniently in terms of the density of states (DOS), see Figure 3.26. Theoretically, the density is composed of δ-functions at each energy level, broadened to narrow Lorentzians when the finite lifetime of the carriers is taken into account. In Fig. 3.26 we have replaced each δ-peak with a Gaussian of 10 meV full width at half maximum (FWHM) for better legibility. This is suggested also by the fact that many experiments are carried out on dot ensembles rather than on a single dot; DOS δ-peaks broaden inhomogeneously due to the contributions of many dots in the ensemble, forming more or less Gaussian profiles. However, the width of different peaks is different in that case,

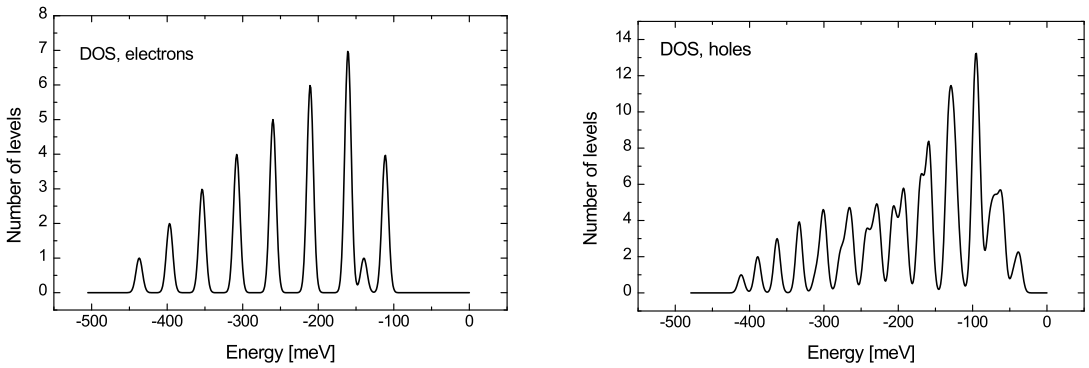

Figure 3.26: Density of states in the lens-shaped quantum dot with the height of 5 nm and the radius of 10 nm for electrons (left) and heavy holes (right), obtained from the VTWA model. The zero of energies is set to the top of the potential wells. Each δ-function has been replaced by the 10 meV FWHM Gaussian of unit amplitude for better legibility.

and it is also usually larger than 10 meV; the level of the broadening used in Fig. 3.26 serves therefore merely as an illustration. The electron DOS resembles roughly a two-dimensional harmonic oscillator due to the approximately parabolic lateral confinement. The heavy hole DOS is more complex due to the presence of vertically excited states.

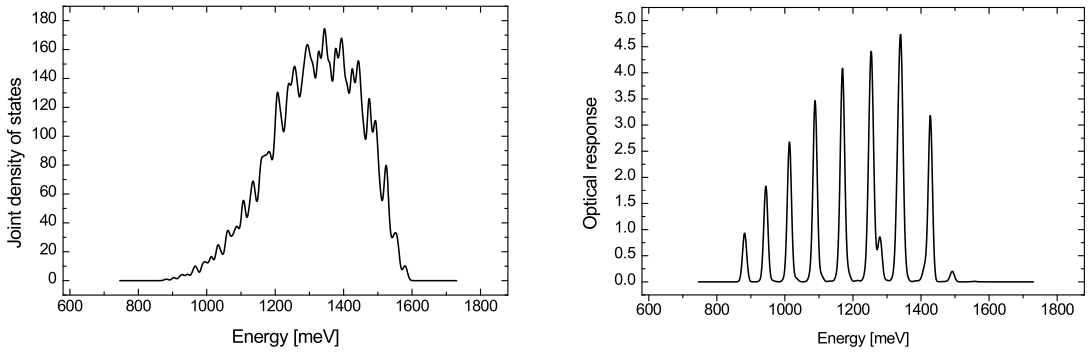

Figure 3.27: Joint density of states (left) and joint density of states multiplied by the transition probability (right) in the lens-shaped quantum dot with the height of 5 nm and the radius of 10 nm, obtained from the VTWA model. Each single-particle δ-function has been replaced by 10 meV FWHM Gaussian of unit amplitude for better legibility.

Figure 3.27 displays the joint density of states (JDOS) and the corresponding optical response (i.e., JDOS multiplied by the transition probability between initial and final states) in the considered system. The probability is proportional to an overlap between the envelope

functions of initial and final states; as we can see, the overlap is close to unity for the states with identical quantum numbers and very small otherwise.

In the following we explore in more detail the properties of wave functions. Figure 3.28 displays the densities (the squared modulus of wave function) of selected states in planar cuts parallel with the dot basis. We find that the wave functions approximately trace the shape of the dot, and the number of nodal planes in each direction corresponds to the quantum numbers. The heavy hole wave functions fill the dot volume more closely, while the electronic ones are more compact regardless of the dot shape. This is illustrated e.g. by the radius of the ground ([111]) state density in individuals planar intersections, which decreases as the dot radius decreases for holes, but remains almost constant for electrons. This effect is due to the effective mass, which is larger for holes than for electrons. The kinetic energy, which prefers a compact smooth shape, is therefore more important for electrons than for holes. Vice-versa, the potential energy, which prefers the wave function to fill the dot volume, is more important for heavy holes than for electrons. Note that the wave functions considered in this section are real and they can be obtained simply from the densities by extraction, whereas the sign has to be changed every time when the nodal plane is crossed.

So far we have discussed the electronic and optical properties of several quantum dots with well defined shape and dimensions. In practice, however, we often encounter the problem of unknown structural properties. The structural measurements can be inaccurate, even unreliable, or they can be missing. It is therefore important to have the dependences of quantum dot properties on their shape and dimensions at hand. This allows us to check the structural measurements, or to determine the structural parameters from the electronic and optical measurements It is also possible to determine the spread of sizes from the inhomogeneous broadening of the optical response etc. We have calculated transition energy of the lowest transition (denoted as "E_0") and its separation from the first higher transition (denoted as "ΔE") for the number of dot shapes (cone, lens, cylinder), and for a range of dot heights (h) and radii (r); the results are summarized in Figure 3.29. We observe the following facts:

1. The lowest transition energy decreases as the height and/or radius increases, i.e., as the dot volume increases.

2. For a certain height and radius, the lowest transition energy increases as the dot shape changes from cone to lens and to cylinder. The explanation of this trend lies basically in the increase of the dot volume V. To illustrate this, the values of E_0 and V are listed in Table 3.4 for several dot sizes. The energy E_0 tends to decrease as the dot volume

$h \times r$	2.8×20		4.0×20		2.8×30		4.0×30	
	E_0	V	E_0	V	E_0	V	E_0	V
cone	1077	1173	995	1676	1020	2639	933	3770
lens	980	1771	899	2547	938	3970	851	5688
cylinder	907	3519	824	5027	884	7917	795	11310

Table 3.4: The lowest transition energy E_0 (in meV) calculated using VTWA and the dot volume V (in nm^3) for several shapes and sizes (the height h and the radius r, both in nm). The energy shifts to lower values when changing the shape from cone to lens and cylinder due to the increase of the volume.

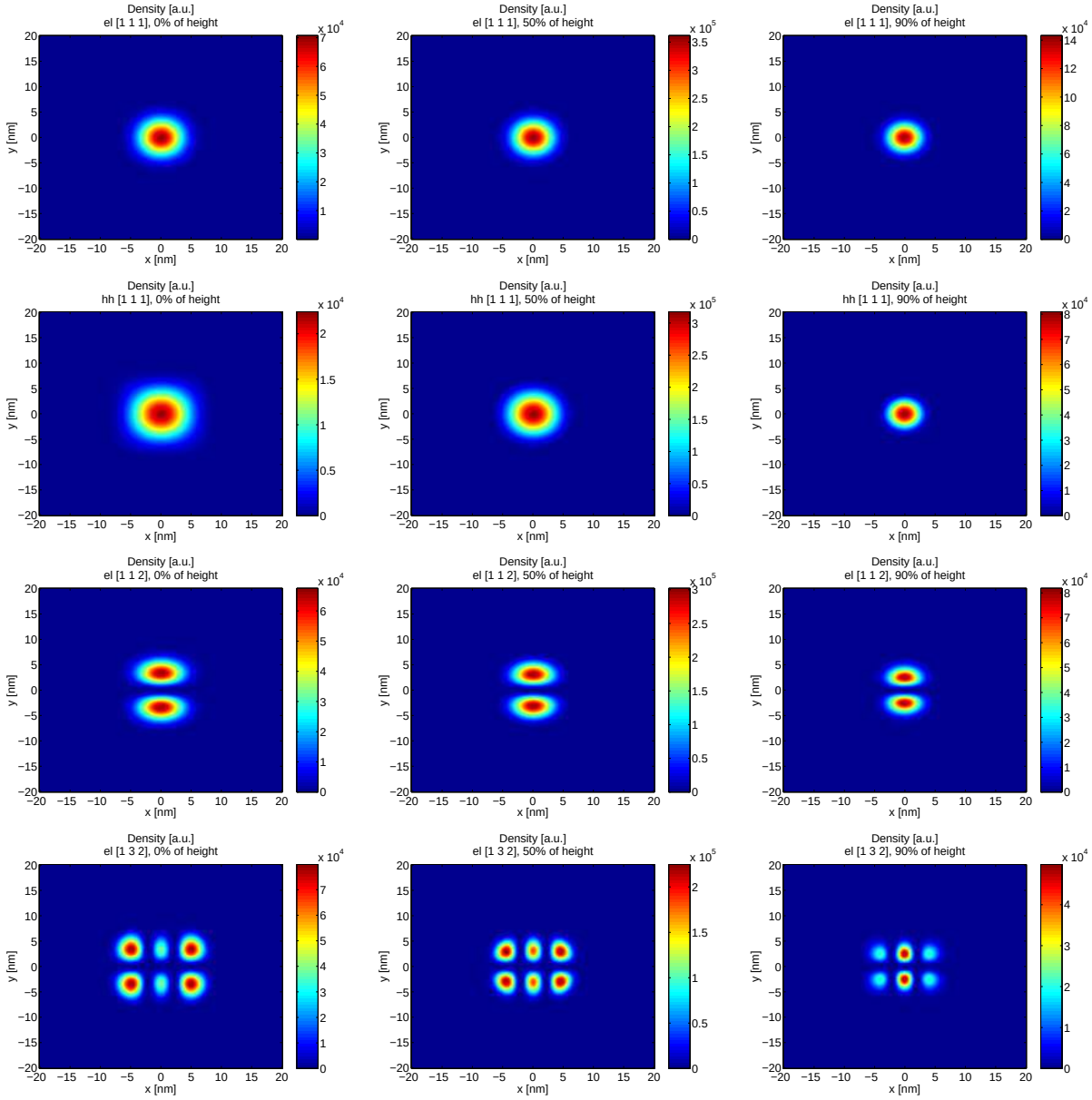

Figure 3.28: Charge density in the lens-shaped quantum dot of the height of 5 nm and the radius of 10 nm. Planar intersections parallel with the dot plane at the height of the dot basis, mid-height, and top are shown in the first, second and third column, respectively. States with the following quantum numbers are displayed: [111] for electrons (the first row) and heavy holes (the second row), [112] for electrons (the third row), and [132] for electrons (the fourth row).

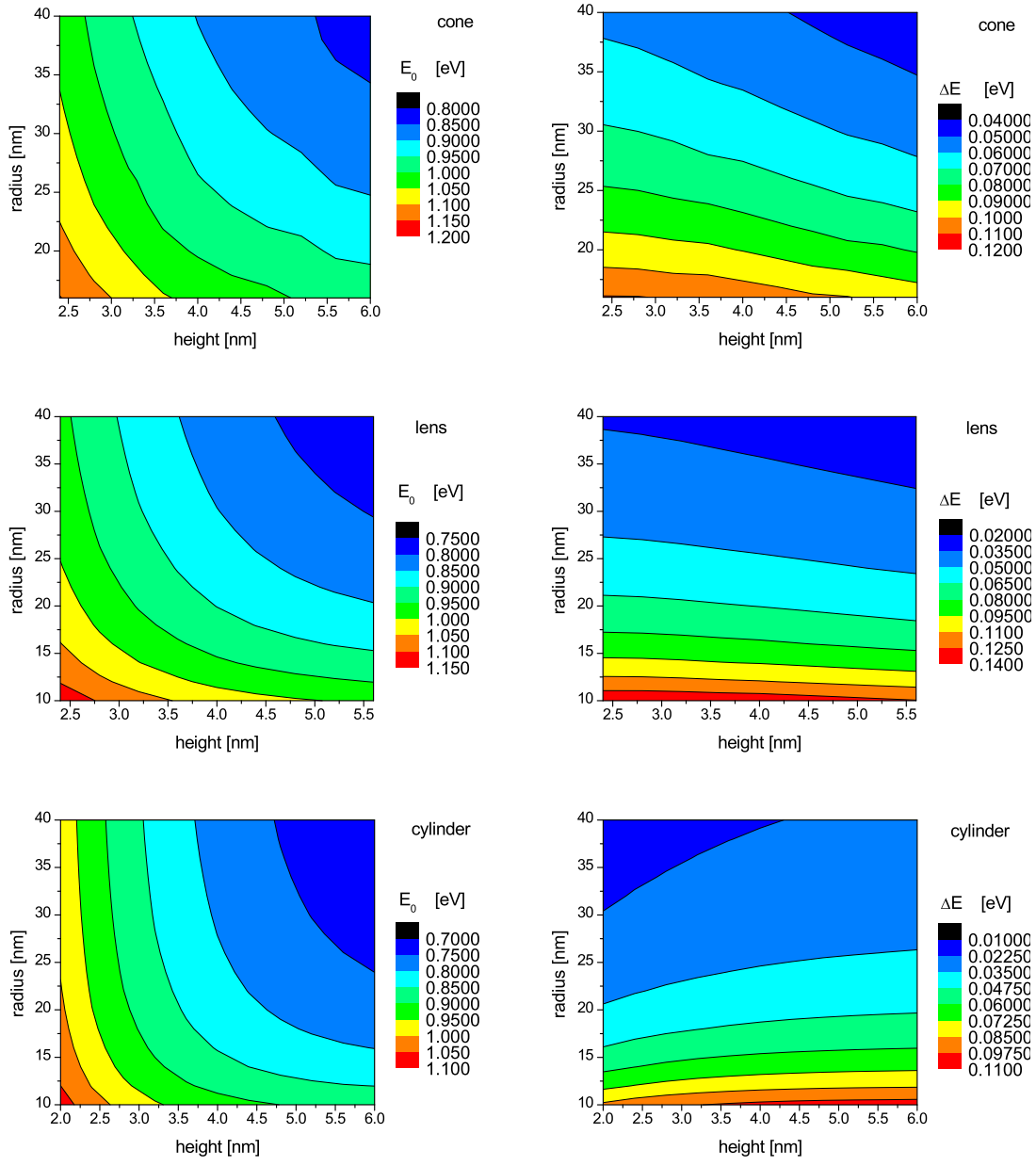

Figure 3.29: Energy of the lowest optical transition (left), and energy separation between two lowest optical transitions (right), calculated for quantum dots with the shape of cone (the first row), lens (the second row), and cylinder (the third row), with various heights and radii.

V increases, but an exception occurs in the second and third column of Table 3.4. In particular, for the dots with the size of $4.0 \times 20\,\mathrm{nm}$ (the second row) both volume and energy are lower than for dots with the size of $2.8 \times 30\,\mathrm{nm}$ (the third row). This is due to the fact that the three confinement directions are not equally important. The lateral confinement is much weaker than the vertical one; a modification of the radius causes much smaller energy shift than a modification of the height. For dots with identical volume, those with a higher aspect ratio, $A = h/(2r)$, have lower energies E_0. For dots with identical aspect ratio, those with higher volume have lower energies E_0. These trends are illustrated in Figures 3.30 and 3.31.

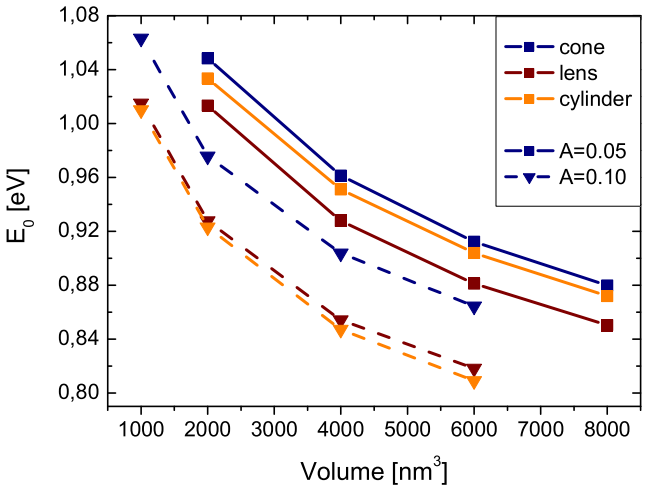

Figure 3.30: The lowest transition energy E_0 calculated using VTWA for several dot volumes, aspect ratios (A) and shapes. The energy decreases as both volume and aspect ratio increase.

3. The ordering of E_0 for identical volume and aspect ratio and various shapes is illustrated in Figure 3.31. In general, the wave function tends to be compact in order to minimize the kinetic energy; for example, the wave function does not extend to the tip and the basis perimeter of the cone. It favors compact shapes, such as the cylinder over extended shapes such as the cone, and the energy decreases when moving from the cone to the lens and to the cylinder. However, for very flat dots (aspect ratio fairly below 0.1), the height-dependent vertical confinement becomes crucial. Since the height of the cylinder is the lowest among all considered shapes, the energy in the cylinder becomes higher than in the lens (while the energy in the cone remains the highest).

4. The energy separation between the two lowest transitions ΔE is determined primarily by the dot radius (see Fig. 3.29). This fact is quite obvious: the separation is practically identical to the lateral excitation energy, which is determined by the lateral dimension.

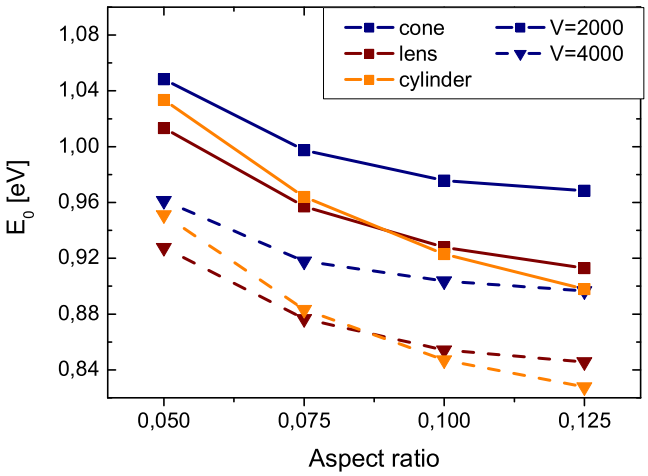

Figure 3.31: The lowest transition energy E_0 calculated using VTWA for several aspect ratios, dot volumes (V, in nm^3) and shapes.

5. The dot height influences the separation ΔE in two ways. First, when increasing the height, the lateral potential well becomes deeper and the lateral excitation energy and separation increase. Second, for large heights, the energy-height dependence is shallower; consequently, the lateral potential well is shallower and the separation decreases. In the case of cone, the second item dominates and the separation decreases as the height increases. In the case of cylinder, the first item dominates (in fact, the profile of the lateral potential is constant and the second item does not take place) and the separation increases as the height increases. For the lens both items approximately compensate each other, the separation is almost independent of the height.

Finally we underline again the two main advantages of our method. First, it provides a reasonable understanding in very simple terms. Second, the calculations are fast, which allows us to explore complex dependencies on many parameters defining the dot system simultaneously. It is however necessary to test the validity of the approximations made here, preferably against more accurate methods. One of the possibilities is proposed in the next section.

3.3 Variational method

Variational method (VM) was originally developed to test the approximations used in VTWA. These approximations can be divided into two parts, concerning either physical model or numerics. Here we keep the identical physical model, i.e., the single band envelope function method, energy dependent effective masses, homogeneous strain field, etc. For the numerical solution of the Schrödinger equation (3.2) we employ the Ritz–Galerkin variational approach, based on an expansion of the wave function into a linear combination of suitably chosen

basis functions. This approach allows to obtain the solution of the Schrödinger equation with arbitrary precision if a sufficient number of the basis functions is used.

Since the main purpose of the method is testing, we restrict ourselves to the dots of shapes with cylindrical symmetry, such as the cone or lens. This restriction enables us to decompose the problem to a set of subproblems according to the magnetic quantum number, which notably improves the performance. Furthermore, together with the approximation of homogeneous strain field, it makes possible to calculate the matrix elements analytically, which again improves the performance and also reduces the numerical errors.

The selection of basis functions should respect the symmetry of the dot. We have chosen so-called Fock–Darwin (FD) functions (the eigenfunctions of two-dimensional harmonic potential) as the suitable basis for the lateral part of the wave function. They read (in polar coordinates)

$$\psi_{FD}^{nm}(\rho,\phi) = \exp(im\phi)\left(\frac{\rho}{l_0}\right)^{|m|}\mathcal{L}_n^{|m|}\left(\frac{\rho^2}{l_0^2}\right)\exp\left(-\frac{\rho^2}{2l_0^2}\right), \tag{3.11}$$

where l_0 is the lateral extension parameter, and $\mathcal{L}_n^{|m|}$ is a (generalized) Laguerre polynomial, for which the following equation holds:

$$\mathcal{L}_n^m(x) = \sum_{j=0}^{n}\binom{n+m}{n-j}\frac{(-x)^j}{j!}. \tag{3.12}$$

Since this explicit expression is cumbersome, we have used the following recurrent formula in the actual implementation:

$$\mathcal{L}_n^m(x) = \frac{2n+a-1-x}{n}\mathcal{L}_{n-1}^m(x) - \frac{n+a-1}{n}\mathcal{L}_{n-2}^m(x); \quad \mathcal{L}_0^m(x)=1,\ \mathcal{L}_1^m(x)=1+m-x. \tag{3.13}$$

In the vertical direction, we use plane waves, which are universal enough to treat dots with various vertical profiles (cone, lens, cylinder, etc.), and even vertical dot molecules. The lateral part of the wave function is confined to a line segment of finite length centered around the dot. We denote the length of the segment as L_z. The plane waves periodic on this segment form a complete set for all the functions periodic on the segment. Since the wave functions drop rapidly with increasing distance from the dot, they vanish on the segment boundaries and can therefore be considered periodic on the segment. We consequently restrict the basis to the plane waves periodic on the segment of the length L_z.

The complete basis functions read

$$\psi_{VM}^{nmk}(\rho,\phi,z) = \exp(im\phi)\left(\frac{\rho}{l_0}\right)^{|m|}\mathcal{L}_n^{|m|}\left(\frac{\rho^2}{l_0^2}\right)\exp\left(-\frac{\rho^2}{2l_0^2}\right)\exp\left(ik\frac{2\pi}{L_z}z\right), \tag{3.14}$$

where n is a non-negative integer and m, k are integers.

We specify the size of the basis by three numbers, n_{max}, m_{max}, k_{max}, limiting the corresponding basis function indices in the following way:

$$n \in \{0,\ldots,n_{max}\},\quad m \in \{-m_{max},\ldots,m_{max}\},\quad k \in \{-k_{max},\ldots,k_{max}\}. \tag{3.15}$$

The basis size is therefore

$$N = (n_{max}+1)(2m_{max}+1)(2k_{max}+1). \tag{3.16}$$

The trial wave function is expressed as

$$\psi_{TR}(\rho,\phi,z) = \sum_{n=0}^{n_{max}} \sum_{m=-m_{max}}^{m_{max}} \sum_{k=-k_{max}}^{k_{max}} c_{nmk}\psi_{VM}^{nmk}(\rho,\phi,z). \tag{3.17}$$

Inserting ψ_{TR} into the Schrödinger equation 3.2, multiplying both sides by complex conjugates of basis functions ψ_{VM}^{nmk*}, integrating over the volume, and using the orthonormality of the basis functions, we obtain the following set of algebraic equations for the energy and coefficients:

$$\sum_{n_2 m_2 k_2} \langle\psi_{VM}^{n_2 m_2 k_2}|H|\psi_{VM}^{n_1 m_1 k_1}\rangle c_{n_1 m_1 k_1} = E\delta_{(n_2 m_2 k_2),(n_1 m_1 k_1)}. \tag{3.18}$$

Here H is the Hamiltonian, and $\langle\psi_{VM}^{n_2 m_2 k_2}|H|\psi_{VM}^{n_1 m_1 k_1}\rangle$ are its matrix elements. It is clear that the energies of bound states are eigenvalues of the Hamiltonian, and the expansion coefficients of the wave functions are eigenvectors of the Hamiltonian.

The calculation of the matrix elements is rather tedious; we omit the details here and review only some general features. First, due to the rotational symmetry of both Hamiltonian and basis functions, the Hamiltonian matrix has a block diagonal form with each block belonging to a unique value of the magnetic quantum number m. This enables a decomposition of the $N \times N$ matrix eigenvalue problem to the set of $2m_{max}+1$ eigenvalue problems for $N/(2m_{max}+1) \times N/(2m_{max}+1)$, which considerably speeds up the calculations. The in-plane integration can be performed analytically, and the only numerics used for the calculation of matrix elements is related to the vertical integration. The complexity of the matrix element calculations is dramatically reduced. The most time-consuming part of the calculations is then the diagonalization of matrices.

The choice of the basis functions is a trade-off between universality and performance. The lateral component is well suited for a particular class of the systems with cylindrical symmetry: it enables the matrix decomposition, the analytical evaluation of the matrix elements, and provides a fast convergence. On the other hand, an extension to different dot shapes would be difficult; we therefore omit many interesting classes of quantum dot shapes, such as laterally elongated dots, or dots with a rectangular basis. On the contrary, the choice of the vertical component enables us to treat various vertical dot profiles or even interacting vertically stacked dots at the trade-off of slower convergence and the necessity of the numerical integration.

The variational method serves here several purposes. First, it is used for the testing and assessment of VTWA. It can be also used to improve the results obtained from VTWA, with the restriction to the dot shapes of cylindrical symmetry. This is in particular important for tall dots, since VTWA is not intended for treating them and leads here to serious inaccuracies. Owing to the choice of the vertical component of the basis functions, it is also possible to treat vertically stacked quantum dots. The magnetic field parallel with the axis of rotation can be easily included into the model, which further extends the application possibilities. On the other hand, there are two disadvantages with respect to VTWA: the increase of complexity and the loss of generality (i.e., the restriction to the cylindrically symmetric quantum dots).

In the following, we discuss the accuracy of the method, and compare its results with those of VTWA. The basis functions are determined by the lateral extension parameter l_0 and by the vertical periodic size L_z. The accuracy of the solution is further influenced by the basis size, i.e., by the parameters n_{max}, m_{max}, k_{max}. All the results below have been obtained for

the lens shaped dot with the height of 5 nm and the radius of 10 nm, unless stated otherwise. Since the calculations are fairly time-consuming, we have solved the Schrödinger and the mass equations self-consistently for the ground state only, and used the ground state value of the effective mass also for the excited states. The basis size is denoted as $n_{max}\, m_{max}\, z_{max}$.

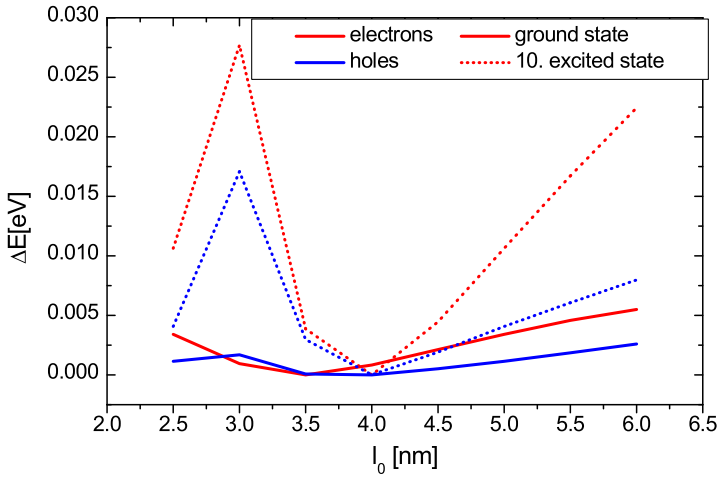

Figure 3.32: The energy of the ground state, and the tenth excited state for both electrons and heavy holes in the lens-shaped quantum dot with the height of 5 nm and the radius of 10 nm calculated using VM with the basis size 4 4 6 for several values of the parameter l_0.

A proper choice of the lateral extension parameter can considerably improve the accuracy of the solution. The Fock–Darwin solution to the two-dimensional harmonic potential provides the value of the parameter

$$l_0 = \sqrt{\frac{\hbar}{\omega m_0 m^*}}, \tag{3.19}$$

where ω is the harmonic frequency and m^* is the effective mass expressed in units of free-electron mass m_0. For the lens-shaped quantum dot with the height of 5 nm and the radius of 10 nm, we obtain $l_0 = 3.5$ nm for electrons and $l_0 = 4.0$ nm for heavy holes. It is however advantageous to use the same values for electrons and holes in order to simplify the calculations of transition matrix elements. Figure 3.32 displays the calculated energies of electron and hole states for several values of l_0. We observe that for ground states the dependence is quite shallow, with the difference up to 5 meV for l_0 ranging from 2.5 nm to 6 nm, which justifies the use of the same l_0 for both electrons and holes. For the tenth excited state, the difference is considerably higher (up to 25 meV) due to more complex shape of the corresponding wave functions with rapid oscillations inside the dot volume. However, the highly excited states are usually of no particular interest. Consequently, we set the value of l_0 to approximately one half of the dot radius in the following.

The value of L_z has to be large enough in order the wave function vanishes at the boundaries, and small enough in order to keep the number of the plane waves necessary to describe the bending and oscillations of the wave function inside the dot volume reasonably small. In

most cases we use such a value that the wave function decreases by a factor e^5 from the dot boundary to the segment boundary.

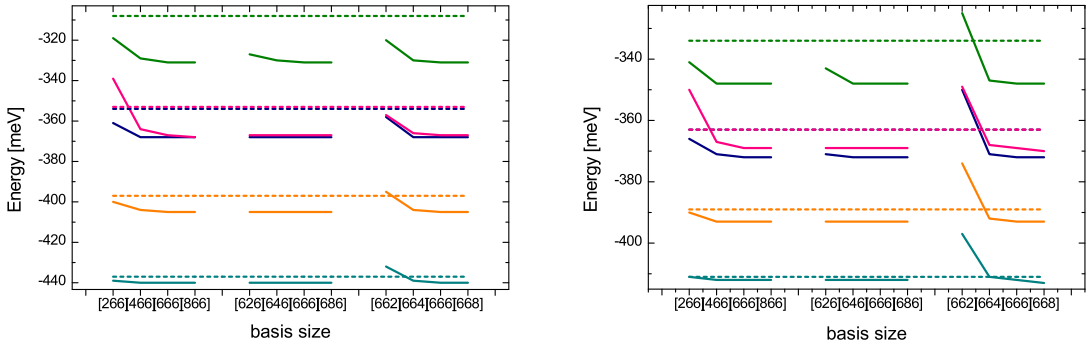

Figure 3.33: The bound state energies of electrons (left panel) and heavy holes (right panel) in the lens-shaped quantum dot with the height of 5 nm and the radius of 10 nm, calculated using VM with several basis sizes (solid lines), and using VTWA (dashed lines). Corresponding energy levels are denoted by the same color. From the three parameters determining the basis size, two are left constant and only one is varied: n_{max} in the left part of both panels, m_{max} in the middle part, and k_{max} in the right part of both panels.

To study the effect of varying basis size, we have calculated the energy levels of electrons and heavy holes in the lens shaped dot of the height of 5 nm and the radius of 10 nm. The values of the three parameters determining the basis size, i.e., n_{max}, m_{max}, and k_{max}, were systematically varied: the values of two parameters were set to 6, and the value of the third parameter was varied from 2 to 8. The results are shown in Figure 3.33; for comparison, the energies obtained from VTWA are also displayed there. The computational time for the smallest basis size was comparable to the VTWA method (several minutes), it was considerably larger (several hours) for the largest sizes.

The effect of varying m_{max} is simple: due to the symmetry, each wave function is labelled with a certain value of m, and is composed of the basis functions with the same m only. The value of m_{max} has therefore no effect on the accuracy of the results, it only determines, which levels will be calculated. In this test, however, we did not decouple the matrix explicitly, and some mixing in m is observed for excited states resulting from numerical errors. In the following calculations explicit decoupling of the Hamiltonian matrix to submatrices has been used, which fixed the problem.

As n_{max} is increased, we observe a fast convergence. The lowest states are determined with an accuracy better than 1 meV for $n_{max} = 4$, other states considered here require at most $n_{max} = 6$. This confirms our assumption that the Fock–Darwin functions are well suited for the description of the dots of cylindrical symmetry. Of course we have to keep in mind that the value of l_0 has to be set properly. The excited states require higher n_{max} since the shape of their wave functions is more complex. This is particularly important for the d-state with dominating $m = 0$ (depicted by the pink color in Fig. 3.33), for which the radial excitation is

significant, i.e., it is composed of basis functions with non-zero n. Lower states contain rather polar excitations, i.e., they are composed of basis functions with non-zero m.

Despite of the Fock–Darwin functions, the plane waves were not chosen due to their convergence properties, but rather due to their generality. It is therefore necessary to use many plane waves (large k_{max}) to obtain convergence. This is illustrated by two facts in Fig. 3.33: First, the energies for low k_{max} are distinctly above the converged value, even above those obtained from VTWA. Second, even for $k_{max} = 8$ the ground hole state has not converged, there is an energy shift larger than 1 meV when modifying k_{max} from 6 to 8. On the other hand, the electron levels are well converged for $k_{max} = 6$. This fact is explained by the effective mass, which is considerably higher for holes than for electrons. The low effective mass of electrons increases the importance of the kinetic energy, which excludes rapidly oscillating plane waves with high k from the wave function expansion. The high effective mass of holes increases the importance of the potential energy, and the wave function tends to fill the dot volume; its shape is more complex and more plane waves are required to describe it with a good accuracy.

The fast lateral and slow vertical convergence can also be illustrated in a different way. Each state can be classified by three quantum numbers which are prevailing in its expansion. For the ground electron state, the following values are prevailing: $n = 0$ with the large rate of 78 %, $m = 0$ with the rate of 100 %, $k = 0$ with the rate of 47 % only. For the ground hole state, the following values are prevailing: $n = 0$ with the large rate of 71 %, $m = 0$ with the rate of 100 %, $k = 0$ with the rate of 32 % only. Indeed, the mixing of basis states differing in k is more pronounced than of those differing in n (while those differing in m do not mix at all), which means that a large k_{max} is required to model the realistic wave functions properly.

The energies obtained from VM for the basis size of 6 6 6 were always lower than the energies obtained from VTWA, as is expected. We remind here that the energies from VTWA are obtained as mean values of the Hamiltonian operator for a trial wave function (if the correction terms are included to the calculations), the same holds for VM. We know from the variational principle that the eigenfunctions minimize the Hamiltonian mean value, with the condition of orthogonality for excited states. It means that each energy calculated as the Hamiltonian mean value for some wave function is always above the corresponding eigenenergy. Increasing the basis size improves the trial function and leads to lower energies; for a certain basis size they have to be lower than those obtained from VTWA. The size of the basis for which the energies obtained by both methods cross assesses the quality of the trial wave function of VTWA. We can conclude that VTWA is better than VM for the basis size $2\,m_{max}\,4$, but worse than VM for the basis size $2\,m_{max}\,6$ or $6\,m_{max}\,4$ (as already mentioned, the value of m_{max} does not play any role in the accuracy of the results).

We proceed with the quantitative comparison of VM with the basis size of 6 6 6 and VTWA. The ground state energies of both electrons and holes differ as little as by 1 meV. The agreement between the excited states is slightly worse: the first excited energy differs by about 2 meV for both electrons and holes. We note here that the considered dot is fairly tall, and therefore not treated very well by VTWA. Such differences are entirely acceptable compared with other uncertainties and inaccuracies which enter the modeling. The differences including the higher states are visualized in Figure 3.34, where the optical response function (i.e., the joint density of states multiplied by the transition probability) obtained from the calculations using VM and VTWA. There are significant differences occurring for higher transitions; however, such transitions are rarely important from the experimental or

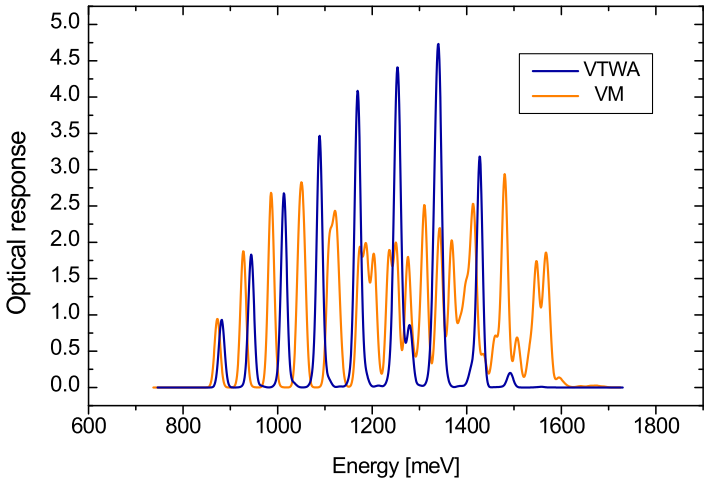

Figure 3.34: Joint density of states multiplied by the transition probability (i.e., "optical response") in the lens-shaped quantum dot with the height of 5 nm and the radius of 10 nm, obtained from VM model with the basis size of 6 6 6, and from VTWA model. Each single-particle δ-function has been replaced by a 10 meV FWHM Gaussian of unit amplitude for better legibility.

application point of view, particularly due to the fact that the corresponding levels are not usually populated.

The very good agreement of VM and VTWA for the lens-shaped dot with the height of 5 nm and the radius of 10 nm discussed in the previous paragraph might be incidental. We have therefore calculated the energy levels in four lens-shaped dots with the heights of 2 and 3 nm and the radii of 15 and 30 nm. The aspect ratio of these dots varies between 0.03 and 0.10, being substantially smaller than that of the original dot (0.25); we therefore expect even a better accuracy of VTWA here. The basis size used in the VM calculations was 10 2 12. The results are as follows: The lowest transition energies calculated by VTWA are surprisingly lower than those obtained from VM, with the difference up to 3 % (38 meV). The difference decreases as the dot height or the dot radius increases. Since the energies in both methods are the mean values of Hamiltonian, the lower value should represent the better approximation and VTWA is found to be superior to VM for the considered dots. This is indeed an unexpected result, meaning that either VM has not fully converged, or some numerical error influences its results. The origin of this behavior is not fully understood yet.

The agreement of both methods for the taller lens-shaped dot with the height of 5 nm and the radius of 10 nm has therefore be classified as incidental. VM gives always higher energies than the true value, VTWA is not very accurate for tall dots, and gives also higher energies. Both values have therefore met incidentally for a particular dot system, although the true value might be several tens of meV lower.

Concluding this comparison, we have found that VTWA performs better than VM for very flat dots. We therefore cannot test the accuracy of VTWA by the comparison with VM. However, we believe that the results provided by VTWA are rather accurate since the

correction terms are fairly low. Furthermore, the inaccuracy of several tens of meV is still fairly below the typical inaccuracies introduced in other approximations. Both methods are therefore suitable for modeling of the quantum dots.

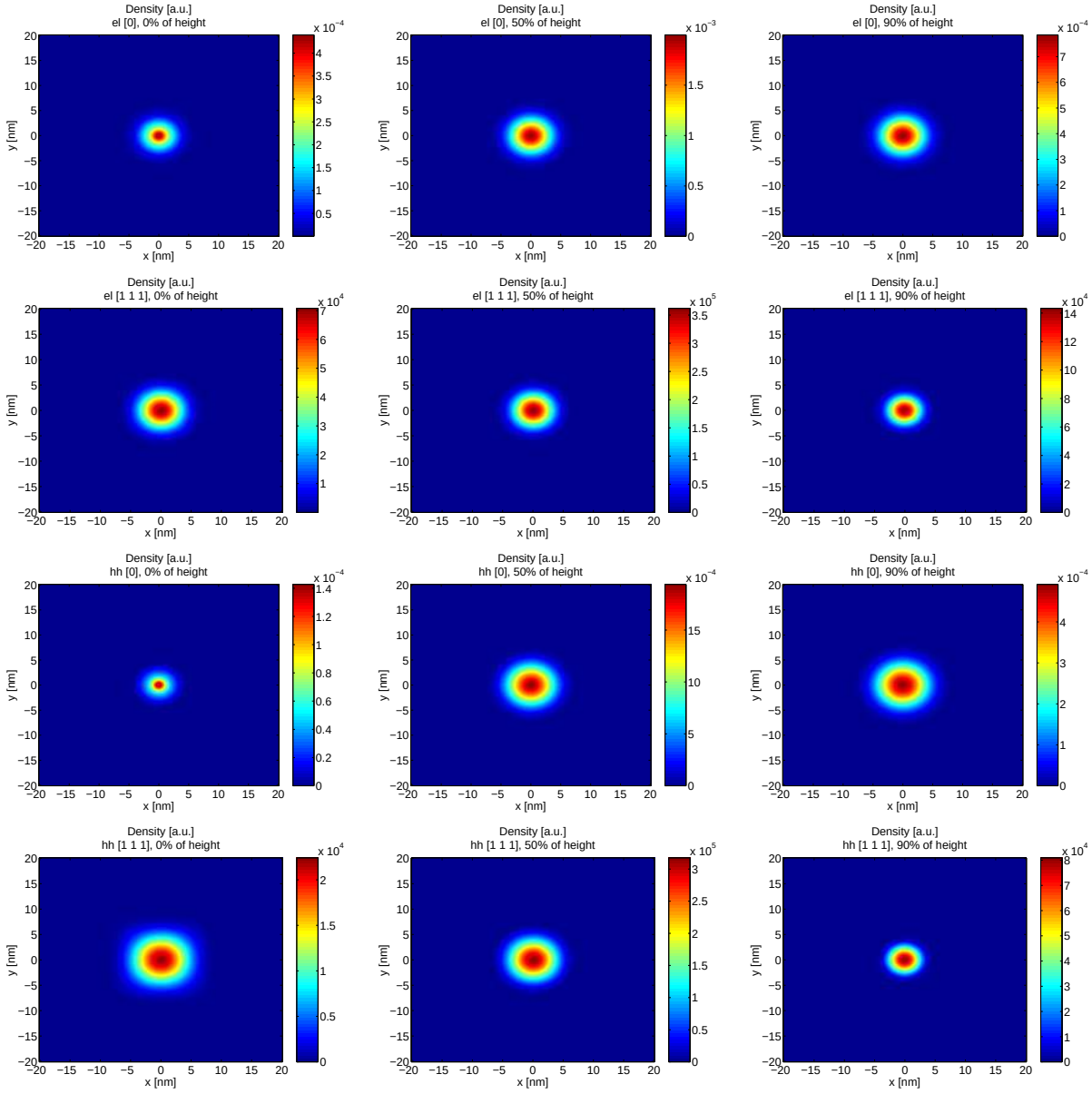

Figure 3.35: Charge density in the lens-shaped quantum dot of the height of 5 nm and the radius of 10 nm. Planar intersections parallel with the dot plane at the height of the dot basis, mid-height, and the top are shown in the first, second and third column, respectively. Ground states are displayed: for electrons (VM – first row, VTWA – second row) and heavy holes (VM – third row, VTWA – fourth row).

Finally we turn our attention to the charge densities in the lens-shaped quantum dot of the height of 5 nm and the radius of 10 nm. The comparison of the results obtained using VM and VTWA is shown in Figure 3.35. We display there values in planar intersections parallel with the dot plane at the height of the dot basis, mid-height, and the top (0 %, 50 %, and 90 % of the dot height, respectively) for the ground electron and heavy hole states. We omit the comparison of the excited states since they are often degenerate and the comparison would require a transformation to the equivalent bases. The vertical profiles of the densities along the dot axis obtained by both methods are similar. For example, the ground electron state density along the dot axis has its maximal value at the mid-height, the value at the dot basis is approximately 20 % of the maximum and the value at the top is approximately 40 % of the maximum. The ground heavy hole state density drops more rapidly towards the dot boundaries; the value at the dot basis is approximately 8 % of the maximum and the value at the top is approximately 25 % of the maximum. No significant differences in the density profiles along the dot axis between VM and VTWA have been observed. On the other hand, there is a pronounced difference in the lateral extension of the density: as we move the plane of the intersection upwards, the lateral extension of the density decreases for VTWA and increases for VM. Since the lateral dimension of the dot decreases when moving the plane of the intersection upwards, the first option (which holds for VTWA) is more physical. It also agrees with our observation that VTWA is superior to VM when applied to flat dots. The origin of the observed inverse dependence of the lateral extension on the intersection position for VM is unclear.

In conclusion, comparing it with VM, we have proved that VTWA is a plausible method to obtain the energies of several lowest bound states in quantum dots with aspect ratios below 0.25. Applications of VM to vertical dot molecules and to dots in magnetic field will be described in Chapters 4 and 6, respectively.

3.4 Eight band k.p model developed at TU Berlin

The method (8kpTUB) discussed in this section outreach significantly those described so far in both accuracy and complexity. It was developed by several scientists (M. Grundmann, O. Stier, A. Schliwa, V. Mlinar, M. Winkelnkemper, and D. Bimberg) at Technische Universität Berlin and it is very thoroughly described in numerous scientific papers, and, in particular, in the doctoral theses of Oliver Stier [91] and Andrei Schliwa [85].

The most prominent features of 8kpTUB are summarized below:

- The general concept of the model is a discretization. The continuous infinite space is first restricted to a finite area, in which the probability of finding a particle is non-negligible, and afterwards replaced by a discrete grid. It enables the transformation of the differential equations describing the problem to sets of algebraic equations, which are solved by standard iterative methods. An important consequence of this approach is an equal treatment of the dot shape, contrary to the VM or VTWA, which were best suited for (or even limited to) a certain class of the dots (with cylindrical symmetry or flat, respectively).

- The strain field is calculated by the minimization of the total strain energy for the system. The numerical solution of corresponding differential equations is obtained using the finite differences method.

- First- and second- order piezoelectric field is calculated from the strain field using the expressions described in Section 2.4. The piezoelectric charge is determined by Eqs. 2.47, 2.48, and 2.50. The piezoelectric potential can be in principle expressed analytically in the form of integral of the piezoelectric charge; however, the evaluation would be very time-consuming. Instead, the integral is evaluated only on the boundaries of the grid and inside the grid the Laplace equation is solved to obtain the potential. Furthermore, only a small part of the grid points with the highest charge density enters the integration; by experience, 2 % of the grid points contain 90 % or more of the total charge.

- If desirable, external fields can be added to the Hamiltonian. The electric potential is added to the Hamiltonian potential term, the magnetic field is introduced via the Peierl's substitution in the momentum operator and an addition of the Zeeman term.

- The total Hamiltonian is composed of several parts: the Luttinger eight-band $\vec{k} \cdot \vec{p}$ Hamiltonian (2.10), the Bir-Pikus strain Hamiltonian, the piezoelectric term, and, if desirable, the contribution of external fields.

- The eigenvalues and eigenfunctions of the Hamiltonian corresponding to the bound state energies and wave functions are found using a specialized diagonalization method developed for this purpose with a great care by Oliver Stier. The method is unfortunately described in his thesis only [91], since none of all the scientific journals was ready to accept a lengthy, although excellent paper.

- The multiparticle states are calculated using configuration interaction method. The calculations involve a contribution of direct Coulomb interaction, exchange interaction, and correlation. Knowing the multiparticle states energies and wave functions, it is possible, in principle, to retrieve arbitrary physical property of the considered quantum dot.

It is beyond the scope of this work to explore the properties of 8kpTUB in more detail. However, it is interesting to use it for a comparison with VTWA (and for an estimation of VTWA accuracy). Such a comparison could be of course very complex; however, we believe that the application of the methods to realistic physical problems is far more interesting. We therefore restrict ourselves to a very brief comparison, whose purpose is rather illustrative.

We state some conditions of the comparison first. One point is that both methods are suitable for different dot types. As already mentioned, VTWA is designed for flat dots. On the other hand, 8kpTUB requires comparable lateral and vertical dot dimensions. It is either slow or inaccurate otherwise (this is, in fact, a matter of the implementation only, since an identical grid step is used for all directions). In comparing the methods, we are therefore limited to dots with the aspect ratio of about 0.2. Further, the material parameters used in both methods are not necessarily identical. For example, effective masses in VTWA are set by approximating the real band structure in a close vicinity of the Γ-point, while the Luttinger parameters in 8kpTUB are set by approximating the band structure in a considerably larger volume of k-space. Such differences are forced by the nature of both methods. We have therefore treating them as blackbox methods to obtain the results, omitting their inner structure.

Two systems were chosen for the comparison. The first one is the lens-shaped dot with the height of 4.5 nm and the radius of 11.3 nm (aspect ratio 0.2). VTWA predicts the lowest transition energy of 0.985 eV and the lowest transitions separation of 116 meV; 8kpTUB gives 1.044 eV and 85 meV, respectively. The second dot is of the lens shape, with the height of

3.0 nm and the radius of 10 nm (aspect ratio 0.15). VTWA predicts the lowest transition energy of 1.082 eV and the separation of 136 meV; 8kpTUB gives 1.071 eV and 94 meV, respectively. Thus, the differences of the lowest transition energies are below 6 %, which can be considered satisfactory.

Chapter 4

Vertically stacked InAs/GaAs quantum dot structures

The photoluminescence measurements of a series of vertically stacked multilayer quantum dot structures [4] are systematically interpreted here. The analysis of the data taken at various excitation powers and in the magnetic field up to 24 T yields a useful insight into the electronic structure of the InAs/GaAs quantum dot structures. A comparison of the experimental results with the theoretical calculations reveals an increase of the dot dimensions (both height and diameter) and a decrease of the aspect ratio (height/diameter) with increasing number of the quantum dot layers. The increase of the thickness of the spacing layers between adjacent dot layers leads to a decrease of the lateral dimensions of the dots, accompanied by an increase of the aspect ratio and of the energy separation between the ground and first excited transitions. All the experimental data presented here have been provided by collaborators. The results have been partly published [4].

4.1 Introduction

One of the most attractive properties of the InAs/GaAs quantum dot (QD) structures is the efficient emission of near-infrared light. In particular, the band structures of the constituents are well suited for covering the 1.3/1.55 μm range, important in optical communications [45, 100]. These wavelengths are impossible to achieve in quantum well (QW) or single-layer QD InAs/GaAs structures due to the strain-limited dimensions. A promising way to extend the emission to longer wavelengths is the use of vertically stacked QD structures with various number of QD layers. The strain field resulting from the large lattice mismatch leads to a preferential formation of column-like structures of stacked QDs. The multilayer systems have a higher deformation energy, which can eventually lead to the formation of defects. On the other hand, these systems have many important advantages in comparison with single-layer QD structures. Most importantly, they allow to increase the QD size [101, 102] without decreasing significantly their density. Stacked QDs tend to increase the overlap of the optical wave with the electron and hole wave functions in the active region, thus increasing the laser gain and decreasing the threshold current density [103, 104]. Multilayer systems also exhibit a lower inhomogeneous broadening than single-layer systems.

This chapter describes the results of the photoluminescence (PL) studies of a series of multilayer InAs/GaAs QD structures. The origin of the optical transitions is explained using

magnetophotoluminescence measurements (MPL). The electronic structure is calculated for the dot model based on the structural measurements (AFM, TEM). The comparison of the calculated transition energies and the PL data allows us to identify the factors responsible for the increase of the emission wavelength accompanying the increase of the number of the layers.

4.2 Experimental data

A series of vertically stacked InAs/GaAs structures with various numbers of QD layers was provided by by the group of E. Hulicius, Institute of Physics of the Academy of Sciences of the Czech Republic (IP, ASCR). The samples were prepared by low pressure metalorganic vapor phase epitaxy in an AIXTRON 200 apparatus using the Stranski–Krastanow growth mode using the standard growth conditions [105]: Semi-insulating GaAs (100) wafers were used as a substrate. Precursors used for the growth of GaAs and InAs layers were trimethyl-gallium (TMGa), trimethyl-indium (TMIn), and arsine (AsH_3). Prior to the growth, the substrate temperature was held at 800 °C for 5 minutes under AsH_3 flow. The total pressure of 70 hPa and the total flow rate through the reactor of 8 slpm (standard liters per minute) was kept during the growth. The first GaAs buffer layer was grown at 650 °C. Subsequently, the temperature was decreased to 500 °C for the growth of the rest of the structure, consisting of the second GaAs buffer layer, several alternating layers of InAs QDs and GaAs spacer (latter with the thickness of either 3.7 or 7.5 nm), and the GaAs capping layer of a thickness of 22 nm. All InAs layers were deposited under identical conditions: the partial pressure of TMIn of 7.10^{-2} Pa, the V/III ratio of 85, and the growth time of 9 s. After each InAs layer deposition, the growth was interrupted for 30 s to facilitate QD formation.

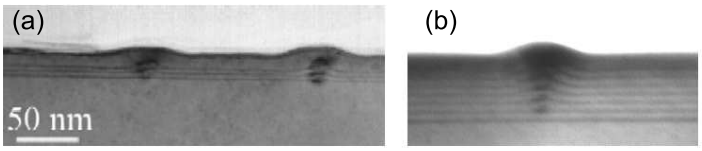

Figure 4.1: TEM cross-sections of (a) a sample with 3 QD layers, spacer thickness 3.7 nm and (b) a sample with 7 QD layers, spacer thickness 7.5 nm. Reprinted from [4].

Examples of TEM cross-sections of samples with three and seven QD layers are shown in Fig. 4.1. The vertical stacking of QDs and the increase of the size of QDs with the increasing number of QD layers are clearly seen. The surface relief observed in the electron micrographs is in a very good agreement with AFM results (Fig. 4.2). The maximum surface density of QDs was about 2.5×10^9 cm^{-2}.

Optical properties of QDs have been studied by photoluminescence at IP, ASCR and by magneto-photoluminescence at Grenoble High Magnetic Field Laboratory. The experimental set-up is in more detail reported in [4]. The magnetic field parallel to the growth direction (Faraday configuration) in the range up to 24 T has been used for MPL [106, 107]. The samples

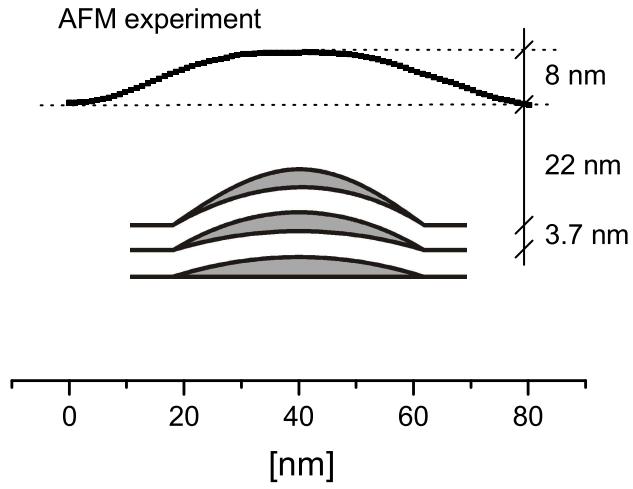

Figure 4.2: The AFM surface profile of 3 vertically stacked QDs with 3.7 nm spacer thickness covered by 22 nm of GaAs, and a model scheme of the underlying QD structure. Reprinted from [4].

were immersed in liquid nitrogen, the increase of temperature at the highest pumping did not exceed 10 K.

PL spectra of the set of samples with the spacer thickness of 3.7 nm and various numbers of QD layers are shown in Fig. 4.3 (a). The most remarkable feature of the series is the shift of the PL signal towards low energy with increasing number of QD layers. The observed spectra can be decomposed fairly well to overlapping Gaussian bands; the two lowest Gaussians are marked by the arrows. The energy of the lowest band and its separation from the next higher band are shown in Fig. 4.3 (b) and (c) as functions of the number of QD layers.

We further discuss the origin of the observed bands. The lowest band corresponds clearly to the transition between the electron and hole ground states in the topmost dot layer (in which the dots are the largest). The first higher band might correspond either to the transition between the excited states in the largest dot, or to the transition between the ground states in smaller dot lying in some deeper layer. The former case will be denoted as the "lateral" excitation, the latter as the "vertical" excitation.

The penetration depth of the pumping light is about 100 nm in GaAs, larger than the total thickness of the 7-layers QD structure with the thicker (7.5 nm) spacer. All dots in stack are therefore populated with carriers. The arguments given in [108] suggest that the carriers thermalize to the lowest-energy states of the largest dots. For higher excitation powers, the intensity of the first higher PL band is approximately twice higher than that of the lowest band, as demonstrated in Fig. 4.3 (a) for the 5-layers QD sample. This can be explained by the higher joint density of states for the higher transition, which corresponds to the excited states in the largest dots – there are two transitions between them with similar energy, resulting in twice larger density of states than for the lowest transition [109]. These observations therefore supports the case of "lateral" excitation.

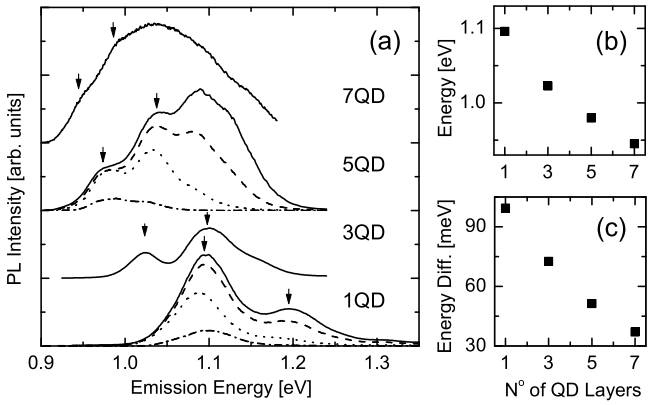

Figure 4.3: (a) PL spectra of samples with 1, 3, 5 and 7 QD layers and spacer thickness 3.7 nm. Spectra of 1 and 5 QD layers are shown for various values of the excitation density: 500 W/cm^2 (solid line), 300 W/cm^2 (dashed), 125 W/cm^2 (dotted) and 5 W/cm^2 (dash–dotted). (b) The lowest transition energy as a function of the number of layers. (c) Energy difference between the two lowest PL bands ΔE_{sp} as a function of the number of QD layers. Reprinted from [4].

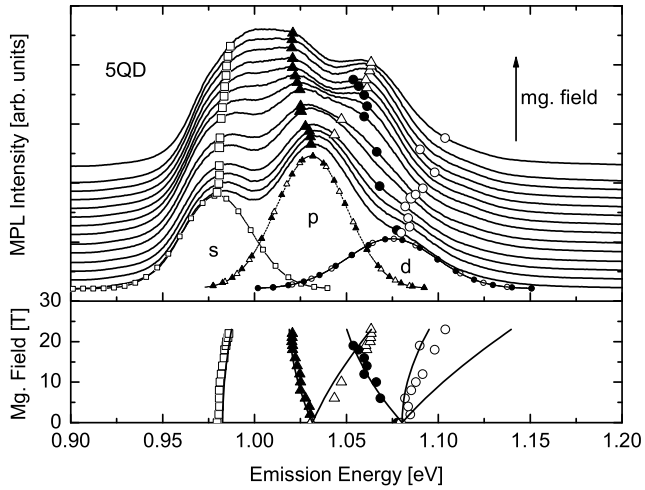

Figure 4.4: Upper panel: magneto-photoluminescence spectra (for the magnetic field from 0 to 24 T) of the 5-layers QD sample, spacer thickness 3.7 nm. Individual spectra are shifted vertically. The zero-field spectrum is decomposed into three Gaussian bands, labelled s, p, and d. The positions of the band maxima are shown as the open squares (s-band), solid and open triangles (lower and upper component of the p-band) and solid and open circles (lower and middle component of the d-band). Lower panel: band positions calculated from the Fock–Darwin model (solid lines), and the best resolved components of the Gaussian representation of experimental spectra (symbols). Reprinted from [4].

Further insight into the origin of the multi-band PL spectra is provided by the MPL measurements. The spectra observed on the 5-layers QD sample with the spacer thickness of

3.7 nm are shown in Fig. 4.4 . With increasing magnetic field, the lowest PL band (0.98 eV at B = 0 T) displays a diamagnetic shift, while the next higher band (1.03 eV at B = 0 T) splits into two clearly resolved bands. This is an evidence of the p-like character of this transition [110, 111, 112] and it proves conclusively, that the individual PL bands of these samples do not originate in QDs of different sizes, which are present in separate layers. The zero-field spectrum can be represented rather well by a sum of three Gaussian profiles shown in the upper panel of Fig. 4.4. With increasing magnetic field, the decomposition becomes more difficult due to the larger number of broad, overlapping bands. Nevertheless, multiple bands can be resolved fairly well in some of the spectra. The resulting band positions are also shown in Fig. 4.4, and the expected transition energies are plotted in its lower panel. The s-, p- and d-energy levels were calculated by a simple one particle Fock–Darwin model [113, 114] for a particle confined in a two-dimensional parabolic well in an external perpendicular magnetic field, in effective mass approximation [111]. The motion of such particle is described by the Hamiltonian

$$H = \frac{p^2}{2m^*} + \frac{1}{2}m^* \left(\omega_0^2 + \frac{1}{4}\omega_c^2\right) r^2 - \frac{1}{2}\omega_c l_z \,, \tag{4.1}$$

where m^* is the effective mass, $\vec{r}$ is the position, $\vec{p}$ is the momentum, $l_z = xp_y - yp_x$ is the projection of the angular momentum onto the field direction, ω_0 is the harmonic potential frequency, $\omega_c = eB/m^*$ is the cyclotron frequency. Two quantum numbers, n_+ and n_-, determine the eigenenergies (Fock–Darwin levels) of this Hamiltonian corresponding to the states $|n_+ n_-\rangle$:

$$\epsilon\,(n_+ n_-) = \hbar\omega_+ \left(n_+ + \frac{1}{2}\right) + \hbar\omega_- \left(n_- + \frac{1}{2}\right), \quad \text{where } \omega_\pm = \sqrt{\omega_0^2 + \frac{1}{4}\omega_c^2} \pm \frac{1}{2}\omega_c \,. \tag{4.2}$$

Adjusting ω_0 to the observed separation of the lowest PL band from the next higher band (51 meV), we obtain the effective mass of the exciton of $0.06\, m_0$.

The magnitude of the observed red shift of the lowest PL band when increasing the number of QD layers from 1 to 7 is about 150 meV, see Fig. 4.3 (b). This shift is primarily due to the increasing size of the dots in the topmost layer observed in the TEM cross-sections (Fig. 4.1).

Increasing number of QD layers at a constant GaAs spacer thickness causes the decrease of the energy difference ΔE_{sp} shown in Fig. 4.3 (c). This is a rather serious disadvantage for lasing structures since it leads to an undesirable increase of the occupation of higher excited states. However, an increase of the spacer thickness can enhance the band separation at comparable values of the lowest transition energies, see Fig. 4.5. This behavior can be explained by different dimensions of QDs in structures with different spacer thicknesses as discussed in the following.

4.3 Electronic states

The single-dot energy levels and transition energies are retrieved using the variable thickness well approximation. The method is thoroughly described in Sec. 3.2. The lowest transition energies and their separations from the first higher transition energies calculated for several dot shapes and sizes are depicted in Fig. 3.29.

The single-dot energy levels are shifted by the vertical interaction of the dots in the multi-layer system. This shift depends strongly on the thickness of the spacer layer. The TEM images (Fig. 4.1) indicate a uniform thickness of the spacer over the profile of the underlying

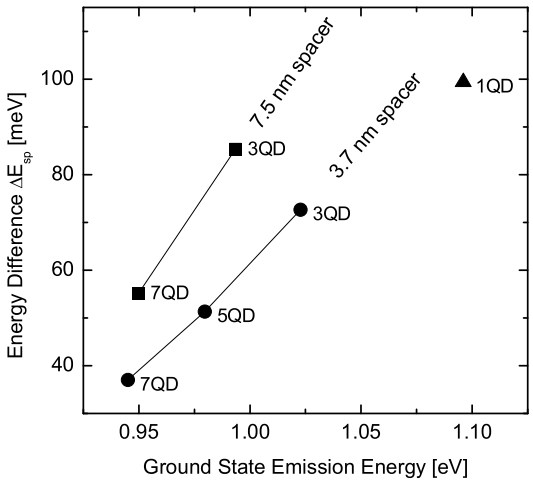

Figure 4.5: Energy difference ΔE_{sp} versus the lowest transition energy, experimental data. Reprinted from [4].

dots. This assumption is further supported by the surface relief seen in AFM (Fig. 4.2), which is for multilayer systems markedly higher than the height of a single-dot (determined from fitting of the calculated energy structure to the PL band positions), and only slightly lower than the corresponding multiple of the height of the individual dots. We therefore assume the distance between the dots to be equal to that of the wetting-layer regions, i.e., 3.7 and 7.5 nm for the two series of the samples, respectively. We also assume the same sizes of all dots in the stack in order to reduce the number of free parameters of the model. The magnitude of the energy shift of two lowest transitions depends only very weakly on the dot radius. In fact, within the range of the radii from 10 nm to infinity (i.e., to the quantum well limit) it varies less than 2 meV (1 meV) for the spacer thickness of 3.7 nm (7.5 nm), respectively, considering the three-layer system with the dot heights of 2 and 5 nm. This fact allows us to replace the vertically stacked dots by coupled wells for the determination of the energy shift, which leads to much faster computations. The magnitude of the shift for the dot heights from 2 to 5 nm in the 3– to 7–layer systems is found to be between 4 and 25 meV (0.2 and 2.5 meV) for the spacer thickness 3.7 nm (7.5 nm), respectively.

We illustrate the conclusions of the previous paragraph by discussing the case of three identical stacked dots with the heights of 2 nm and the radii of 30 nm, see Figure 4.6. The two lowest transition energies in the single dot (corresponding to the spacer layer of infinite thickness), calculated using the VM (Sec. 3.3), are 1.061 and 1.110 eV. The transitions split into triplets in the system of three dots separated by the finite spacer. Their energy ranges are 1.054 – 1.075 eV and 1.103 – 1.126 eV for the spacer thickness of 5 nm, and 1.032 – 1.111 eV and 1.083 – 1.162 eV for the spacer thickness of 3 nm; they extend as the spacer thickness decreases. The calculations have been repeated for the system of three corresponding quantum wells of the thickness of 2 nm. The lowest transition energy in the single well is 1.011 eV, resulting in the lateral confinement energy of 50 meV for the lowest transition 99 meV for the next higher transition in the dot. Adding this energy to the energy ranges for the transitions in wells

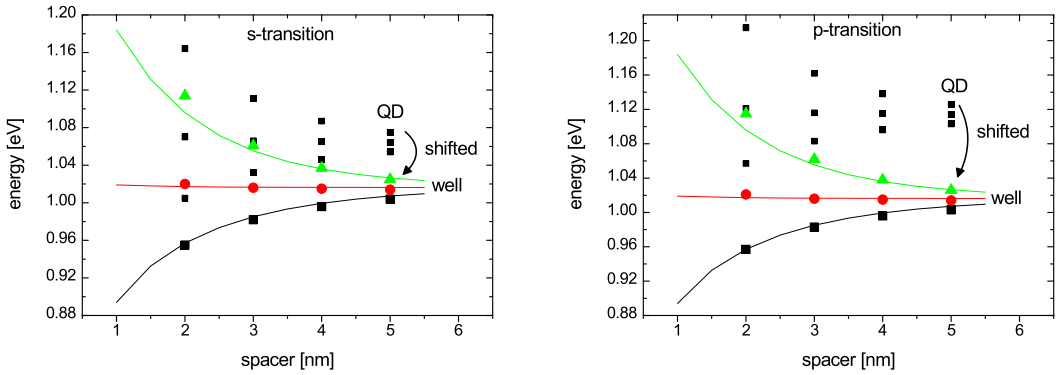

Figure 4.6: The transition energies in the system composed of three identical quantum dots with the heights of 2 nm and the radii of 30 nm, are displayed as functions of the spacer layer thickness by small squares (original values) and by symbols (after subtracting the lateral confinement energy). The transition energies in the corresponding system composed of three identical quantum wells with the thicknesses of 2 nm are displayed by lines. The left panel shows the lowest transition (s-transition), the right panel the next higher transition (p-transition).

results in the energy ranges for the lowest transition triplet and next higher transition triplet of 1.057 – 1.076 eV and 1.106 – 1.125 eV for the spacer thickness of 5 nm, and 1.035 – 1.105 eV and 1.084 – 1.154 eV for the spacer thickness of 2 nm. The differences between these ranges and those calculated directly for the dots are up to 8 meV.

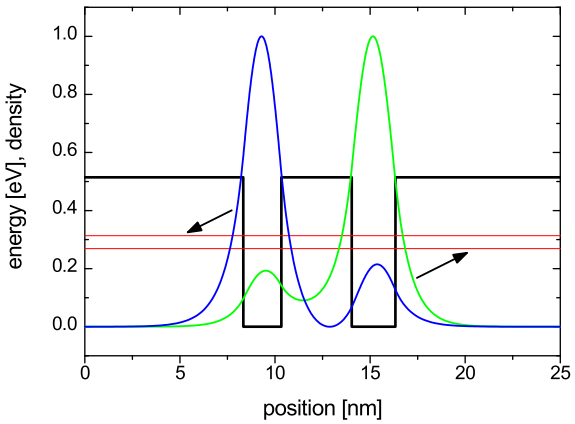

Figure 4.7: The energies and densities of the two lowest conduction-band bound states in two quantum wells of the thicknesses of 2.0 and 2.3 nm, separated by the spacer layer of the thickness of 3.7 nm: the confinement potential (black line), the energies (red lines), the density of the lower (green line) and upper (blue line) state.

If the dots in the stack were identical, the wave functions would extend over all dots in the stack. However, for different dots the the wave functions tend to localize. As an example we have calculated the two lowest bound states in two quantum wells of the thicknesses of 2.0 and 2.3 nm, separated by the spacer layer of the thickness of 3.7 nm, see Figure 4.7. Both densities are rather well localized in one well, the lower energy in the thicker well and the higher energy in the thinner well, with probabilities of being in the second well below 20 %. The holes are even better localized due to their larger mass. It is therefore reasonable to consider the transitions as originating in a particular dot layer.

4.4 Interpretation of measurements

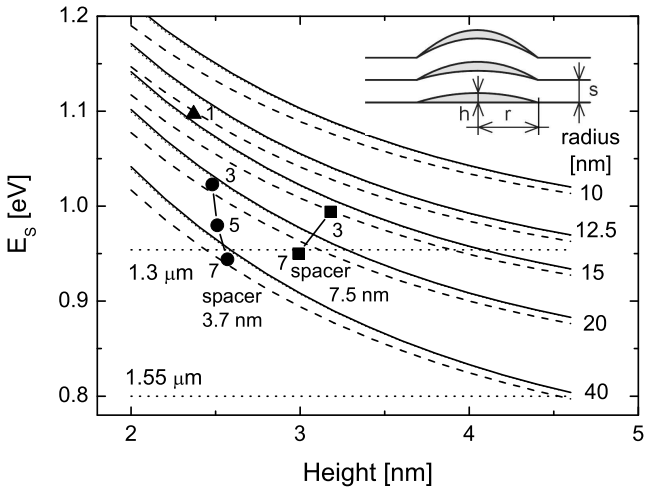

Figure 4.8: The lowest transition energy calculated for the single layer (solid lines) and 7 layer (dashed and dot-dashed lines for the spacer 3.7 and 7.5 nm, respectively) lens-shaped QDs. The symbols show the values resulting from the photoluminescence measurements for the single-layer sample (triangle), 3, 5 and 7 layers samples with the spacer thickness of 3.7 nm (circles), and 3 and 7 layers samples with the spacer thickness of 7.5 nm (squares). The inset shows the model scheme of 3 layers QD structure with geometrical parameters. Reprinted from [4].

The energies of the lowest transitions calculated using the VTWA for the QDs with shape of a lens is shown in Fig. 4.8, as functions of the height for different values of the base radius. The lateral confinement is due to the nearly parabolic potential resulting from the narrowing of the effective quantum well when going off the QD center.

The calculated energy differences ΔE_{sp} for the single QDs are plotted in Fig. 4.9, the values in multilayer systems are almost the same, differing less than by 0.1 meV. Note the weak dependence on the dot height in the whole range (30 – 100 meV) of values observed in our samples. On the other hand, the energy separation decreases fairly steeply with increasing dot radius. Consequently, we assign the observed increase of ΔE_{sp} in samples with thicker

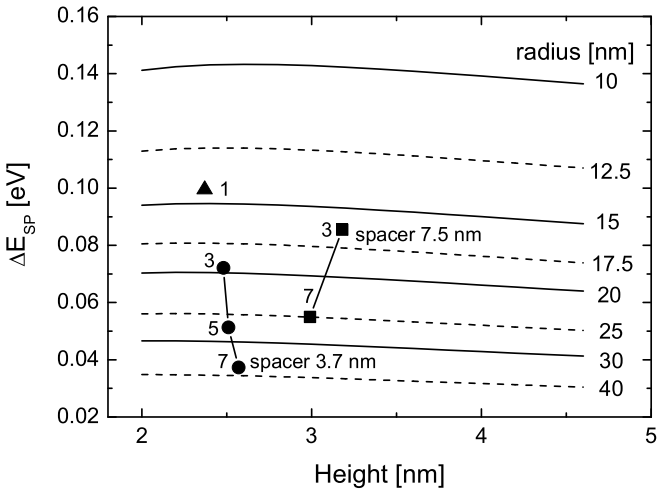

Figure 4.9: Energy difference between the two lowest transitions calculated for the single layer lens-shaped QDs (solid and dashed lines). Corresponding values for 3–7 layer are lower by less than 1 meV. The symbols show the values resulting from the photoluminescence measurements for the single-layer sample (triangle), 3, 5 and 7 layer samples with the spacer thickness of 3.7 nm (circles), and 3 and 7 layer samples with the spacer thickness of 7.5 nm (squares). Reprinted from [4].

spacers (7.5 nm), see Fig. 4.5, to a decrease of the dot radii. We have used the computed dependencies of E_s and ΔE_{sp} on the dot dimensions to estimate the latter for our series of samples.

The dimensions resulting from the comparison of the measurements and calculations are shown in Figs. 4.8 and 4.9 and Table 4.1. The dot heights are limited to a fairly narrow range of 2.3–3.2 nm, while the lateral dimensions increase rather strongly with increasing number of QD layers. The TEM measurements confirm this increase qualitatively, quantitative comparison is not possible since the TEM is sensitive rather to the strain contrast, which tends to extend vertically and squeeze laterally. The height of the hillocks on the top of the capping layer (seen both by TEM and AFM), which is only a bit lower than a product of the single-dot height and the number of layers, supports indirectly our values of the single-dot height and also our assumption that the spacer layer copies the underlying dot profile without flattening it (see Figs. 4.1 and 4.2).

The observed trends can be explained as follows: we suppose that the aspect ratio (height/diameter) of QDs depends rather strongly on the morphology of the underlying GaAs layer. After the formation of the first QD layer, GaAs hillocks formed above the dots influence the progress of QD formation in the next InAs layer. First, the strain in InAs overgrowing the curved surface is lower, which increases the probability of the vertical stacking. Second, the higher the curvature of the surface, the lower the strain, which results in a decrease of the aspect ratio. The curvature of the interfaces depends on the thickness of the GaAs spacer. Thicker spacers should lead to lower curvatures, in agreement with the observed evolution of the aspect ratio and energy separation ΔE_{sp} (see Tab. 4.1). Finally, the largest aspect ratio is expected for QDs grown on a perfectly flat GaAs surface.

No of QD layers	1	3	5	7	3	7
spacer [nm]	–	3.7	3.7	3.7	7.5	7.5
E_s [eV]	1.097	1.023	0.980	0.944	0.994	0.950
ΔE_{sp} [eV]	0.100	0.072	0.051	0.037	0.086	0.055
FWHM [eV]	0.066	0.035	0.037	0.050	0.043	0.035
QD height h [nm]	2.37	2.48	2.51	2.57	3.18	2.99
h_{min} [nm]	2.13	2.33	2.36	2.36	2.92	2.81
h_{max} [nm]	2.65	2.64	2.68	2.80	3.48	3.19
QD radius r [nm]	14.3	19.5	27.2	37.0	16.3	25.0
$r_{min}[nm]$	11.9	17.2	23.0	27.9	14.3	21.5
$r_{max}[nm]$	17.9	22.3	34.4	51.3	18.8	29.8
aspect ratio $h/2r$ $[10^{-3}]$	83	64	46	35	98	60

Table 4.1: Dimensions of the QDs calculated from the energies of the two lowest PL bands and from the full widths at half maximum (FWHM) of the lowest band. The mean values of the height and of the radius (h and r) were determined using the values of the transition energies. The minimum and maximum values (h_{min}, r_{min} and h_{max}, r_{max}) have been estimated from the inhomogeneous broadening in the following way: the QD with the height of h_{min} (h_{max}) and the radius of r has the ground transition energy of E_s + FWHM/2 (E_s − FWHM/2), respectively. The values of r_{min} and r_{max} were determined in a similar way. Reprinted from [4].

4.5 Conclusions

The red shift of the lowest PL bands as high as about 150 meV and the decrease of the energy separation ΔE_{sp}, observed with the number of QD layers increasing from 1 to 7, has been explained by the general trend of increasing QD sizes in the stacks, observed also in the TEM cross sections. The electronic-structure calculations suggest the dominant role of the lateral dimension in forming the energy separation ΔE_{sp}. For the flat dots with a shape of lens, both the height and the base diameter can be estimated from the positions of the two lowest PL bands. In particular, we have observed that lateral dimensions of QDs increase as the number of the QD layers increases. An increase of the spacer thickness leads to an increase of the QD height and a decrease of the base diameter (i.e., the aspect ratio increases) resulting in a higher energy separation ΔE_{sp}. The increase of the height of QDs is pronounced in the systems with thick spacers, the increase of the radius is pronounced in the systems with thin spacers.

Chapter 5

Quantum dots with InGaAs strain reducing layer

Using the modeling of electronic structure, we interpret here the results of the photoluminescence study of a series of single quantum dot layer structures containing $In_xGa_{1-x}As$ strain reducing layers with various In concentration (from 0 % to 29 %), prepared by low pressure metal organic vapor phase epitaxy [20]. These structures display a strong red shift of photoluminescence maxima from 1.25 μm to 1.45 μm at 300 K with increased In content in the ternary layer. The origin of the observed transitions has been explained using magnetophotoluminescence measurements and photoluminescence measurements for various pumping intensities at low temperature. We have calculated optical transition energies using a modification of VTWA. Comparing the calculated and measured energies, we can determine the thickness of the wetting layer and the sizes of the dots. We also explain the red shift in terms of the dot enlargement, the barrier reduction, and the strain relaxation. All the experimental data presented here have been provided by collaborators. The results have been partly published [20].

5.1 Introduction

InAs/GaAs quantum dot (QD) structures exhibit efficient emission of near-infrared light. One way of increasing the emission wavelength towards 1.3/1.55 μm range, important in optical communications, consists in stacking QDs in vertical multilayer structures [101] (see also Chapter 4). Another promising way is the use of ternary and/or quaternary compound heterostructures, such as QDs on metamorphic buffer layers [49], capping of QDs by a strain reducing $In_xGa_{1-x}As$ layers (SRL) [115], or In(Ga)As QDs capped by GaAsSb layers [116]. Here we explain the results of the study of a series of single layer structures with $In_xGa_{1-x}As$ SRL with various In concentration (from 0 % to 29 %), which has revealed a strong red shift of emission wavelengths (from 1.15 μm to 1.32 μm at low temperature; to 1.45 μm at 300 K) with increasing In content in the ternary SRL [20].

5.2 Experimental results

The samples have been provided by the group of E. Hulicius, Institute of Physics of the Academy of Sciences of the Czech Republic (IP, ASCR). The growth conditions of single

layer structures, prepared by low pressure metal organic vapor phase epitaxy (LP MOVPE), were similar to those described in the previous chapter (see p. 78). The capping layer consists of two parts: The $In_xGa_{1-x}As$ SRL of the thickness of 5 nm with In content varying between 0 % and 29 % has been followed by the GaAs capping layer of the thickness of 15 nm. The partial pressures of AsH_3 and TMIn during the InAs QD layer and $In_xGa_{1-x}As$ SRL were identical.

Optical properties were studied at liquid-helium temperature (4 K) by photoluminescence (PL) and magneto-photoluminescence (MPL) in magnetic field parallel to the growth direction up to 23 T. The excitation energy of 2.4 eV has been used, allowing to observe transitions originating in both the InAs wetting layer (WL) and the QDs. The MPL measurements were performed at the Grenoble High Magnetic Field Laboratory by K. Kuldová, the PL measurements at IP, ASCR by J. Oswald.

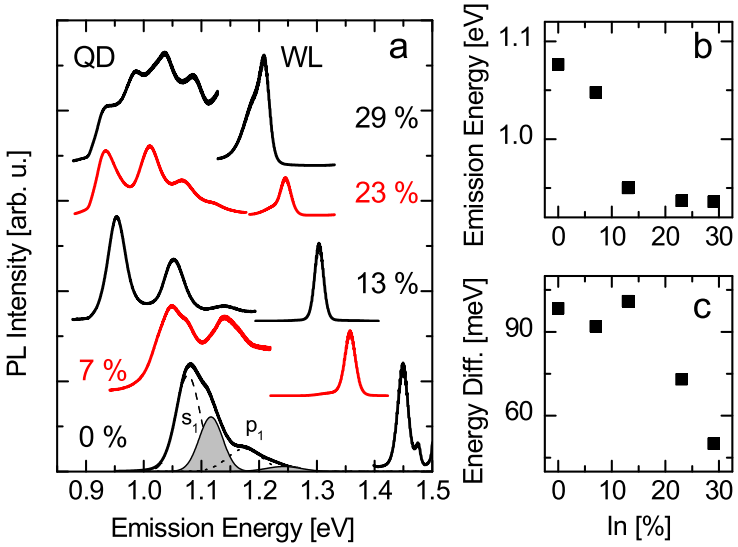

Figure 5.1: (a) PL spectra of samples with various In concentration in SRL. The low-energy bands originate in QD, the high-energy bands in WL. Example of the decomposition into four Gaussian bands (dashed lines and filled area curves) is shown for 0 % In. (b) Positions of the first Gaussian band as a function of the In concentration. (c) Difference between the two lowest Gaussian bands as a function of the In concentration.

PL spectra of the set of samples with various concentration of In in SRL are shown in Figure 5.1. We discuss here the low-energy bands originating in QDs. The most remarkable feature of the series is the shift of the PL signal towards lower energies with increasing In concentration in SRL (180 meV for the ground transition when going from 0 % In to 29 % In). The measured lineshapes are represented fairly well by sums of overlapping Gaussian profiles. The energy of the ground (s) transition and its separation from the next higher (p) band are shown in Fig. 5.1 (b) and (c) as functions of the In concentration in SRL. Doublet structure of s-peaks for 0 % and 7 % is probably due to emission from different types of QDs. PL spectra were measured at various excitation intensities. The low energy bands dominate for low

excitation powers and higher energy transitions intensities increase with increasing excitation powers, which is the evidence for the emission from the excited states of the dots. This interpretation is supported by the MPL spectra (Figure 5.2) where a diamagnetic shift of the ground transition and a splitting of the first excited transition into two peaks occur, the typical behavior expected from the Fock–Darwin model of a single two dimensional particle confined in a parabolic well, see Eq. (4.2) and [111]. It is important for laser applications that the

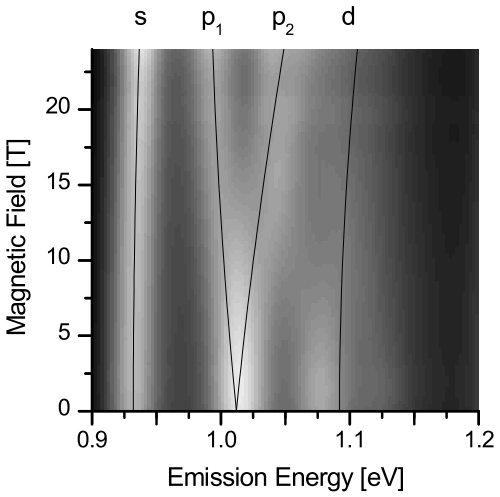

Figure 5.2: Surface plot of MPL spectra of the sample with 23 % In in SRL. Solid lines represent the band positions calculated from the Fock–Darwin model for effective mass $m^* = 0.05\,\mathrm{m}_0$ and harmonic frequency $\hbar\omega = 80\,\mathrm{meV}$ (for the notation see Ref. [18]). Reprinted from [20].

energy difference between PL transitions from the ground and the first excited states remains as high as possible as the In concentration in SRL increases (Fig. 5.1c). The decrease of the energy difference ΔE_{sp} of the ground and first excited transitions is a serious disadvantage for lasing structures since it leads to an undesirable increase of the occupation of higher excited states.

The energy of the emission from the InAs WL, which is about 1.4 eV for 0 % In, decreases to about 1.2 eV for 29 % In (see squares in Figure 5.4). While the observed band is represented rather well by a single Gaussian in the case without SRL (i.e., 0 % of In), it exhibits a low-energy satellite for the systems with SRL; the positions of them are depicted by circles Figure 5.4.

5.3 Interpretation of measurements

The red shift of transition energies caused by SRL can be explained by three mechanisms. First, the band gap of $\mathrm{In}_x\mathrm{Ga}_{1-x}\mathrm{As}$ is lower than that of pure GaAs due to both different chemical composition and the relaxation of the strain. The potential barrier therefore decreases

as the In content in the SRL (i.e., x) increases, resulting in the decrease of the transition energies. Second, the dot is compressed by the capping layer from the sides. The SRL allows, due to its larger lattice constant, for a better relaxation of the strain in the dot than the pure GaAs capping, decreasing the transition energies. This effect is more pronounced for tall dots. Third, the volume of the dots capped with SRL might be larger than of those capped with GaAs. This effect originates also from the lowering of the dot compression by the capping layer. In the following, we identify the proportions of all these effects on the observed red shift, as well as the dimensions of QDs and WL.

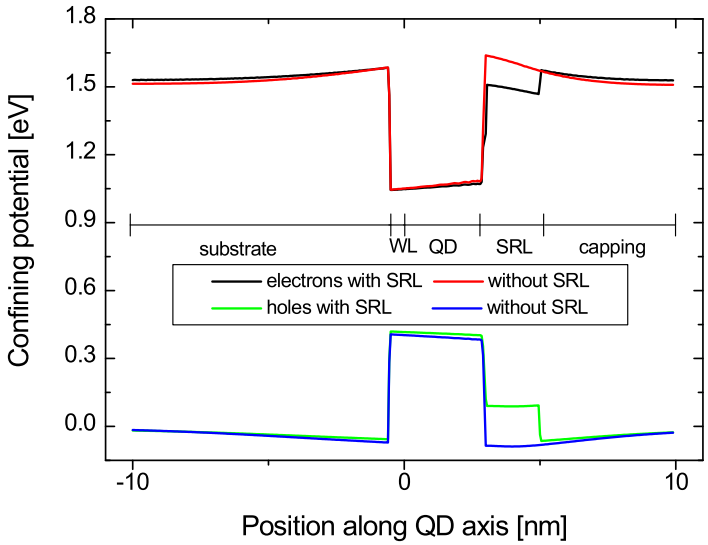

Figure 5.3: Confinement potentials for electrons and holes along the dot axis in the lens-shaped dot with the height of 3 nm and the radius of 15 nm. The dot is either capped by the SRL with the thickness of 5 nm and In content of 29 %, or no SRL is used. The WL thickness is 0.5 nm in both cases and the whole system is embedded in GaAs matrix.

The confinement potentials for the electrons and holes are shown in Figure 5.3 for the lens-shaped dot with the height of 3 nm and the radius of and 15 nm. The potentials have been calculated using Eq. 2.46, where the material parameters of the ternary alloy have been interpolated linearly from the values listed in Table 3.2. A pronounced effect of the SRL is the barrier reduction; it amounts about 0.11 eV for electrons and about 0.17 eV for holes. The presence of SRL also leads to the relaxation of the strain inside the dot, mainly on the boundaries. This influences significantly the growth process; however, the influence on the photoluminescence energies is rather small, not exceeding 10 meV for relevant QD morphologies, which is only a minor part of the observed red shift of 180 meV.

The optical transition energies have been calculated using VTWA (Sec. 3.2) including the energy dependent effective masses. Instead of selecting particular lateral profile, we have used the infinite parabolic potential as the lateral confinement potential, describing fairly the lens- or cone-shaped QDs. We have also calculated the transition energies in the one-dimensional

system formed by the WL and SRL. Comparing the calculated and measured energies, we can determine the thickness of the wetting layer and the sizes of the dots. The errors of the sizes can reach tens of percent; however, the observed trends are plausible.

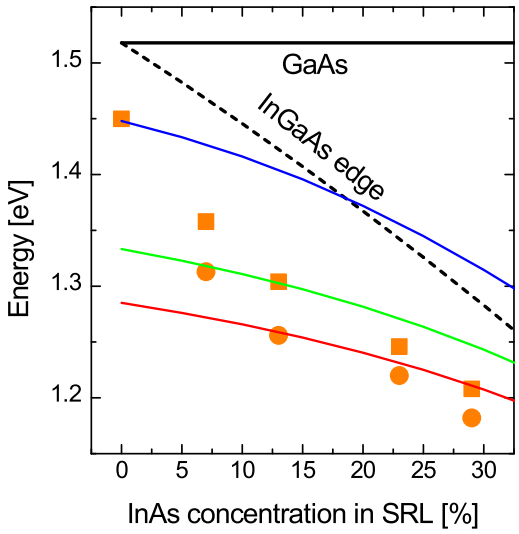

Figure 5.4: The lowest transition energy originating in the system composed of the WL and SRL as a function of the content of In in the SRL. Color lines display the calculated values for the thickness of the SRL of 5 nm and the thickness of the WL of 0.35 nm (blue line), 0.65 nm (green line), and 0.78 nm (red line). The band gap of the GaAs and SRL is depicted by the solid and dashed black line, respectively. The observed transition energies are depicted by squares (Gaussian centers) and circles (low-energy satellites).

The energies of the optical transitions originating in the one-dimensional system composed of the WL and SRL are displayed as squares in Figure 5.4. We have also calculated the transition energies, assuming abrupt boundaries and fitting the WL thicknesses to the observed values of the energies. The WL thickness determined from the model increases as the amount of In in SRL increases. The thickness is 0.35 nm (about 1 ML) for 0 % In in SRL, 0.65 nm for 13 %, and 0.78 nm for 29 %. Two latter values are far above the critical thickness (1.7 ML), for which the pseudomorfic InAs layer is stable on the GaAs substrate. Consequently, they might indicate that the assumption of the abrupt boundaries is not correct and an alloying takes place. However, this conclusion has to be treated with care since the accuracy of the continuum model is limited on the atomistic scale. We have calculated the transition energies for the three WL thicknesses in the whole range of In amount in SRL; the results are displayed by lines in Fig. 5.4. Both the effect of the reduction of potential barrier and that of the increase of QD volume are roughly equally important for the lowering of the transition energies originating in WL. For example, when changing the SRL composition from 0 % to 29 % of In, the observed red shift is 0.24 eV, while the calculated shift for the constant WL

thickness is 0.13 eV only. The remaining part of the shift is caused by the increase of the WL thickness from 0.35 nm to 0.78 nm.

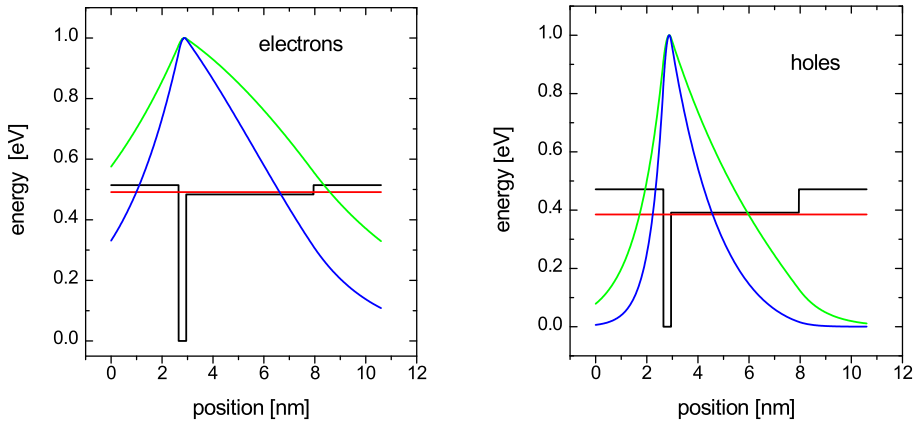

Figure 5.5: The lowest electron (left panel) and hole (right panel) bound state in the system composed of the InAs WL with the thickness of 0.6 nm and the ternary SRL with the thickness of 5 nm and the In rate of 15 %. The confinements potential are depicted by black line, the energies of the bound state by red line. The wave functions and densities are displayed by green and blue lines, respectively.

The transitions under considerations might originate either in WL, or in SRL, or be of mixed type, with the electron extended to the SRL and the hole localized in the WL. However, the classification is rather vague; there is a continuous crossover between the distinct possibilities. As an example, consider a system composed of the InAs WL with the thickness of 0.6 nm and the ternary SRL with the thickness of 5 nm and the In rate of 15 %. The energies and wave functions of the lowest electron and hole state are shown in Figure 5.5. The electron energy is slightly above the band edge of the SRL and its wave function extends to the SRL. On the contrary, the hole energy is slightly below the band edge of the SRL and its wave function is localized in the WL. The observed values of the transition energies are fairly below the band gap of the SRL, which is calculated as the band gap of strained $In_xGa_{1-x}As$ bulk and displayed by thick dashed line in Fig. 5.4. It can be said that the observed transitions originate in the WL and that no transition originating in the SRL has been observed.

The energies of the optical transitions originating in QDs have been calculated fitting the dot dimensions (i.e., height and radius) to the observed values of energies. The resulting dimensions are shown in Figure 5.6 as functions of the In content in SRL. For the low values of In content in SRL (up to 13 %), the QD height increases with the In content, while the radius remains approximately constant. Above this concentration, the QD height starts to decrease slowly, accompanied by the increase of the QD radius and the decrease of the energy separation ΔE_{sp}. It is therefore favorable to keep the In content in SRL about 13 % to obtain this separation as high as possible.

Within our model we have found that ΔE_{sp} depends mainly on the lateral dimensions of the dots (it decreases as the radius of the dot increases, cmp. Fig. 3.29), while the energy of

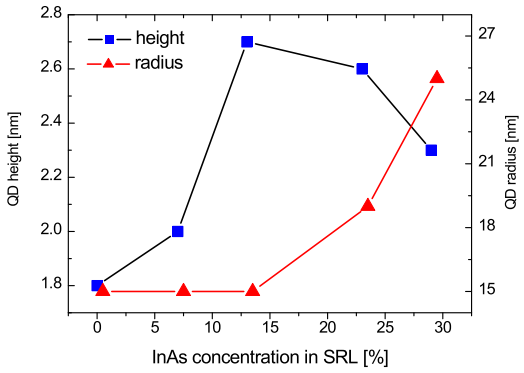

Figure 5.6: The heights and radii of QDs capped by SRL with various In content, as obtained from the comparison of observed transition energies and electronic structure calculations. The lines are guides for the eye.

the ground transition decreases as both dot dimensions, i.e., the height and/or the radius, increase. Thus, the QD structures suitable for the requested applications should have small radius and large height. Both of these conditions are fulfilled for 13 % In content in SRL.

5.4 Conclusions

The properties of the single QD layer structures with $In_xGa_{1-x}As$ strain reducing layer of various In concentrations (from 0 % to 29 %) were explained. A strong shift of the QD emission towards low energy, observed with increasing In content, has been explained by the decrease of the confinement barrier at the SRL side and by the increase of the dot volume. The effect of the strain relaxation in QDs due to the SRL was negligible. The most favorable properties, i.e., high emission wavelength and high energy separation ΔE_{sp}, achieved for 13 % In content in SRL, were attributed to the large height and rather small radius of the dots.

Chapter 6

Magnetooptical properties of quantum dots

As we have demonstrated in previous chapters (4, 5), measurement of optical properties provides a good insight into the electronic structure of quantum dots. An information yield of the optical measurements is largely increased if an external field is applied, either electric or magnetic. The electric field is particularly useful in studies of quantum dot molecules where it is used to couple bright and dark excitons [117, 118]. Some of the effects observed in the electric field are far from being trivial and require an elaborate theory to explain them [119]. Some applications of the magnetic field are discussed below.

The chapter is aimed to magnetooptical properties of quantum dots. A special interest is concentrated to the possibility to retrieve the structural properties of quantum dots, in particular their lateral elongation, vertical profile, aspect ratio, and basis roundness/squareness, from magnetooptical measurements. We also briefly discuss the interplay of external magnetic field, piezoelectric field, and excitonic interaction.

The chapter is divided into two sections. In the first section we describe our experimental data and develop a very simple model in order to interpret them. We demonstrate the sensitivity of the magnetooptical parameters of quantum dots to their lateral elongation, as well as the possibility to retrieve the elongation magnitude from the magnetooptical measurements Comparing our results with the AFM measurements on the samples with and without the capping layer we also gain some insight into the structural modifications during the capping layer growth.

In the second section we apply the elaborate model 8kpTUB (see Section 3.4 for a description) to verify the results of the previous section and to study the dependence between the magnetooptical parameters of the quantum dots and additional structural parameters, such as vertical profile, aspect ratio, and basis roundness/squareness. The effects of the excitonic interaction and the piezoelectricity are studied as well. The second section is purely theoretical since the effects discussed there are too weak to be observed by existent experimental techniques. However, some recent experiments on single quantum dots in magnetic field [120, 121, 122, 123] promise the observation of the effects in the near future.

6.1 Elongation of InAs/GaAs quantum dots from magneto-photoluminescence measurements

We have used magnetophotoluminescence for the determination of the lateral anisotropy of buried quantum dots. While the calculated shifts of the energies of higher radiative transitions in magnetic field are found to be sensitive to the lateral elongation, the shift of the lowest transition is determined mainly by the exciton effective mass. This behavior can be used for a fairly reliable determination both the effective mass and the elongation from spectra containing at least two resolved bands. A comparison of the elongation values with AFM plan-view measurements on the samples and reference uncapped samples yields in an understanding to the structural modification during the capping process. All the experimental data presented here have been provided by collaborators. Some of the results presented in the section have been published [18, 19].

6.1.1 Introduction

Determination of the morphology of quantum dots (QDs) is presently subject of intense interest due to its strong influence on the QD electronic structure [21]. Lateral asymmetry influences the QD optical properties, in particular the polarization of absorption and emission. Moreover, it leads to a decrease of the energy separation between the optical transitions, which leads to worse temperature stability of QD lasers. The QDs suitable for applications are always buried, which embarrasses the determination of their lateral profile by standard structural methods.

Atomic force microscopy (AFM), transmission electron microscopy (TEM), and scanning tunneling microscopy (STM) are usually used to study the shape and size of QDs [124]. Vertical profiles can be measured accurately by high-resolution TEM [125] or cross-section STM [26, 126, 127, 128]. The determination of the lateral profile of buried QDs using STM or AFM plan-view images is much less reliable, since the observed surface profile of the dot structure can differ from the underlying dots [17, 129]. These measurements are sometimes performed on uncapped dots prepared under the same growth conditions [130, 131, 132, 133], assuming tacitly that the dot size and shape remain unchanged during the overgrowing process. However, the latter is not always true as demonstrated, e.g., in [17], where a strong lateral elongation and a decrease of the height after the deposition of the GaAs capping layer were reported. On the other hand, the strong lateral elongation, which is caused by the strong anisotropy of the GaAs diffusion coefficient [134], may concern only the GaAs capping layer, while the underlying dots could be much less elongated.

Magnetophotoluminescence (MPL) has been used in several studies of different properties of QD structures, including the morphology [135, 136, 137], or the impact of the elongation on the exchange interaction [138]. MPL spectra of circular dots, displaying blue shift of the lowest PL band and splittings and crossings of higher bands, were found to be in good agreement with theoretical estimates based on a two–band model of a particle confined in two-dimensional (2D) parabolic potential [139]. We focus here on MPL as a non-destructive tool for the determination of the lateral elongation, discuss its accuracy and limitations, and compare the results with those of AFM.

6.1.2 Theory

The lateral motion of particles in QDs can be approximately treated independently of the vertical confinement, using the 2D harmonic potential in the case of lens-shaped QDs [140]. The reasonability of this approximation is supported by our considerations about VTWA (see Sec. 3.2) and will be verified by a comparison with more elaborate calculations. The Hamiltonian for perpendicular magnetic field reads

$$H = \frac{p^2}{2m^*} + \frac{1}{2}m^*\left(\omega_x^2 x^2 + \omega_y^2 y^2 + \frac{1}{4}\omega_c^2 r^2\right) - \frac{1}{2}\omega_c\, l_z. \tag{6.1}$$

where m^* is the effective mass, $\vec{r}$ is the mass center position, $\vec{p}$ is the momentum, $l_z = xp_y - yp_x$ is the projection of the angular momentum onto the field direction, $\omega_c = eB/m^*$ is the cyclotron frequency; ω_x and ω_y are the harmonic potential frequencies, which are related to the lateral dot dimensions a_x, a_y by $\omega_y : \omega_x = a_x : a_y = L$, where the parameter L quantifies the lateral elongation. Solutions are found using exact diagonalization; for $\omega_x = \omega_y$ they result in the well-known Fock–Darwin states [111, 113, 114].

The transition energies depend on the effective masses and harmonic potential frequencies of both electrons and holes; however, according to our calculations, not all of these parameters appear to be equally significant. In fact, the energies are very precisely (better than to 1 meV) determined by the total harmonic potential frequencies, $\omega_{x/y} = \omega_{x/y}(\text{electron}) + \omega_{x/y}(\text{hole})$, and by the reduced effective mass of the electron–hole pair. We calculate therefore the field-induced energy shifts for a single effective particle, for convenience referred to as exciton below. The exciton energy levels can be compared with the positions of the MPL bands after adding the bulk gap and the vertical confinement energies.

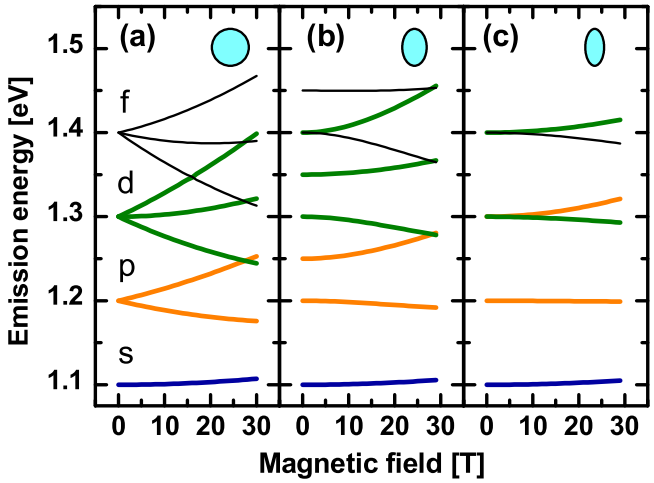

Figure 6.1: MPL energies calculated for a) circular and b), c) elongated QDs. Parameters used in the calculations: $m^* = 0.045\, m_0$, $\omega_x = 100\,\text{meV}$, a) $\omega_y = 100\,\text{meV}$ ($L = 1.0$), b) $\omega_y = 150\,\text{meV}$ ($L = 1.5$), c) $\omega_y = 200\,\text{meV}$ ($L = 2.0$). The energies of the lowest transition at zero field were set to 1.1 eV (corresponding to the vertical confinement energy).

Figure 6.1 displays the magnetic field dependencies of the MPL energies calculated for the circular and elongated QDs. The higher bands of circular dots (see Fig. 6.1a) are degenerate at zero field, splitting rapidly with increasing field. The bands of elongated dots (Fig. 6.1b and c) are not degenerate due to lower symmetry (although accidental degeneracy can still be present, see Fig. 6.1c). The dependences of the transition energies on the field flatten with increasing elongation. The energy levels of circular dots are denoted by s, p, d, f, corresponding to the symmetry at zero field. Zero magnetic moment s-states display only a diamagnetic shift, while the paramagnetic splitting occurs in addition for the higher states.

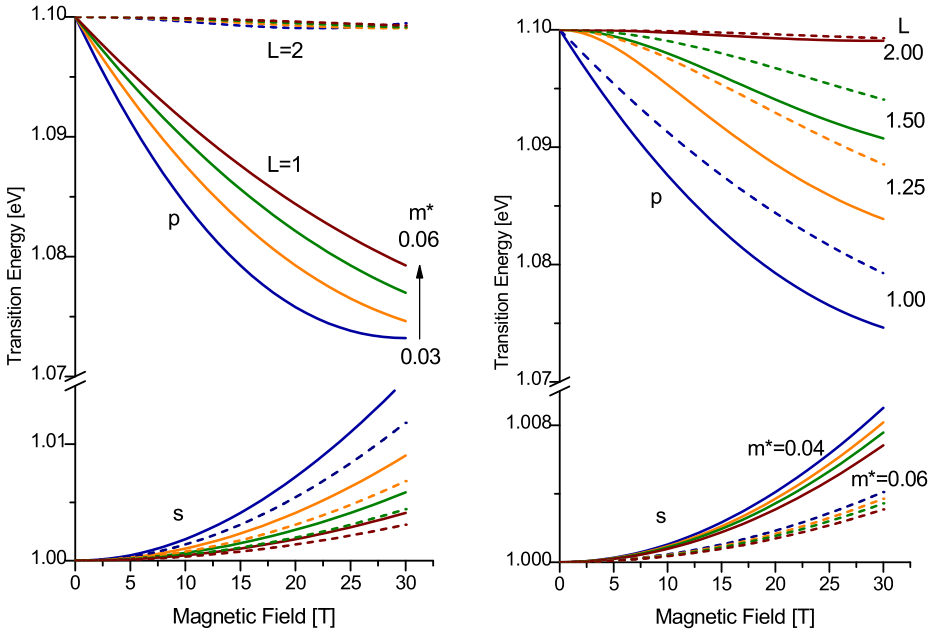

Figure 6.2: MPL energies calculated using the generalized Fock–Darwin model for several values of the parameters m^* and L. The value of $\omega_x = 100\,\text{meV}$ (lower of both harmonic frequencies) is kept for all calculations. Left panel: The values of m^* expressed in m_0 are 0.03 (blue), 0.04 (orange), 0.05 (green), and 0.06 (brown). The value of L is either 1.0 (solid lines) or 2.0 (dashed lines). Right panel: The values of L are 1.00 (blue), 1.25 (orange), 1.50 (green), and 2.00 (brown). The value of m^* expressed in m_0 is either 0.04 (solid lines) or 0.06 (dashed lines).

Figure 6.2 illustrates the impact of the dot elongation L and exciton effective mass m^* to the calculated shifts of the transition energies in the magnetic field. The value of the third parameter, ω_x, is set to 100 meV for all calculations considered here (ω_x is lower of both frequencies and therefore determines the energy separation between two lowest transitions). The left panel shows the energies calculated for several values of the effective mass (0.03, 0,04, 0.05, 0.06; expressed in units of free-electron mass m_0), and two values of the elongation (1.0, 2.0). We observe a pronounced effect of the effective mass value to both s- and p-transition energy shifts for both values of elongation; the higher is the mass, the lower is the energy shift. For circular dot ($L = 1$) the paramagnetic part of the shift is inversely proportional to

m^*. The situation is more complex for the diamagnetic part of the shift. In the low field limit ($\omega_c \ll \omega_x$, where ω_c is the cyclotron frequency) the shift is proportional to B^2 and inversely proportional to a square of m^*. In the high field limit ($\omega_c \gg \omega_x$) the shift is proportional to B and inversely proportional to m^*. We assume that these facts hold also for the elongated dots ($L \neq 1$). If the overall energy shift is low, such as for p-transition of elongated dots (see almost constant dashed lines at about 1.10 eV in the left panel of Fig. 6.2), then the effect of the effective mass is naturally low on the absolute scale, but is still pronounced on the relative scale.

The elongated dots exhibit lower shifts in comparison with circular, i.e., the shifts decrease as the elongation increases. The reasons of such behavior are different for the diamagnetic and paramagnetic part of the energy shift, as well as the magnitudes. In case of the paramagnetic shift the reason for the shift reduction is a break-down of the rotation symmetry accompanied by a decrease of orbital momenta of the electron and holes. The effect is very pronounced. The lowering of the diamagnetic shift can be probably explained as follows: We intend to use our calculations to interpret measurements. For a particular measurement, the parameter ω_x is not free, but determined by the energy separation of two lowest transitions. We therefore keep the value of ω_x while increasing L in our calculations. That means that the dimension of the dot in x-direction is constant and the dimension in y-direction decreases. An extension of an exciton decreases and as a consequence the diamagnetic shift decreases as the elongation increases. The lowering of the diamagnetic shift is therefore indirectly mediated through the volume decrease. We believe that there is only very weak direct influence of the elongation to the diamagnetic shift, i.e., if we preserve the dot volume the modification of the shift due to the elongation will be very low, probably below the observation limit.

The effect of L is therefore strong for the p-transition (very stronger than that of m^*), but rather weak for the s-transition. This is illustrated in the right panel of Fig. 6.2, where the energies calculated for several values of L (1.00, 1.25, 1.50, 2.00), and two values of m^* (0.04, 0.06; expressed in units of free-electron mass m_0) are depicted. As an example, consider the parameter set $L = 1.00$, $m^* = 0.04$ (blue solid lines). The s-transition shift at 30 T is 9.02 meV, the p-transition shift is 25.4 meV. If we increase the effective mass to 0.06, i.e., by 50 % (see green solid lines), the s-transition shift drops to 4.10 meV (45 % of the original value), while the p-transition shift only to 20.7 meV (81 % of the original value). If we, conversely, increase the elongation to 1.50, i.e., by 50 % (see blue dashed lines), the s-transition shift drops only to 7.58 meV (84 % of the original value), while the p-transition shift is heavily reduced to 9.25 meV (36 % of the original value). The p-transition is therefore essential for a precise determination of the elongation.

Figure 6.3 displays the transition energies in the circular dots ($L = 1$) for several values of ω_x (50 meV, 75 meV, 100 meV, 125 meV), and two values of m^* (0.04, 0.06; expressed in units of free-electron mass m_0). The energy shifts can be expressed analytically for the circular dots (4.2). The value of ω_x has no impact on the paramagnetic shift; the diamagnetic shift reads

$$\Delta E_{dia} = C\sqrt{\omega_0^2 + \frac{1}{4}\omega_c^2}, \tag{6.2}$$

where a constant C is equal to 1 for s-transitions, 2 for p-transitions, etc. Similar behavior is observed also for elongated dots. An important fact is that within the Fock–Darwin model the ratio of diamagnetic energy shifts of particular transitions is constant for all values of the magnetic field; this fact is later exploited for a determination of vertical profile of dots.

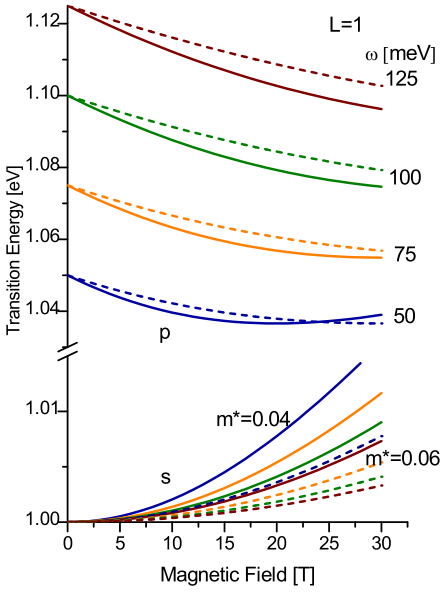

Figure 6.3: MPL energies calculated using the Fock–Darwin model for several values of the parameters ω_x and m^*. The elongation ratio is $L = 1$ for all calculations. The values of ω_x are 50 meV (blue), 75 meV (orange), 100 meV (green), and 125 meV (brown). The value of m^* expressed in m_0 is either 0.04 (solid lines) or 0.06 (dashed lines).

Some additional issues have been discussed in [141]. We have calculated the errors of the parameters estimates assuming that ω_x is known precisely (it can be determined with a fairly small error from the energy separation of the two lowest transition) and the transition energies are determined for magnetic field from 0 T to 30 T with the step of 3 T with a random error of magnitude of 1 meV (2 meV) for the lowest (first higher) transition, respectively. For reasonable values of m^* (from $0.03\,m_0$ to $0.06\,m_0$) and L (from 1 to 2), the maximum relative errors of the m^* and L are 11 % and 5 % for $\omega_x = 100$ meV, and 3 % and 4 % for $\omega_x = 20$ meV. Obviously, the largest relative errors are found for the parameter values with the most flat energy dependencies; i.e., $m^* = 0.06\,m_0$ and $L = 2$. For these values, the correlation of the estimates is 1 % (-28 %) for ω_0 of 20 meV (100 meV), respectively. Such a small correlation is crucial for the accurate determination of the parameters.

Of course, there are additional systematic errors, resulting from the model inaccuracy. Some of them are discussed later on in the next section.

Sometimes it is not possible to detect the higher transitions. In such cases, it is still possible to obtain ω_x and m^* for the circular dots [137]. However, if the dots are elongated, then even if ω_x was known, the values of L and m^* could not be determined simultaneously due to their large correlation, which can easily exceed 99 %. The relative errors of the parameter estimates are then several tens of percents, or even more. This is illustrated in Fig. 6.4, where the field dependence for selected values of the parameters is reproduced using different sets of the parameters ω_0, m^*, L. Lines differing in ω_x and m^* are distinguishable on the scale of meV and therefore simultaneous determination of both parameters is possible; on the other hand, the opposite is true for the lines differing in m^* and L.

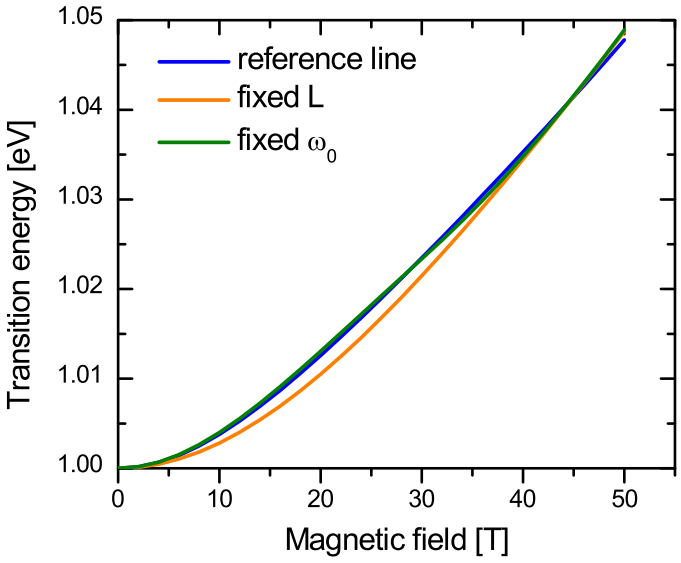

Figure 6.4: The transition energies calculated for the following values of the parameters: $\omega_x = 20\,\mathrm{meV}$, $m^* = 0.045\,m_0$, $L = 1$ (blue line); $\omega_x = 50\,\mathrm{meV}$, $m^* = 0.034\,m_0$, $L = 1$ (fixed L; orange line); $\omega_x = 20\,\mathrm{meV}$, $m^* = 0.040\,m_0$, $L = 1.5$ (fixed ω_x; green line).

6.1.3 Experiment

To compare the theoretical expectation with experimental results, several single layer InAs/-GaAs QD structures were prepared by low pressure MOVPE technique in an AIXTRON 200 machine using Stranski–Krastanow growth mode [105]. Semi-insulating GaAs (100) wafers were used as a substrate. Precursors used for the growth of GaAs and InAs layers were TMGa, TMIn and AsH_3. Prior to the growth, the substrate temperature was held on 800 °C for 5 minutes under AsH_3 flow. The total pressure of 70 hPa and total flow rate of 8 slpm was kept during the growth. The first GaAs buffer layer was grown at 650 °C. Subsequently, the temperature was decreased to 500 °C for the growth of the rest of the structure, consisting of the second GaAs buffer layer, the InAs QD layer and the GaAs capping layer of a thickness of 22 nm. We studied two samples, labelled I and II, which differ in the growth conditions of the InAs QD layer. In particular, the V/III ratio of 182 (85, a lower AsH_3 partial pressure) and the growth time of 15 (9) seconds has been used for sample I (II), respectively. The partial pressure of TMIn 7.10^{-2} Pa, and the growth interruption of 30 s after the InAs layer growth (required to complete QDs formation) were identical for both samples. A reference sample to sample II, referred to as sample IIref, was prepared at the identical growth conditions, but without a capping layer. The reference sample is intended for AFM measurements. The samples have been provided by by the group of E. Hulicius, Institute of Physics of the Academy of Sciences of the Czech Republic (IP, ASCR).

Optical properties of QDs have been studied by photoluminescence (PL) at IP, ASCR and by magneto-photoluminescence (MPL) at Grenoble High Magnetic Field Laboratory. Ar laser (pumping photon energy of 2.41 eV) was used for the excitation. Optical 200 μm core

multi-mode fibres were used for both the luminescence excitation and collection. Maximal excitation density on the samples was 500 W/cm^{-2}. The emitted light was analyzed by a 600 grooves/mm single grating monochromator with a resolution of 1 meV, and detected by an InGaAs photomultiplier using standard lock-in technique. The MPL measurements were performed in a magnetic field parallel to the growth direction (Faraday configuration) in the range up to 26 T in a resistive magnet. All spectra reported here were taken with the samples immersed in liquid nitrogen.

Atomic force microscopy (AFM) images were obtained on a Veeco Autoprobe CP scanning probe microscope with the maximum scanning area of 5 μm, in the contact mode, using the ULCT–AUHW ultralevers (tip radius of 10 nm).

6.1.4 Results and discussion

AFM plan view scans of the samples I, II, and IIref are displayed in the left panel of Figures 6.5, 6.6, and 6.7, respectively. The linear size of the pictures is 5 μm for sample I and 2 μm for the samples II, IIref. The surface plane has an orientation (001). The orientation of the edges is not the same for all Figures; light blue lines denote the directions [110] and [1$\bar{1}$0], whereas the [110] direction is horizontal in Figure 6.5, goes from the left upper corner to the right bottom corner in the Figure 6.6, and is vertical in Figure 6.7. The right panel of the Figures display a surface profile along two perpendicular lines with orientations [110] and [1$\bar{1}$0], intersecting on the top of a quantum dot. The position of the profiles in the plan view scans is denoted by the blue light segments.

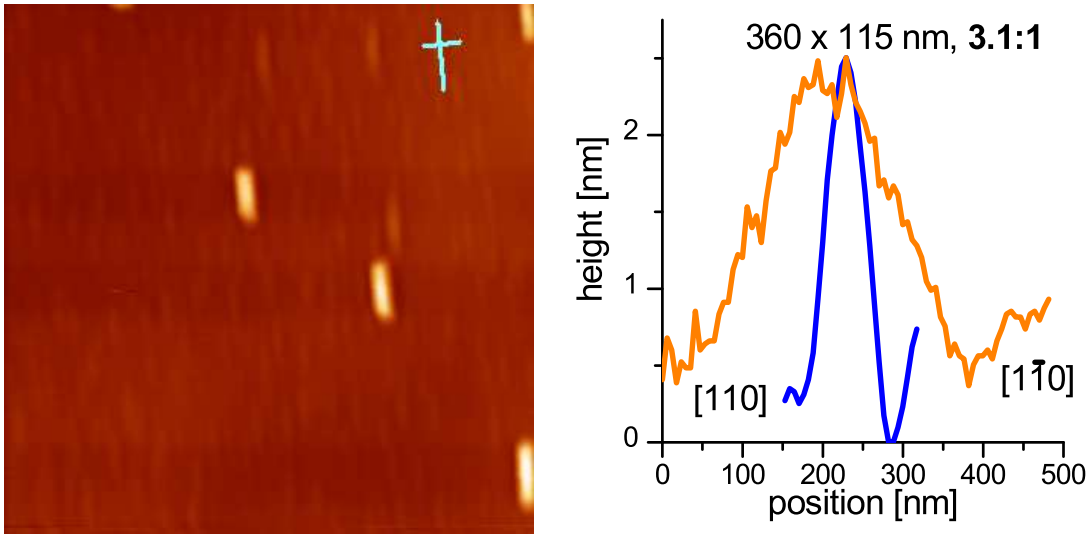

Figure 6.5: Surface of sample I (with a capping layer) displayed by AFM: 5 μm × 5 μm plan view (left panel); height profile of a quantum dot (see light blue segments in the left panel) along the directions [110] and [1$\bar{1}$0] (right panel).

Let us first concentrate to the planar scans. Two or three types of the hillocks are found on the surface of the samples I and II. The lateral dimensions of all types of hillocks is

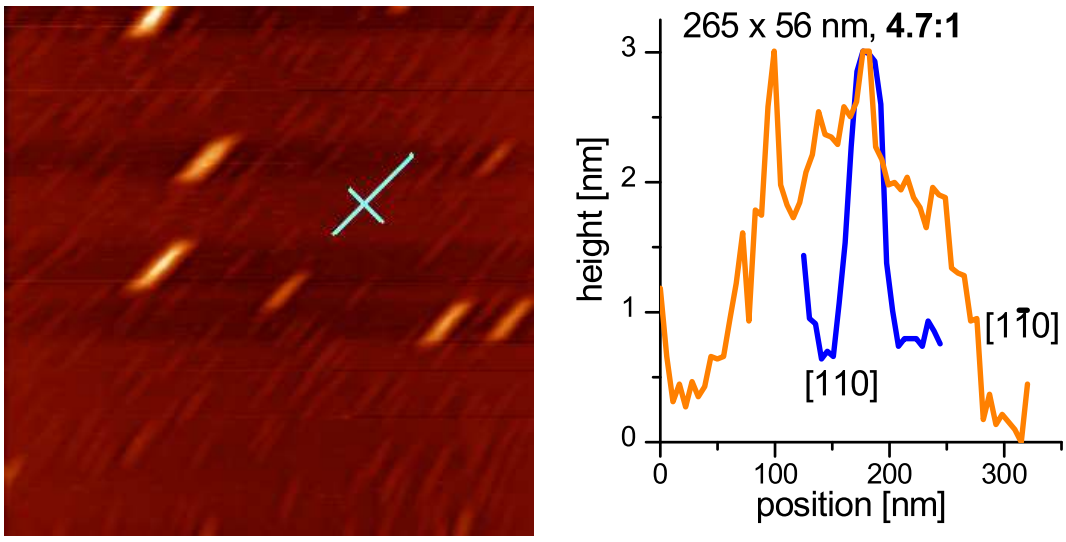

Figure 6.6: Surface of sample II (with a capping layer) displayed by AFM: $2\,\mu\text{m} \times 2\,\mu\text{m}$ plan view (left panel); height profile of a quantum dot (see light blue segments in the left panel) along the directions [110] and [1$\bar{1}$0] (right panel).

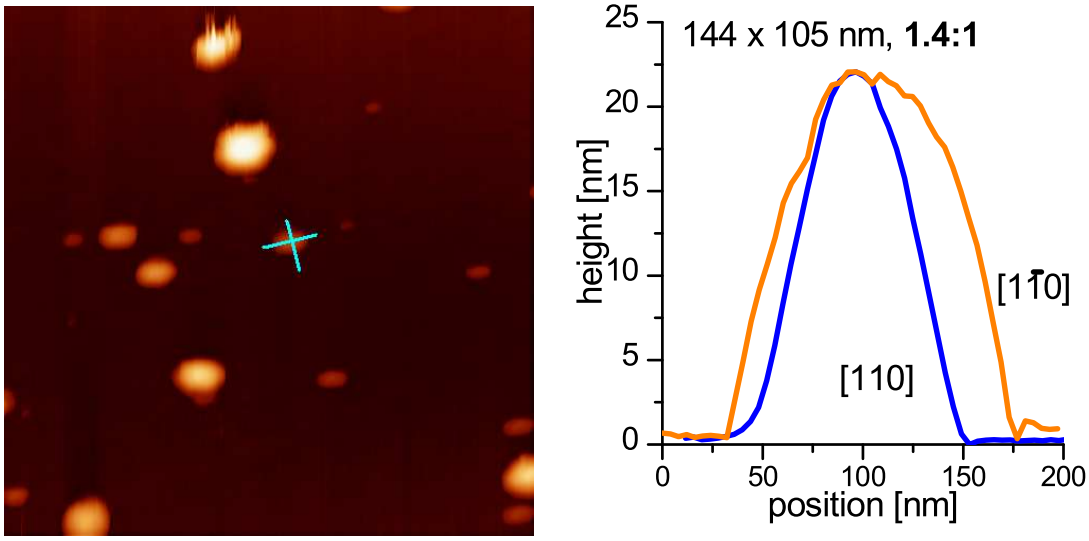

Figure 6.7: Surface of sample IIref (without a capping layer) displayed by AFM: $2\,\mu\text{m} \times 2\,\mu\text{m}$ plan view (left panel); height profile of a quantum dot (see light blue segments in the left panel) along the directions [110] and [1$\bar{1}$0] (right panel).

comparable, but they differ significantly in height. The first-type hillocks are rather low, with a typical height of 2 nm (the underlying dot can be naturally higher). Their density is several tens per square micrometer. The second-type hillocks are very high, exceeding 10 nm. Their density is more than ten times lower than for the first-type hillocks and does not exceed units per square micrometer. We are quite sure that the quantum dots are hidden below the first-type hillocks. First, the second-type hillocks are so large that dislocations are formed in their volume in order to decrease the strain field. The non-radiative recombination due to the dislocation consequently inhibits the luminescence. Second, if there were dots only below the second-type hillocks, it would be probably possible to observe single dot features in the microphotoluminescence experiment with an excitation spot of a diameter of 5 μm; however, our experimental evidence is different.

The surface of the uncapped sample IIref contains a variety of hillocks ranging from very small to rather large. It is not easy to identify those which form the (optically active) quantum dots after the capping layer is grown. A detailed AFM study [17] reveals that the minor lateral dot dimension is preserved or slightly decreased during the capping procedure, we therefore attribute the medium sized hillocks on the sample IIref to the quantum dots in sample II. Here some caution has to be paid to the fact that our growth method and conditions differ from those used in [17]. It is notable that the density of the hillocks (either medium sized or all) is much lower in comparison with the dot density observed at the capped sample II. This feature is not yet understood; we suggest here two explanations. First, the dot distribution is not homogeneous over the whole sample. The measurement of sample IIref could be incidentally carried out in the area with low dot density, which has to be verified by additional measurements in another parts of the sample. Second, it is possible that the large structures observed on the top of sample IIref dissolve during the capping process

We proceed with the discussion of the dot dimensions. Single hillock was taken as a representative for each sample. The variation of the dimensions for the hillocks of the same type was up to 20 % (although the same type of the hillock is not well defined for sample IIref). The sample I hillock has a height of 2.5 nm, lateral dimensions (diameters) of 115 nm and 360 nm, the lateral elongation has a value of 3.1. The sample II hillock has a height of about 3 nm, lateral dimensions of 56 nm and 265 nm, the lateral elongation has a value of 4.7. The sample IIref hillock has a height of 22 nm, lateral dimensions (diameters) of 105 nm and 144 nm, the lateral elongation has a value of 1.4. In summary, the hillocks on the surface of uncapped samples are tall and rather circular; the capping layer growth is accompanied by a large decrease of the height (to approximately one tenth of original value) and an increase of the elongation ratio. Both facts are in agreement with the observations in [17]. The decrease of the height applies very probably also to the underlying quantum dots. The thickness of the capping layer, 22 nm, is comparable to the original height of uncapped hillocks; if the height was preserved after the capping, we would expect taller hillocks than of 2 – 3 nanometers. The lateral elongation of the capped quantum dots cannot be determined from AFM measurements.

In the end of the discussion of AFM measurements we add the following note: it would be benefitable to have the reference sample without the capping layer also for sample I. The reason for non-existence of such sample is that sample I was grown several years before our study. Many properties of the growth process have changed since then, either due to replacement of the machine parts or due to its ageing. It is therefore not possible to prepare the reference sample at identical growth conditions. Despite it sample I is included in our

study due to its magnetoluminescence properties, which differ significantly from those of recently grown samples.

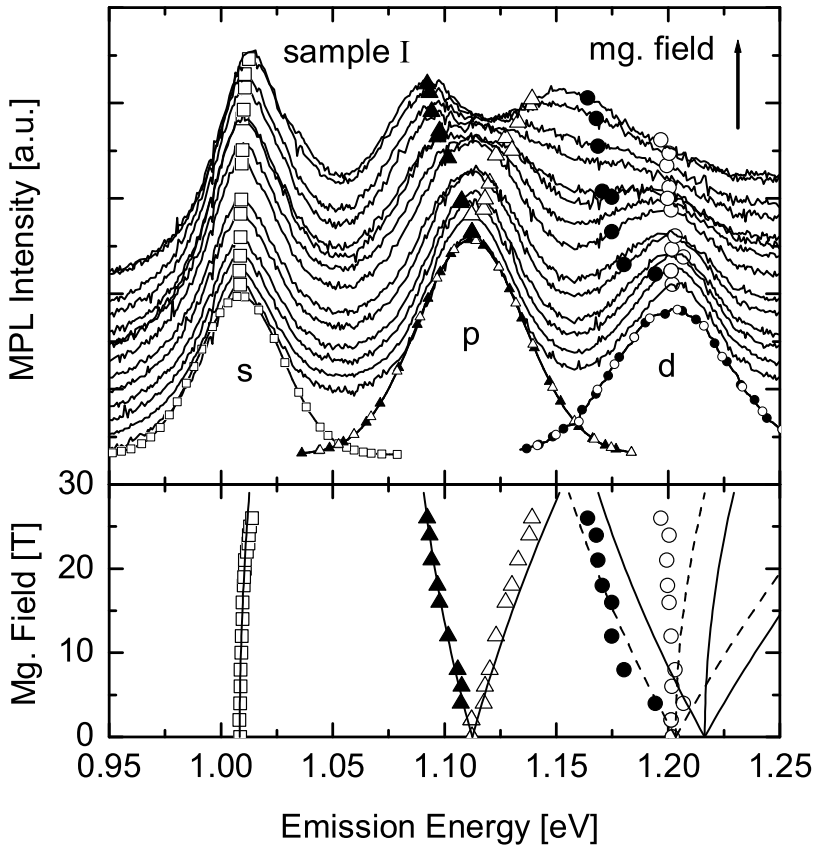

Figure 6.8: Top panel: Magnetophotoluminescence spectra (for the magnetic field from 0 to 26 T) of sample I. The graphs of individual spectra are shifted vertically. The zero-field spectrum is decomposed into three Gaussian bands, labelled s, p, and d. The positions of the band maxima are displayed by open squares (s-band), full and open triangles (lower and upper component of the p-band) and full and open circles (lower and middle component of the d-band). Bottom panel: The symbols depict the band positions obtained by the Gaussian decomposition of the spectra; the same notation as in the upper panel is used. The best fit of the data with the Fock–Darwin model is displayed by solid lines. Dashed lines display the d-band energies shifted by 13 meV to the lower energy (the shift corresponds to the non-parabolicity of the effective lateral confinement potential). Reprinted from [18].

Photoluminescence spectra measured in the magnetic field are displayed in the top panels of Figures 6.8 and 6.9 for the samples I and II, respectively. The shape of the PL bands, broadened by the size and shape fluctuations of QDs, is approximately Gaussian. The central

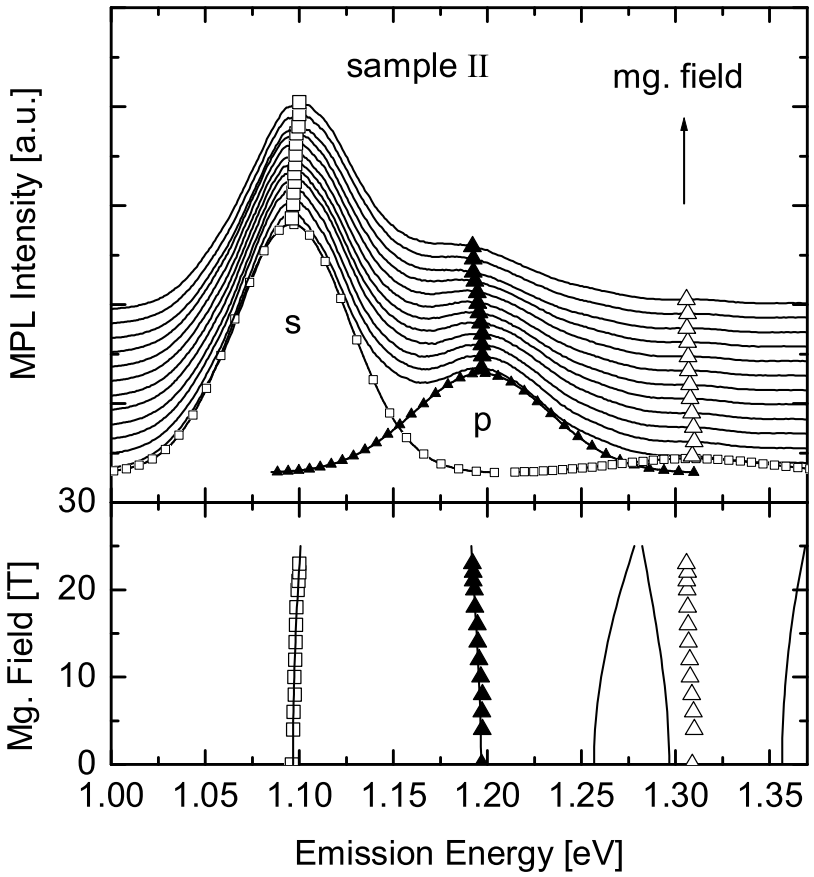

Figure 6.9: Top panel: Magnetophotoluminescence spectra (for the magnetic field from 0 to 23 T) of sample II. The graphs of individual spectra are shifted vertically. The zero-field spectrum is decomposed into three Gaussian bands, first two of them labelled s, p. The positions of the band maxima are displayed by open squares (s-band), solid triangles (p-band) and open triangles (low-amplitude band, whose origin is not clear). Bottom panel: The symbols depict the band positions obtained by the Gaussian decomposition of the spectra; the same notation as in the upper panel is used. The best fit of the data with the generalized Fock–Darwin model (including the lateral elongation of dots) is displayed by solid lines. Reprinted from [18].

energies of the bands, obtained by a Gaussian decomposition of the measure spectra, are displayed by symbols in the bottom panels of Figures 6.8, 6.9 as functions of applied magnetic field. The decomposition of the spectra into elementary bands was performed as follows: the width of each zero-field Gaussian band has been fixed, the central energy and the band amplitude were adjustable parameters. Possible double (triple) degeneracy of the second (third) band, applicable if the dots exhibit a circular symmetry, has been taken in account. Five Gaussian bands can be resolved in the spectra of sample I, while only three in the spectra of sample II. The third band of sample II has rather low amplitude even at maximum excitation power density, and is partially overlapped with a PL band between 1.32 eV and 1.38 eV, whose origin is yet unknown.

The lowest PL bands of both samples (with the zero-field energy 1.01 eV for sample I and 1.09 eV for sample II) display a similar diamagnetic shift in the magnetic field whereas the higher PL bands of both samples behave differently. The second band of sample I (1.11 eV) splits into two clearly resolved bands, and the splitting of the third band (1.20 eV) is also apparent. By contrast, the second band of sample II shows rather weak red shift in the magnetic field (4 meV at B = 23 T), no splitting is observed.

The energy-field dependencies observed for sample I have been commonly reported, especially for small dots with the lowest PL band at about 1.3 eV [112, 142]. Such dependencies are rather well described by a simple two-dimensional Fock–Darwin model; more elaborate calculations do not differ significantly from the Fock–Darwin patterns ([143], also Sec. 6.2 in this work). Quantum dots are assumed to have a rotation axis parallel with the magnetic field. Due to this symmetry, some excited levels are double degenerate. Further degeneracy comes out of the particular shape of the dot. For example, the d-shell is composed of a doublet (two degenerate levels with opposite orbital magnetic momentum) and a singlet (one level with zero orbital magnetic momentum). All these levels are degenerate in the Fock–Darwin model due to the harmonic confinement potential, forming d-shell triplet. For a generalized quantum dot with different lateral confinement (but still with a rotation axis) the triplet is splitted into the doublet and singlet. However, the energy separation between the doublet and the singlet is usually rather low and beyond the resolution limit of standard PL measurements on the dot ensembles; treating the d-shell as a triplet is therefore reasonable. The pronounced splitting of the higher PL bands is explained by the paramagnetic interaction of the orbital magnetic momenta with the applied magnetic field.

We have fitted the experimental data with the Fock–Darwin model (defined by Eq. 6.1 with $L = 1$). The parameter ω_x was determined from the energy separation between two lowest PL bands; it reads 104 meV. The value of the effective mass m^*, determined from the magnetic field dependencies, is $0.055\, m_0$. The s-, p- and d-transition energies calculated using these parameters are displayed by the solid lines in the bottom panel of Fig. 6.8, the experimental energies are denoted by the symbols. Note a very good agreement of the experiment and theory for the higher p-transition. The experimental d-transition energies are located 13 meV below the energies expected from the Fock–Darwin model. This discrepancy can be explained by the non-parabolicity of the lateral confinement, since a rigid shift by 13 meV (displayed by dashed lines in Fig. 6.8) provides a good agreement with the experimental data.

Contrary to the case of sample I, the energy-field dependencies measured on the sample II have not been observed before our study. The degeneracy of higher bands is not present which means that the rotational symmetry is broken. We try here to explain observed dependencies by a lateral elongation of quantum dots.

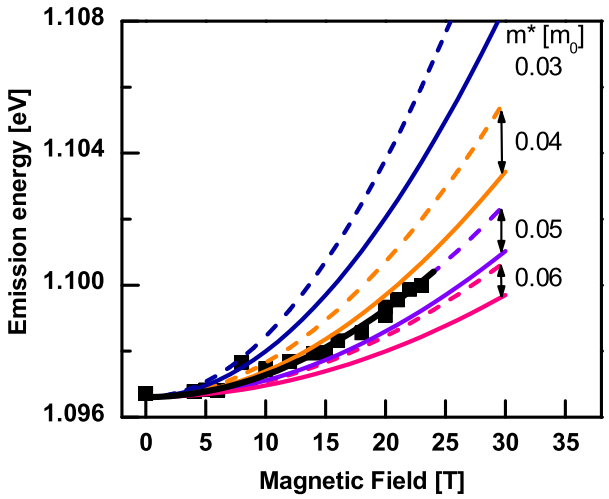

Figure 6.10: Energy of the lowest MPL transition against magnetic field for elongated QDs. The experimental values (squares) and calculated energies with parameters $\omega_x = 100\,\text{meV}$, ω_y going from 100 meV (dashed lines) to 200 meV (solid lines), and effective masses $0.03\,m_0$ (blue), $0.04\,m_0$ (orange), $0.05\,m_0$ (violet), $0.06\,m_0$ (pink), indicated by the arrows. The best agreement with the experimental data has been obtained for $\omega_y = 160\,\text{meV}$ and $m^* = 0.045\,m_0$ (black solid line).

The transition energies, obtained from the Gaussian decomposition of the measured MPL spectra (see Fig. 6.9) are shown in Figures 6.10 and 6.11. The values of the model parameters, ω_x, ω_y, m^*, have been obtained as follows: ω_x (the lower of both frequencies) was fixed at the value of the splitting between the lowest and the first higher MPL transition at zero field (x is the direction of elongation), ω_y, m^* were obtained by fitting the observed magnetic field dependencies. The measured and calculated values of the lowest (s) MPL transition are shown in Fig. 6.10. The shape of the theoretical dependences is influenced primarily by the exciton effective mass, with the best fit occurring for $0.045-0.050\,m_0$.

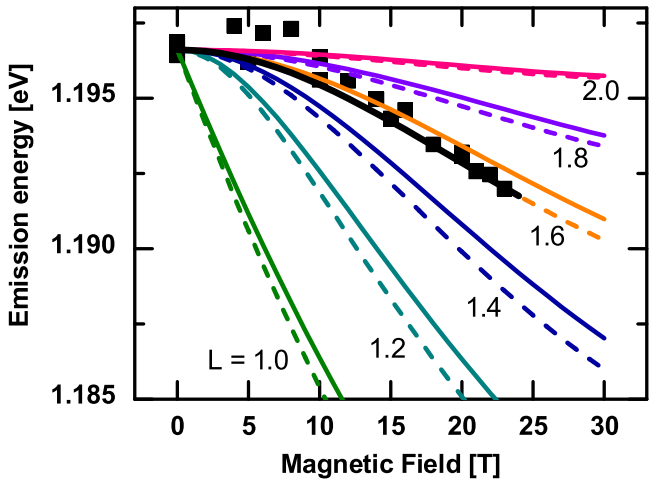

Figure 6.11: Energy of the first higher MPL transition against magnetic field for elongated QDs. The experimental values (squares) and calculated energies with parameters $\omega_x = 100\,\text{meV}$, m^* going from $0.045\,m_0$ (dashed lines) to $0.05\,m_0$ (solid lines), and ω_y values of 100 meV (green), 120 meV (cyan), 140 meV (blue), 160 meV (orange), 180 meV (violet), 200 meV (pink). The best agreement with the experimental data has been obtained for $\omega_y = 160\,\text{meV}$ and $m^* = 0.045\,m_0$ (thick solid line).

Figure 6.11 displays the measured and calculated energies of the first higher (p) MPL transition. The influence of the lateral elongation is obviously stronger than for the s–transition, allowing us to determine the elongation accurately. The best agreement between the measured and the calculated energies has been obtained by taking $m^* = 0.045\,m_0$ and $\omega_y = 160\,\text{meV}$ (see the thick lines in Figs. 6.10 and 6.11). The ratio of the harmonic potential frequencies corresponds to the lateral elongation $L = 1.6$.

The uncertainty of resulting parameters consists of a systematic part, and of a random part resulting from the errors of energy positions. The former is mainly due to limited accuracy of the model (the non-parabolicity of the actual potential and the non–separable lateral and vertical confinement). We have performed exact 3D diagonalizations for several QD dimensions and shapes (lens, cone, cylinder) resulting in slightly lower energy shifts compared with the approximate 2D calculations, which therefore tend to overestimate the exciton mass (see also Fig. 6.23). The maximum difference in the shifts is about 10 % for

the lens shape and 20 % for other shapes, even for the height/diameter ratio as high as 0.4. Note that Wojs et al. [140] report negligible difference between the two models in the case of circular lens-shaped dots. Another part of systematic error comes from the fitting procedure; however, it influences only the absolute values of energy, keeping the differences almost unchanged. We estimate the overall systematic errors of the energy shifts to be below 10 % for flat dots. The random error of the MPL band positions is less than 1 meV; adding the related uncertainties, the errors of effective mass and elongation are limited by $0.005\,m_0$ and 0.1, respectively, for the dots investigated here. Consequently, the data of Figs. 6.10 and 6.11 provide the elongation within the range 1.5 – 1.7, and the effective mass in the range $0.04\,m_0$ – $0.05\,m_0$. The effective mass value resulting from the k.p approximation is $0.035\,m_0$. Since the magnitude of the diamagnetic shift is approximately proportional to the mean exciton dimensions squared, and inversely proportional to its mass [144, 145], the tendency to higher values obtained from the fitting is probably due to an additional decrease of the exciton lateral dimensions not included in our model. It should be noted that the parameters m^* and L are strongly correlated when estimated simultaneously using only the lowest transition (see also Fig. 6.4); the pumping power in the MPL measurement has to be high enough to provide at least two resolved bands.

In the end we drop a line about the modification of the lateral elongation during the capping process. We have three values of L for sample II: 1.6 (from magnetophotoluminescence), 4.7 (from AFM), 1.4 (from AFM on the reference uncapped sample). For sample I the third value is missing, the first two are 1.0 (from magnetophotoluminescence) and 3.1 (from AFM). It is evident from here that the strong lateral elongation observed on the surface of capped samples concerns only the GaAs capping layer, while the underlying dots are much less (if at all) elongated. The first and third value (i.e., obtained from magnetophotoluminescence and from AFM on the reference uncapped sample) are comparable for sample II, which indicates that the lateral elongation is not very influenced by the growth of the capping layer.

6.1.5 Conclusions

In conclusion, we find MPL capable to reveal the lateral elongation of buried quantum dots. Fitting our model to the experimental data taken on a single layer InAs/GaAs QD sample, we found the following values: For sample I, the elongation of the dots equal to 1 and the exciton effective mass equal to $0.055\,m_0$. For sample II, the elongation of the dots in the range 1.5 – 1.7 and the exciton effective mass in the range $0.04\,m_0 - 0.05\,m_0$. The comparison with the AFM results indicates the absence of a pronounced increase of the lateral elongation during the overgrowth. The exciton effective masses are slightly higher than those calculated from the eight-band k.p approximation for strained QD (falling to the $0.03\,m_0 - 0.04\,m_0$ range). This indicates possible deviations of the actual QDs from the assumed shapes, pronounced effect of the excitonic interaction, or oversimplified model of the electronic structure.

6.2 Interrelation of structural and magnetooptical properties of InAs/GaAs quantum dots

Until now, magnetophotoluminescence has been used in many studies of different properties of QD structures, including the morphology [19, 137], or the impact of the lateral elongation of the dot basis on the exchange interaction [138]. For understanding these effects, a detailed

theory describing the electronic levels is necessary. We present here a systematic theoretical study of InAs/GaAs dots in magnetic fields for different dot shapes, we discuss particularly the effect of lateral elongation, roundness/squareness, vertical profile, and aspect ratio on the magnetooptical properties. Moreover, we discuss the possibility to retrieve the structural parameters from magnetooptical measurements.

Our calculations of single particle states have been carried out using eight-band k.p theory [73, 80], including the influence of strain and first- and second-order piezoelectricity [55, 86]. Magnetic field is introduced through Peierl's substitution in the wave-vector and by adding the Zeeman energy term [61]. The exciton energies are calculated using the configuration interaction (CI) method, expanding the wave function into the basis of Slater determinants constructed from single-particle states. Accuracy of the results is limited mainly by neglecting distant bands in the $\vec{k}\cdot\vec{p}$ theory; we estimate the error to be up to 5 % for both absolute energies and energy shifts. The method is referred to as 8kpTUB method throughout this work; it has been discussed briefly in Sec. 3.4. Aside from the calculations of the magnetooptical properties of various quantum dot systems, we also use the 8kpTUB method to verify the predictions of less elaborate methods (in particular, the generalized Fock–Darwin model, Sec. 6.1) and to estimate their accuracy. Some of the results presented in this section have already been published [146, 147].

A general note concerning all the comparisons described in this section has to be added: There are many parameters influencing the resulting electronic structure of a particular quantum dot. If we want to extract the effect of a single parameter, we have to ensure that the influence of the remaining parameters is as small as possible. This is not a simple task, since the parameters are often interrelated and an uncontrolled modification of one parameter may emerge as a side-effect of a controlled variation of another parameter. As an example, let us consider an investigation of the effect of the dot vertical profile on the transition energies. We can, for instance, calculate the transition energies for a cone-shaped and cylinder-shaped dot. Naively, we could set identical heights and radii of both dots, finding that the transition energies in the cylinder are significantly lower than those in the cone. The problem apparently is that the difference in the transition energies is caused by the different volumes of both dots, and not by the vertical profile. We should therefore preserve the volume (and as much of other parameters influencing the transition energies as possible) in order to elucidate the direct effect of the vertical profile. In our comparative studies of magnetooptical properties we prefer to conserve the transition energies for each quantum dot involved in a particular comparison, guided by the following reasons. First, we need to conserve the parameters which are not the subject of interest. There are numerous in elaborate models; however, just two of them enter the Fock–Darwin model [113, 114] (see also Eq. 4.1 in this thesis): the harmonic frequency and the effective mass. The harmonic frequency is proportional to the energy separation between the two lowest transitions. The effective mass depends on particle energies (2.14). The conservation of both electron and hole energies cannot be achieved in general; however, the conservation of transition energies is a good substitution for it, being therefore the plausible approximation of the conservation of all subsidiary parameters. Second, we intend to use our calculations for the retrieval of structural parameters of the quantum dots from their magnetooptical properties. We therefore assume several model quantum dots, whose transition energies correspond to the measured values in zero field, compare the predicted shifts of transition energies in magnetic field with experiment, and select the model dot with the best agreement as the representative of the real quantum dot. The conservation of the transition energies is naturally essential here.

A finding of the dot dimensions for which the transition energies in dots of various morphologies are identical is a very demanding task for elaborate models, in particular 8kpTUB. In such cases we replace the conservation of the transition energies by the conservation of the volume. It often approximates the conservation of the transition energies very well. However, the results of such comparison always need to be treated cautiously.

6.2.1 Magnetooptical properties in general

As an example, we discuss here magnetooptical properties of the QD of lens shape with the height of 3 nm and the diameter of 20 nm. The evolution of the electron levels in magnetic

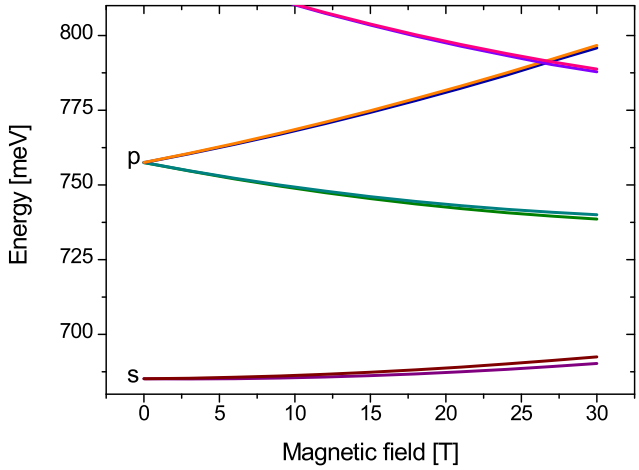

Figure 6.12: The electron energies in the lens-shaped quantum dot with the height of 3 nm and the diameter of 20 nm in magnetic field.

field is displayed in Figure 6.12, it follows the Fock–Darwin (FD) pattern: the diamagnetic shift of all states and the paramagnetic shift of states with non-zero orbital moment are clearly observed. Moreover, the splitting of doubly degenerate states with opposite spins occurs in non-zero field. It is interesting to compare the prediction of 8kpTUB model with the FD model (Eq. 4.1). We have adjusted the harmonic frequency ω_0 to the separation of s- and p-levels ($\omega_0 = 72$ meV), and the effective mass to the s-level diamagnetic shift at 30 T ($m^* = 0.0567\, m_0$). The values of particular energy shifts at 30 T calculated by means of 8kpTUB model (FD model) are (all values have been averaged over the two levels of opposite spins): s-level shift 6.23 meV (6.22 meV; note that the good agreement is due to the setup of FD parameters), p-level diamagnetic shift 10.30 meV (12.43 meV), p-level paramagnetic splitting 57.0 meV (61.3 meV). The paramagnetic splitting is only slightly overestimated by the FD model, the relative discrepancy of the diamagnetic shift of excited levels is larger.

The situation for hole levels, shown in Figure 6.13, is more complex. The holes are heavier than electrons and therefore experience the piezoelectric reduction of symmetry more strongly. Moreover, the band mixing, particularly of heavy and light holes, is more pronounced. The

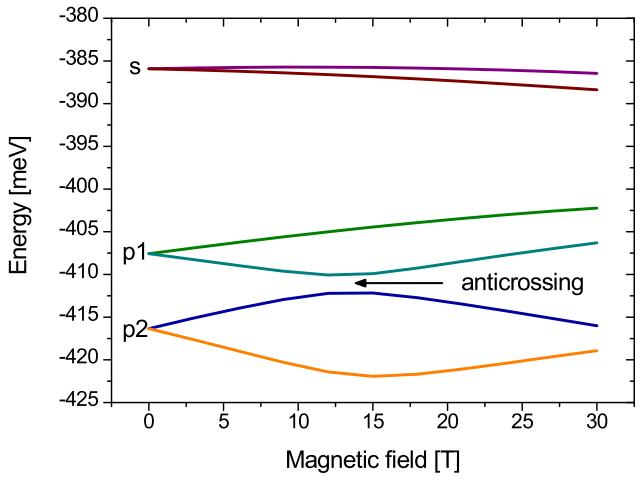

Figure 6.13: The hole energies in the lens-shaped quantum dot with the height of 3 nm and the diameter of 20 nm in magnetic field. The arrow denotes the anticrossing between p-levels.

behavior of the ground state is similar to the electron case showing the diamagnetic shift and spin splitting. For excited states (of the p-like character), the following discrepancies with the FD model occur: a) There is a splitting of p-states at zero field with the magnitude of 9 meV due to piezoelectricity. b) The spin splitting is comparable to the bound state orbital moment splitting. c) Excited states exhibit an anticrossing behavior (e.g. at 13 T in Fig. 6.13), which is connected to piezoelectricity. When the piezoelectric field is excluded from our model, the standard crossing behavior is restored.

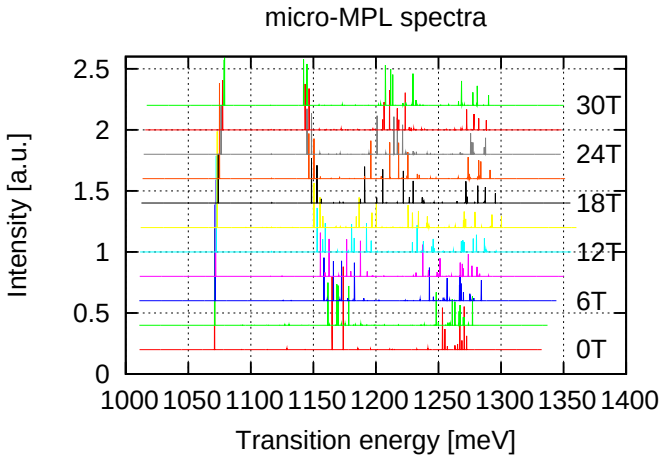

Figure 6.14: The transition energies in the lens-shaped quantum dot with the height of 3 nm and the diameter of 20 nm in magnetic field. Each transition is represented by a narrow line with the amplitude proportional to the transition probability.

The optical transitions, calculated using the Fermi golden rule, are displayed in Figure 6.14. The FD pattern for magnetic field is restored, since the energy shifts are significantly larger for electrons than for holes. In the following, we denote the transitions according to the approximate symmetry of involved states as s-transition (for the ground transition) and p-transition (the excited transition between the p-like states). We also average all energy shifts over two transitions of opposite spins. For the QD considered above and the magnetic field of 30 T, the diamagnetic shift of the s-transition is 7.73 meV, and the diamagnetic shift and paramagnetic splitting of the p-transitions are 12.72 meV and 77.10 meV, respectively. The FD model, with the effective mass fitted to the s-transition ($m^* = 0.044$), gives the p-transition diamagnetic shift of 15.22 meV and the paramagnetic splitting of 77.18 meV.

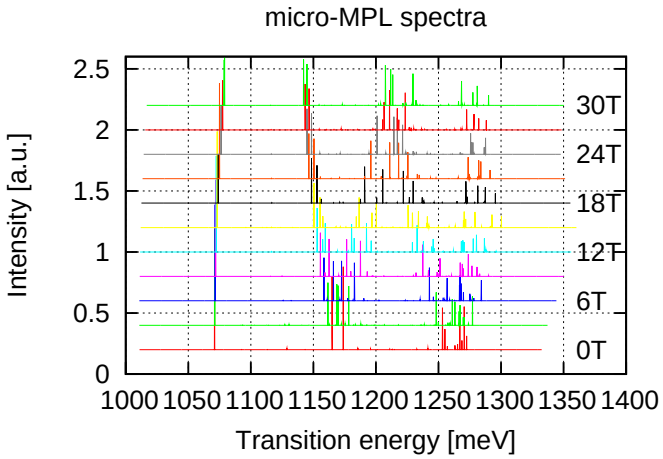

Figure 6.15: The transition energies in the lens-shaped quantum dot with the height of 3 nm and the diameter of 20 nm in magnetic field. Each transition is represented by a Gaussian with the FWHM of 30 meV and the amplitude proportional to the transition probability.

Figure 6.15 displays the optical transitions artificially broadened by 30 meV FWHM Gaussians. This emulates approximately the inhomogeneous broadening of structures in the optical measurements (e.g., photoluminescence bands) on quantum dots. A comparison with single dot spectra (Fig. 6.14) reveals that structures in broadened spectra consist of several microscopic structures. The detailed structure of transitions cannot be completely retrieved from the spatially unresolved measurements, which underlines the importance of single-dot measurements, e.g., microphotoluminescence, cathodoluminescence, etc. We note that real spectra are even more complex than those displayed in Fig. 6.14, in particular due to various excitonic complexes participating in the transitions, as well as due to charged traps in the vicinity of quantum dots.

6.2.2 Exciton in magnetic field

The Coulomb energy (including both direct and exchange interaction) between the ground electron and hole state is displayed in Figure 6.16 for the same QD as in the previous sub-

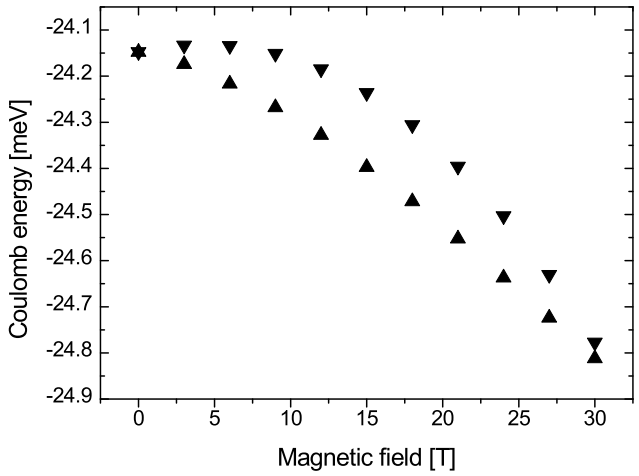

Figure 6.16: The binding energies of two bright excitons in the lens-shaped quantum dot with the height of 3 nm and the diameter of 20 nm in magnetic field. The energies have been calculated using CI method with the basis composed of single particle s-states.

section, i.e., the lens with the height of 3 nm and the diameter of 20 nm. A substantial part of the Coulomb energy comes from the direct interaction, it varies from -24.44 meV for 0 T to -25.11 meV for 30 T. The increase of its amplitude can be understood by considering the additional magnetic-field-induced confinement: the wave functions becomes squeezed, and the Coulomb interaction is increased [148]. This effect decreases effectively the diamagnetic shift by approximately 10 %. The exchange energy varies between 236 μeV and 313 μeV

Another effect of the Coulomb interaction is the change (squeezing) of the wave functions due to the attraction of the electron and hole. In our CI approach this is described by correlation, which is treated by incorporating Slater determinants composed of higher states into the exciton wave function. Including the p-states into the basis (i.e., using 6 states for electrons and 6 for holes), we found the correlation energy of 0.55 meV at zero magnetic field. For magnetic field ranging from 0 T to 30 T, it exhibits mostly stepwise changes (see Figure 6.17), which are attributed to the (anti)crossing of single-particle levels (the lowest energy levels are used as the CI basis, the character of the basis is therefore modified after each level crossing). The low value of the correlation energy demonstrates the fact that the excitons are in a strong confinement regime in the dot under consideration; for larger QDs, the correlation effect would be more pronounced [73].

6.2.3 Lateral elongation

We have found a pronounced effect of the lateral elongation of a quantum dot on its magnetooptical properties using the generalized FD model (Sec. 6.1). The aim of this part is to verify our previous results and to increase their accuracy. We study here five model quantum dots. We use the shape of the lens, since its effective lateral confinement potential corresponds rather well to harmonic FD potential. All dots have the identical height (3 nm) and volume

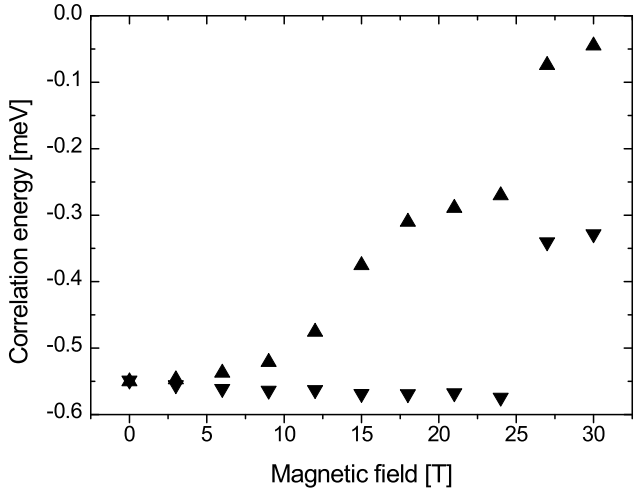

Figure 6.17: The correlation energies of two bright excitons in the lens-shaped quantum dot with the height of 3 nm and the diameter of 20 nm in magnetic field. The energies have been calculated using CI method as the differences of the binding energies obtained using the basis composed of single particle s-states and p-states (i.e, including the correlation), and the binding energies obtained using the basis composed of single particle s-states only (i.e, excluding the correlation).

(the radius of the circular dot is chosen to be 10 nm), their elongation L varies from 1.00 to 1.96 (1.00, 1.21, 1.44, 1.69, 1.96).

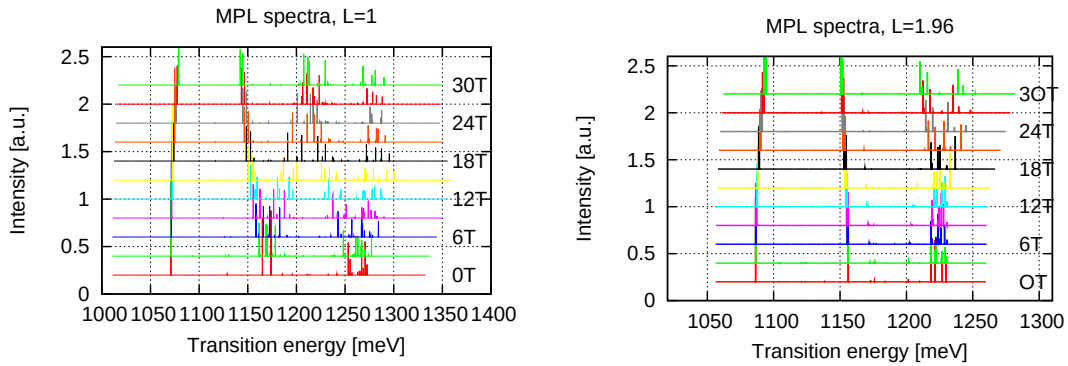

Figure 6.18: The transition energies of the circular quantum dot (left panel) and the elongated quantum dot with the elongation ratio of 1.96 (right panel) in magnetic field. The height of both dots is 3 nm, the diameter of the circular dot is 20 nm, and lateral dimensions of the elongated dot are 28.0 and 14.3 nm (i.e., the volume of both dots is equal). Each transition is represented by the narrow line with the amplitude proportional to the transition probability.

Figure 6.18 displays transition energies in the magnetic field up to 30 T for the circular ($L = 1$, left panel) and the most elongated ($L = 1.96$, right panel) quantum dot. The flattening of p-transition energy dependencies for the elongated dot, caused by the breakdown of rotation symmetry, is evident.

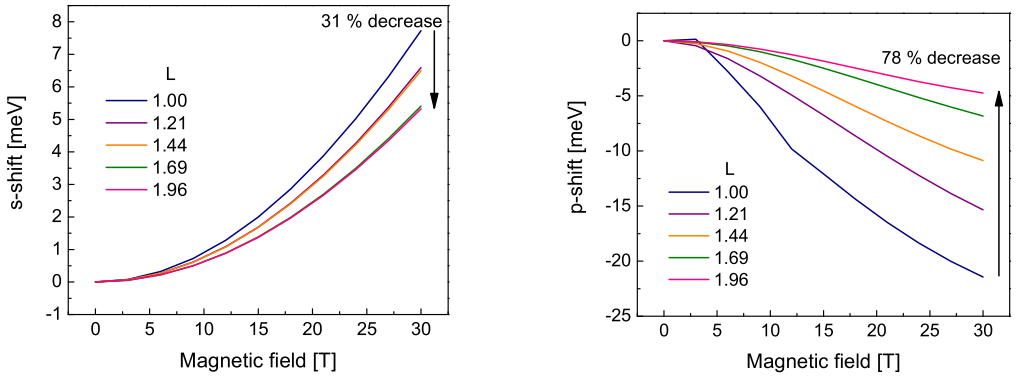

Figure 6.19: The energy shift of the s-transition (left panel) and the lower p-transition (right panel) in elongated lens-shaped quantum dots with the height of 3 nm in magnetic field. The volume of all dots is identical. The s-transition energy shift has been corrected for the discretization error.

The energy shifts of the s-transition and lower p-transition in magnetic field are depicted in Figure 6.19. We again observe a pronounced decrease of the p-transition shift with elongation (from -21.4 meV to -4.8 meV, i.e., by 78 % when changing L from 1.00 to 1.96) as well as a fair decrease of the s-transition shift (from 7.7 meV to 5.3 meV, i.e., by 31 % when changing L from 1.00 to 1.96). The latter has been corrected for the harmonic frequency and discretization error. The energy separation between two lowest transitions decreases as the dot is elongated, which results in an unwanted increase of the diamagnetic shift not connected with an increase of the elongation. Furthermore, this decrease of the energy separation is not smooth due to the discretization of the structure within numerical procedures (see also Fig. 6.20). To overcome the problem, we have used a semiempirical correction provided by the generalized FD model. Its parameters, ω_x and L, have been determined from the separation energy and the structural elongation, the effective mass has been fitted to the calculated diamagnetic shift. We have subsequently modified ω_x to a value, which is identical for all the dots (the value for the circular dot has been chosen for this purpose), and have recalculated the energy shift using this new value of ω_x. We have not applied the correction to the p-transition energy shift, since the diamagnetic shift of the p-transition is not treated properly by the generalized FD model. We have, however, to keep in mind that the problem is present also for all remaining transitions. Figure 6.20 displays the energy shifts at 30 T for the s-transition (both raw and corrected values) and the p-transition.

In the following we compare the 8kpTUB results with those obtained from the generalized FD model. The FD parameters have been set as follows: L has been determined by the dot

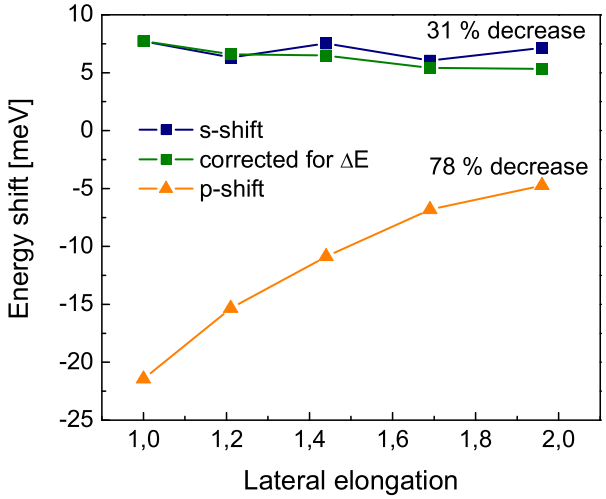

Figure 6.20: The energy shift of the s-transition (blue boxes – raw data, green boxes – corrected for the discretization error), and the lower p-transition (orange triangles) in elongated lens-shaped quantum dots with the height of 3 nm in magnetic field of 30 T as a function of the lateral elongation. The volume of all dots is identical.

structure, ω_x from the energy separation of the two lowest transitions at zero field, m^* has been fitted to the calculated s-transition energy shift.

The energy shifts of s- and lower p-transition at 30 T calculated by means of 8kpTUB and FD methods are displayed in Figure 6.21 (the values are not corrected). The magnitudes of the s-transition shift naturally agree perfectly because the parameters of the FD model have been fitted for the best agreement. Both methods also predict qualitatively similar dependences of the p-transition shift on the elongation, i.e., the rapid decrease of the shift with an increase of the elongation. However, the magnitudes of the effect are different: 8kpTUB predicts the decrease of the p-transition energy shift from -21.4 meV to -4.8 meV, i.e., by 78 % when changing L from 1.00 to 1.96, while FD predicts the decrease from -23.3 meV to -0.9 meV, i.e., by 96 %.

The lower p-transition shift is composed of two parts: a diamagnetic shift and a paramagnetic shift. It is possible to decompose it when also the shift of the upper p-transition is known (or even without that knowledge using approximative assumptions). We take the mean value of both p-transition shifts as the diamagnetic shift, and the difference as the paramagnetic splitting. The results of the decomposition are displayed in Figure 6.22. The FD model overestimates systematically the diamagnetic shift, with the difference up to 4.2 meV (40 % on the relative scale). Both methods agree very well for the paramagnetic shift (a half of the splitting), differences do not exceed to 1.1 meV (2 % on a relative scale).

In conclusion, the generalized FD model is capable to determine the elongation of quantum dots with the same accuracy as the 8kpTUB model, provided both p-transitions are used to determine the p-transition paramagnetic shift. When only the lower p-transition was used, the prediction of FD model would still be qualitatively correct, but the accuracy would be

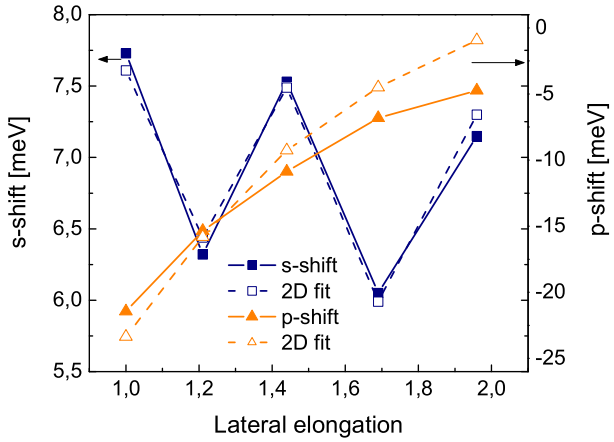

Figure 6.21: The energy shift of optical transitions in elongated lens-shaped quantum dots of identical volume with the height of 3 nm in magnetic field of 30 T as a function of the lateral elongation. Two lowest transitions are shown: the s-transition (blue boxes) and the lower p-transition (orange triangles). The results of 8kpTUB calculations (raw data without any correction) are depicted by full symbols, those of the the best fit FD model by empty symbols. The lines serve as guides to the eye.

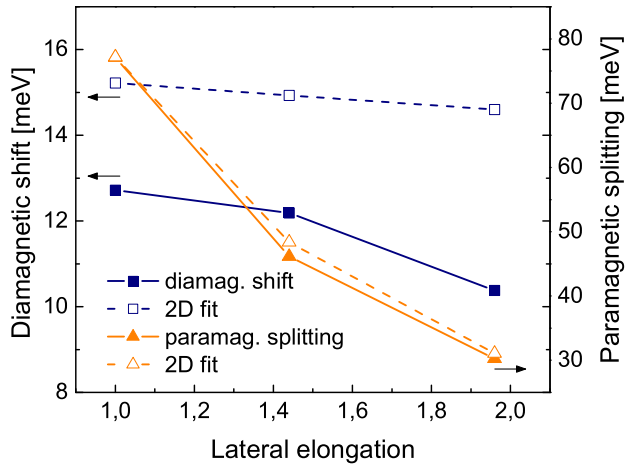

Figure 6.22: The decomposition of the lower p-transition energy shift to the diamagnetic shift (blue boxes) and the paramagnetic splitting (orange triangles) as a function of the lateral elongation. The data have been calculated for elongated lens-shaped quantum dots of identical volume with the height of 3 nm in magnetic field of 30 T. The results of 8kpTUB calculations (raw data without any correction) are depicted by full symbols, those of the best fit FD model by empty symbols. The lines serve guides to the eye.

somewhat reduced. The differences in the p-transition diamagnetic shift are discussed further in the next subsection.

6.2.4 Other structural parameters

In this part, we examine the effect of particular vertical profiles (cylinder → lens → cone, box → pyramid), aspect ratio (flat dots → tall dots), and roundness/squareness of the dot basis (cylinder → box, cone → pyramid). On the basis of very simple considerations we are led to the following expectations: The squareness and lateral elongation of the dot basis are similar, both reducing the circular symmetry. We therefore expect a similar impact to the magnetooptical properties, which is a rather pronounced modification (probably a reduction) of the paramagnetic splitting, possibly rather pronounced, accompanied by only a minor change of the diamagnetic shift. On the other hand, the vertical profile and aspect ratio have no impact to the circular symmetry, we therefore do not expect any pronounced impact on the paramagnetic splitting. Thinking in terms of the FD model, there should be no impact of those parameters on the dots with the circular basis, unless the effective mass was modified. Since the effective mass is in general energy dependent, it is reasonable to keep the energy levels (or at least the transition energies) constant for all the dot systems involved in the comparison in order to exclude the effects of indirectly modified mass value. The only thing we can say in advance about the effect of the vertical profile and the aspect ratio to the diamagnetic shift is that we expect there is some. It might result from the non-harmonic effective lateral confinement potential, as well as from the three-dimensional confinement effects. However, full calculations are needed in order to specify it even qualitatively.

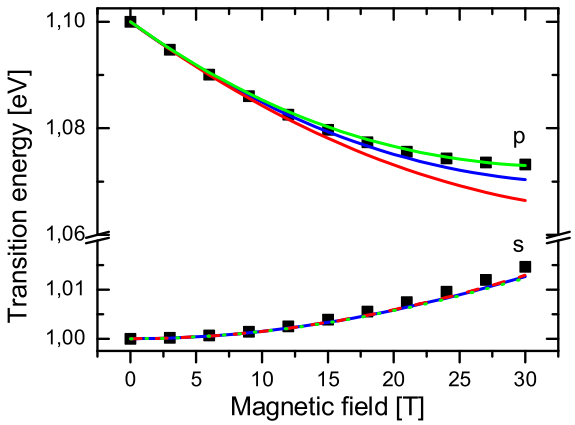

Figure 6.23: The energy shifts calculated for the dot with the lowest transition energies of 1.0 and 1.1 eV. The lines represent results of the three-dimensional single-band effective mass calculations (VM) for the lens- (solid), cylinder- (dashed), and cone-shaped (dotted) dot. The corresponding FD solution ($\omega_x = 100\,\mathrm{meV}$, $m^* = 0.031\,m_0$, $L = 1$) is shown by squares.

We begin our study by reviewing of cone, lens, and cylinder-shaped QDs described within the single-band k.p theory, in particular, using the variational method (Sec. 3.3). The sizes of the dots have been tuned to the same lowest transition energies of 1.0 and 1.1 eV. Two lowest transition energies are shown in Figure 6.23 as functions of magnetic field. The s-transition diamagnetic shift and the p-transition paramagnetic splitting are equal for all QDs (at 30 T, 12.6 meV and 107 meV, respectively). Differences occur in the p-transition diamagnetic shift, which is 20.2 meV for the cylinder, 23.6 meV for the lens, and 26.1 meV for the cone. The FD model fitted to the s-transition diamagnetic shift predicts 25.2 meV, which is similar to the cone case. The ratio of diamagnetic shift of p- and s-transition is almost constant for the magnetic field ranging from 0 T to 30 T. The values of the ratio are 1.60 for the cylinder, 1.87 for the lens, and 2.07 for the cone, while the FD model predicts the value of 2 (exact).

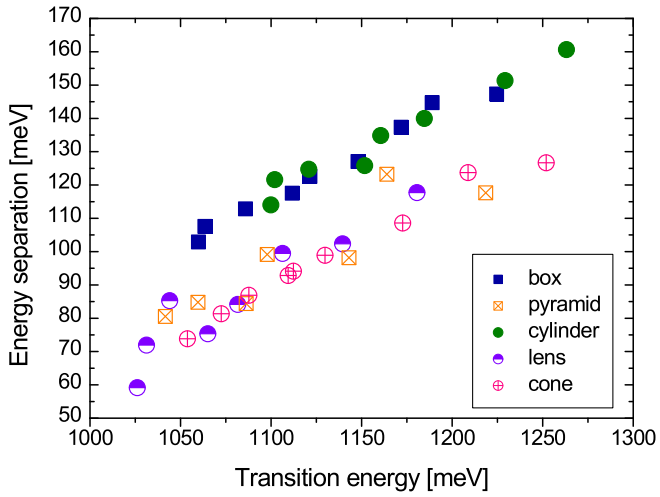

Figure 6.24: The energy separation of the two lowest transition energies as a function of the lowest transition energy in quantum dots with various dimensions for several shapes: box (blue squares), pyramid (orange squares), cylinder (green circles), lens (violet circles), and cone (pink circles).

In order to select proper dot dimensions, we have calculated the transition energies for several shapes (cone, pyramid, lens, cylinder, box) and sizes. The results are interesting, although the size variation is not systematic. In general, the ground transition energies decrease as the dot volume increases, while the effect of the aspect ratio is rather weak. Figure 6.24 displays the energy separation between the two lowest transition energies against the lowest transition energy. It is very surprising that points representing particular dots form approximately two linear dependences, one for the extended shapes (cone, pyramid, lens), second for the compact shapes (cylinder, box). It means that the energy separation is (for a specific shape) determined to a large extent by the lowest transition energy, and vice versa. This fact is in sharp contradiction with our previous knowledge (Sec. 3.2); it is explained by a complex interplay between the confinement and strain effects. This peculiar feature is valid only for rather tall dots, as both energies are rather independent for flat dots.

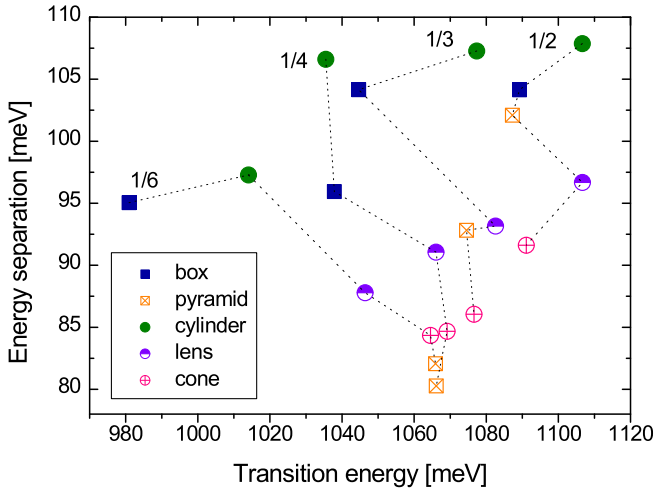

Figure 6.25: The energy separation of the two lowest transition energies as a function of the lowest transition energy in quantum dots of several shapes: box (blue squares), pyramid (orange squares), cylinder (green circles), lens (violet circles), and cone (pink circles). The volume of all dots is identical, the aspect ratio takes several values (1/6, 1/4, 1/3, 1/2). Symbols representing the dots with identical aspect ratio are connected with dotted lines, the numbers indicate the value of aspect ratio.

We further compare magnetooptical properties of five different shapes (cone, pyramid, lens, cylinder, box) and four values of the aspect ratios A (1/6, 1/4, 1/3, 1/2), calculated within the 8kpTUB model. The volume has been kept constant (for example, the flattest box has the height of 2.82 nm and the lateral dimension of 16.88 nm). The transition energies are displayed in Figure 6.25. The ground transition energies vary from 0.981 eV (box, $A = 1/6$) to 1.107 eV (lens and cylinder, $A = 1/2$). Higher aspect ratios mean always higher ground transition energy. This increase is caused by the increase of strain, which overcomes the lower quantum confinement caused by increasing the lowest dimension (i.e., the height). The increase is most pronounced for the compact shapes like cylinder and box (from 0.981 eV to 1.089 eV for box), for the extended shapes (pyramid, cone, lens) it is reduced (from 1.066 eV to 1.087 eV for pyramid). The energy differences between the first excited and ground transition vary from 80 meV to 108 meV, being slightly higher for the compact shapes, and increasing with increasing transition energy.

We have studied various calculated energy shifts as functions of various parameters. All the dependences were rather complex and difficult to interpret. As an example, we display the electron ground level diamagnetic shift at 30 T against the s-p level energy separation in Figure 6.26. In the FD model, the diamagnetic shift decreases as the separation increases. Such tendency is observed also in Fig. 6.26 for particular shapes; however, the influence of additional (uncontrolled) parameters is also evident. The most conclusive were the dependencies on the ground transition energy, which are in more detail discussed in the following. In future the study shall be extended to include more model dots (in particular, various volumes) in order to elucidate the complex dependencies.

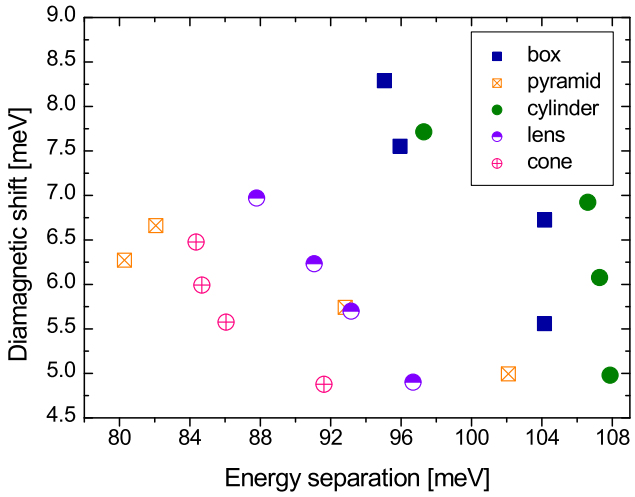

Figure 6.26: The diamagnetic shift of the lowest transition at 30 T as a function of the energy separation of the two lowest transition energies in quantum dots of several shapes: box (blue squares), pyramid (orange squares), cylinder (green circles), lens (violet circles), and cone (pink circles). The volume of all dots is identical, the aspect ratio takes several values (1/6, 1/4, 1/3, 1/2).

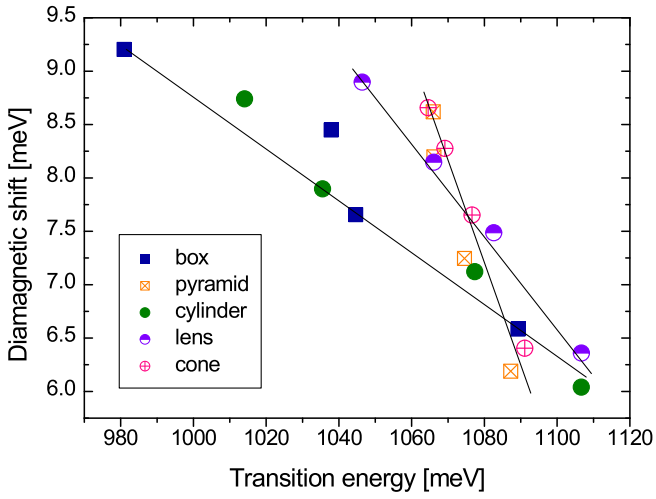

Figure 6.27: The diamagnetic shift of the lowest transition (s-transition diamagnetic shift) at 30 T as a function of the lowest transition energy in quantum dots of several shapes: box (blue squares), pyramid (orange squares), cylinder (green circles), lens (violet circles), and cone (pink circles). The volume of all dots is identical, the aspect ratio takes several values (1/6, 1/4, 1/3, 1/2). The lines guides to the eye.

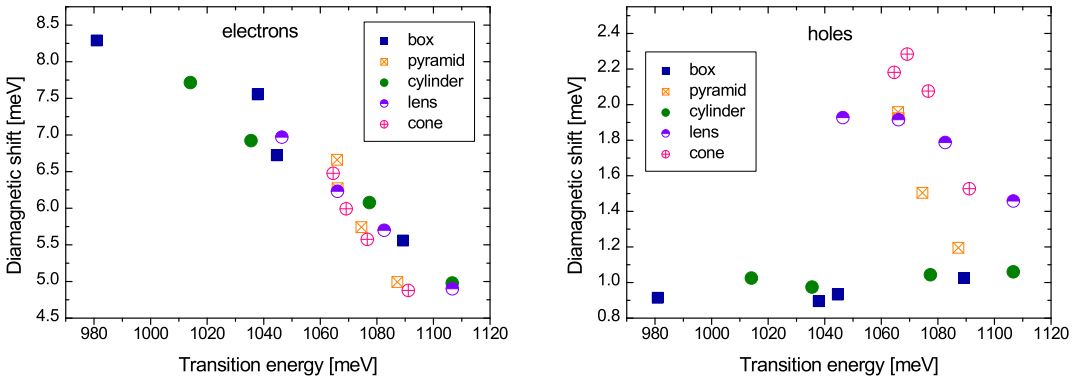

Figure 6.28: The contribution of electrons (left panel) and holes (right panel) to the diamagnetic shift of the lowest transition at 30 T as a function of the lowest transition energy in quantum dots of several shapes: box (blue squares), pyramid (orange squares), cylinder (green circles), lens (violet circles), and cone (pink circles). The volume of all dots is identical, the aspect ratio takes several values (1/6, 1/4, 1/3, 1/2).

The s-transition diamagnetic shift is displayed in Figure 6.27, the contributions of the electron and hole levels to this shift in Figure 6.28. The electron part of the shift is determined predominantly by the ground transition energy: it decreases as the transition energy increases. This behavior has a simple explanation. Both effective mass and harmonic frequency decrease as the transition energy increases, which leads to a decrease of the diamagnetic shift. The effect of the shape on the diamagnetic shift is rather small, which is in agreement with the prediction of the VM method, where no effect is expected (compare Figure 6.23). The hole part of the shift behaves differently for extended shapes (the shift decreases as the transition energy increases, just as for electrons) and for compact shapes (the shift is practically independent of the transition energy). The diamagnetic shift of the s-transition decreases as the transition energy increases, the rate of the decrease is the largest for cones and pyramids followed by lenses, the lowest values apply to cylinders and boxes. It is, in principle, possible to distinguish between the extended and compact shapes from the measured diamagnetic shift; however, the differences are rather small. Very promising fact is that the dependencies of the diamagnetic shift on the transition energy (different rate of decrease) suggest more pronounced differences for lower transition energies. Further calculations are required in order to prove this assumption.

Figure 6.29 displays the diamagnetic shift of the p-transition. The values of the shift are determined by the transition energy and vertical profile, with the clear differences between compact and extended shapes for transition energies below 1.06 eV. Therefore, the measurement of the shift should allow the specification of the vertical profile. There is no significant difference between the round and square-based dots. The diamagnetic shift of the s-transition is qualitatively similar, in contradiction to single-band $\vec{k} \cdot \vec{p}$ theory. Higher values resulting for extended shapes are mainly due to the hole contribution.

The paramagnetic splitting of the p-transitions is displayed in Figure 6.30. It decreases slightly with increasing transition energy, from 84 meV to 62 meV (with the exception of pyramids). There is no clear effect of particular dot shape for lens, cone, cylinder and box.

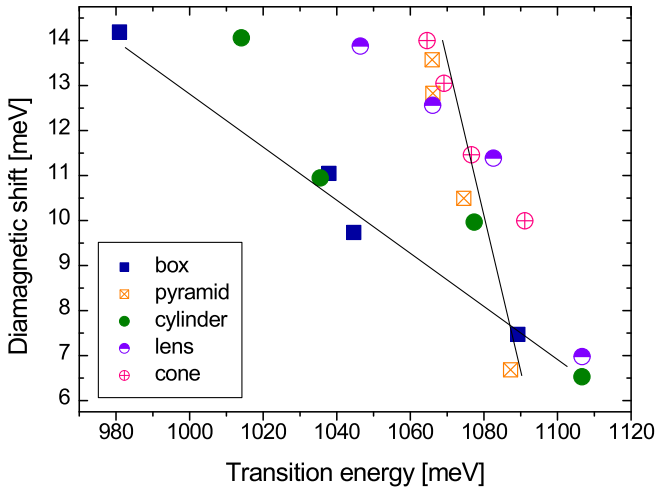

Figure 6.29: The p-transition diamagnetic shift at 30 T as a function of the lowest transition energy in quantum dots of several shapes: box (blue squares), pyramid (orange squares), cylinder (green circles), lens (violet circles), and cone (pink circles). The volume of all dots is identical, the aspect ratio takes several values (1/6, 1/4, 1/3, 1/2). The lines are guides to the eye.

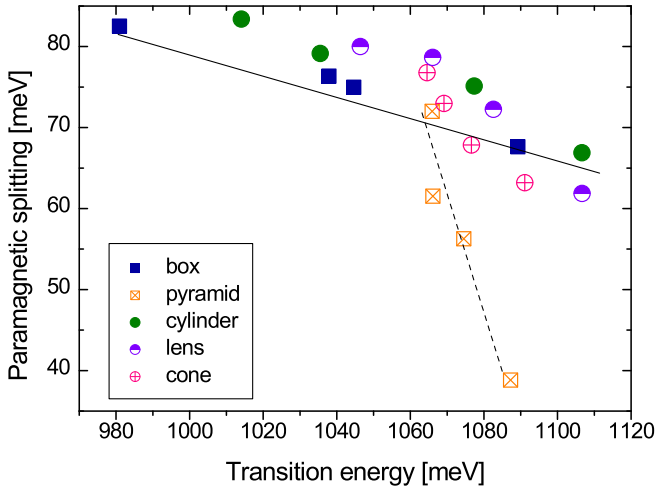

Figure 6.30: The paramagnetic splitting of the p-transition at 30 T as a function of the lowest transition energy in quantum dots of several shapes: box (blue squares), pyramid (orange squares), cylinder (green circles), lens (violet circles), and cone (pink circles). The volume of all dots is identical, the aspect ratio takes several values (1/6, 1/4, 1/3, 1/2). The lines guides to the eye.

This is rather surprising in the case of the box, where the rotational symmetry is broken and a change of the paramagnetic splitting would be expected, similarly to the case of symmetry breaking by the lateral elongation [19]. However, the finite effective mass of particles leads to smooth wave functions and to partially restoring the rotational symmetry, which explains the observed behavior. The paramagnetic splitting in pyramids is reduced (for $A = 1/2$, it is 64 meV in the cone, but only 39 meV in the pyramid). This decrease is in part due to the broken rotational symmetry, but mainly due to the larger piezoelectric splitting of the p-states in pyramids (for $A = 1/6$, where the piezoelectric splitting is small for both pyramid and cone, the difference in their paramagnetic splitting is as low as 5 meV).

In conclusion, the most important structural parameter influencing the magnetooptical properties of those discussed here is the vertical shape. From measurements of the diamagnetic shift we are able to distinguish between the compact (box, cylinder) and extended (pyramid, cone, lens) QDs. The square basis leads to a reduced paramagnetic splitting for pyramids; no such effect was found for boxes (although it may be expected in larger dots). The aspect ratio influences zero-field energies, it has no observable effect on the magnetooptical properties.

6.2.5 Effect of piezoelectric field

Recently, a considerable effort is focused on studying the sources of the lateral asymmetry of QDs electronic confinement [73, 86, 149]; it is an important parameter describing fine structure splitting [150]. The evolution of energy levels in magnetic field provides an excellent tool for the study of such asymmetry [19]. The symmetry of the wave functions can be reduced by an asymmetry of the QD geometry, but also due to the C_{2v} atomistic symmetry of constituent materials, in particular by the piezoelectric field (PEF).

In this subsection, we investigate in detail the effect of the wave function lateral asymmetry induced by PEF on the shift of energy levels in the magnetic field parallel to the growth axis. The electronic structure calculations have been carried out using the 8kpTUB method. As the suitable model system, we choose an InAs pyramidal QD embedded in GaAs matrix, with its base edges parallel to the [100] and [010] directions on the (001) oriented substrate.

In most of this subsection, we discuss the electron levels rather than excitonic transitions. There are two reasons for such restriction: (1) The evolution of the hole levels is very complex; influenced by band-mixing resulting in level anticrossing [146]. Identification of the lateral asymmetry effects is therefore rather difficult for the holes. (2) Since the mass of the electrons is smaller than that of the holes, the resulting evolution of the exciton levels is mainly driven by the electron levels.

The PEF in the considered QDs has an octopole character, with the potential maxima along $[11\bar{1}]$, $[1\bar{1}1]$, $[\bar{1}11]$, $[\bar{1}\bar{1}\bar{1}]$ and potential minima in [111], $[1\bar{1}\bar{1}]$, $[\bar{1}1\bar{1}]$, $[\bar{1}\bar{1}1]$ directions with respect to the dot center. However, in the critical region near the position of the wave function, the PEF is very well described by its quadrupole part, with the potential maxima along $[1\bar{1}0]$ and potential minima along [110] directions (see Figure 6.31). The electron and hole wave functions are elongated in the $[1\bar{1}0]$ and [110] directions, respectively. The electron p-levels are split by the PEF (the hole levels are split even without taking the PEF into account due to the band mixing; the same effect occurs in fact for electrons as well, but the magnitude of this splitting is rather small); the wave function with a nodal plane perpendicular to the elongation direction has lower energy than the second one.

One possible way of tuning the PEF is the change of the QD volume; for larger dots, the effect of PEF is more pronounced [73]. We present here the calculation of the electron

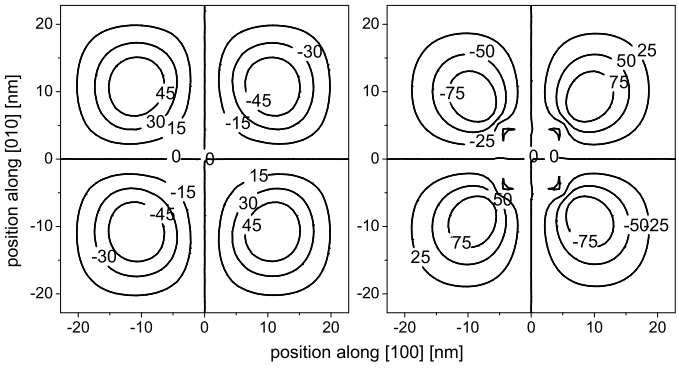

Figure 6.31: The contour plot of the piezoelectric potential around the pyramidal InAs/GaAs quantum dot with the 22.4 nm base length: the planar intersection 5 nm below the dot base (left) and 5 nm above the dot base (right). The contour labels are in mV.

energy levels in magnetic field up to 30 T for a set of pyramidal quantum dots with the aspect ratio of 0.5 and the base length of 7.9, 11.2, 14.0, 16.8, 19.6, and 22.4 nm. For each structure, we perform the calculation including PEF up to the second order, and a reference calculation excluding any PEF. The s-level (ground state) energy (measured from the top of the unstrained InAs valence band) at 0 T varies from 847 meV for the smallest dot to 590 meV for the largest one; negligible differences up to 2 meV are found for the reference system. The energy difference between the s- and p-level (with the p-level energy averaged over four p-levels) varies from 136 meV (the smallest dot) to 52 meV (the largest dot); differences for the reference system are again very small, not exceeding 2 meV. The PEF splits the p-levels; the magnitude of this splitting varies from 10 meV (7 % of s-p energy difference) for the smallest dot to 31 meV (60 %) for the largest one. No such splitting occurs for the reference system, the p-levels are degenerate with the accuracy better than 1 meV. The relative magnitude of the p-level splitting with respect to the s-p energy difference is clearly a good measure of lateral asymmetry, it demonstrates a pronounced increase of the asymmetry with increasing the volume for the dots considered here.

In magnetic field the energy levels are shifted. The diamagnetic shift of s-levels at 30 T (averaged over the two spin orientations) varies from 2.04 meV (the smallest dot) to 10.2 meV (the largest dot), the differences for the reference system are up to 2 %. The paramagnetic splitting (the value is averaged over two spin orientations, 0 T splitting due to the PEF is subtracted) at 30 T is depicted in Figure 6.32. Without PEF, the increase of the volume is accompanied by the decrease of the paramagnetic shift, attributed to the increase of the electron effective mass [4] (see also Eq. 2.1). Including PEF into the calculations, a reduction of the paramagnetic shift occurs, attributed to the lateral elongation of the wave function. The value of the elongation estimated from the planar intersection of the 50% of density maximum surface at its maximum dimension varies from 1.1 (the smallest dot) to 1.8 (the largest dot).

Furthermore, we compare here the calculated shifts with those predicted by the two-dimensional generalized Fock–Darwin model (FD model), described in [19] (see also Eq. 6.1). The only free parameter of the FD model, the effective mass, has been fitted to the diamagnetic shift predicted by the 8kpTUB model. The resulting values of the mass depend on the

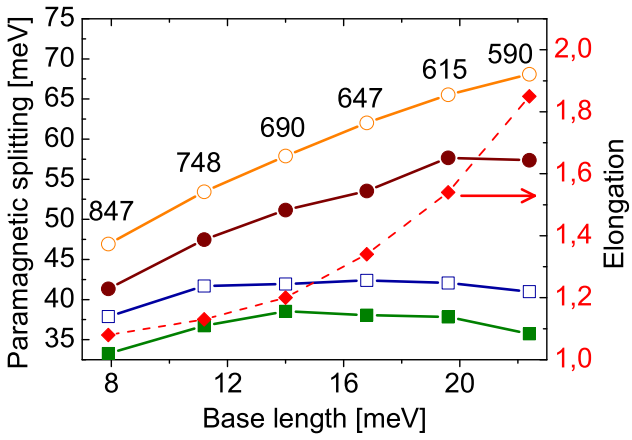

Figure 6.32: Paramagnetic splitting of electron the p-levels at 30 T for pyramidal dots of different volume with the aspect ratio of 1/2. The results obtained within the 8kpTUB (FD model) are depicted by full (empty) symbols, respectively. The results including (excluding) PEF are depicted by squares (circles). The lines are guides to the eye. The labels denote the corresponding s-level electron energies (8kpTUB model with PEF). The elongation estimated from the ratio of s-p1/s-p2 energy differences is depicted by diamonds.

s-level energy (0.074 for the smallest dot and 0.052 for the largest dot in free electron mass units), which is in agreement with the prediction of the $\vec{k} \cdot \vec{p}$ theory [4] (cmp. Fig. 3.20); no influence of PEF on the mass values is observed. Two s-p energy differences provide two harmonic potential frequencies; their ratio corresponds to the lateral elongation in the FD model. The calculated values of the paramagnetic splitting at 30 T are depicted in Figure 6.32. They are somewhat higher than those predicted by the 8kpTUB calculations, the differences related to 8kpTUB calculations results being between 9 and 15 % with the inclusion of PEF, and 13-19 % for the reference case. We attribute these differences mainly to non-parabolicities in both band dispersion and lateral confinement; a minor part (up to 4%, the value has been found from the comparison of the pyramidal and conic dots with identical volume) can be explained by the squareness of pyramids, not included in the FD model. Since no systematic changes of these differences occur with changing the dot volume, we suppose no effect of the wave function elongation. Therefore, we conclude that the elongation predicted within the FD model as a ratio of two harmonic frequencies describes properly the wave function elongation in 8kpTUB calculations. It varies from 1.1 (the smallest dot) to 1.9 (the largest dot); these results are in agreement with those discussed above. We have demonstrated that the increasing magnitude of PEF due to increasing volume produces laterally elongated wave functions.

It is also possible to modify the magnitude of PEF by changing the aspect ratio of the dot; higher aspect leads to higher shear strain and therefore higher PEF. The important advantage of this approach is that when the volume is preserved, the s-level energy varies only very little for a large interval of aspect ratios. Therefore direct comparison of the results is possible and no reference calculations are necessary. We compare here two pyramidal dots. The flat dot

with base length 24.3 nm and aspect ratio 1/6 has an electron s-level energy 680 meV, s-p energy separation 68 meV and p-levels splitting 4.2 meV, at 30 T it exhibits 6.7 meV s-level diamagnetic shift and 52 meV p-levels paramagnetic splitting. The tall dot with base length 16.9 nm and aspect ratio 1/2 (identical volume) has a comparable s-level energy 670 meV, slightly larger s-p energy separation 86 meV, and fairly larger p-levels splitting 18 meV. The shifts of the energies are reduced, the value of s-level diamagnetic shift at 30 T is 5.0 meV and the value of p-levels paramagnetic splitting is 39 meV. The decrease of diamagnetic shift is explained by increased s-p separation, the decrease of paramagnetic splitting (not influenced by s-p separation) by the lateral elongation of the wave function due to PEF (which causes also increased p-levels splitting at 0 T). For the reference calculations without PEF, p-levels are degenerate at 0 T and the paramagnetic splitting reads 56 meV (54 meV) for flat (tall) dot; the other parameters are not modified.

6.2.6 Conclusions

We have discussed effects of morphology of quantum dots (lateral elongation, aspect ratio, vertical profile, basis roundness/squareness), piezoelectric field, and exciton interaction to the magnetooptical properties of quantum dots.

The lateral elongation of quantum dot basis has a pronounced impact to paramagnetic splitting of higher optical transitions in magnetic field: an increase of the elongation is accompanied by a decrease of the splitting. The magnitude of the effect is sufficient for a determination of the elongation from the magnetophotoluminescence measurements. The results of full calculations (8kpTUB) and simplified calculations (FD) are in a good agreement.

Particular vertical profile of quantum dot (e.g., cylinder $\rightarrow$ lens $\rightarrow$ cone) influences the diamagnetic shift rather weakly, no effect to the paramagnetic splitting has been observed. It may be possible to distinguish between extended (e.g., cone) and compact (e.g., cylinder) dot shapes from the magnetophotoluminescence measurements on single dots.

No direct effect of the aspect ratio or the basis roundness/squareness to the magnetooptical properties has been found. However, a large aspect ratio or a square basis are factors increasing the piezoelectric field, which subsequently influences the magnetooptical properties.

Piezoelectric field has effectively a quadrupole character. It therefore elongates the wave functions in a similar way as a morphological lateral elongation. Our calculations reveal that its impact to the transition energy shifts is also comparable to the effects of morphological lateral elongation.

The exciton interaction decreases the diamagnetic shift in comparison with a sum of single electron and hole diamagnetic shift, the magnitude of the effect is about 10 % of the total diamagnetic shift.

Summary

This thesis deals with the theoretical calculations performed to obtain the electronic structure of quantum dots. Two methods have been developed: the Variable Thickness Well Approximation and the Variational Method, both based on the single band envelope function theory. We have further used the implementation of the eight band envelope function theory developed at Technische Universität Berlin. The methods have been applied to study InAs/GaAs quantum dots of various morphologies, including the effects of the strain, piezoelectric field, Coulomb interaction, and external magnetic field. The calculations have also been used for interpreting several experimental studies. The most important results are summarized below.

The strain field in and around quantum dots exhibits qualitative features independent of the dot shape. The lateral strain in the dot is compressive due to lattice matching to the substrate, the vertical strain is tensile. The interaction of the side walls with the capping layer acts in the opposite direction, being pronounced especially for tall dots. This leads, e.g., to the region of inversion strain at the tip of pyramidal dots. The total hydrostatic strain is always compressive. Its magnitude increases due to the side interaction as the aspect ratio increases, resulting in larger values of the band gap (excluding the effects of quantum confinement).

The strain is important also for the growth of QDs. We have attributed the low transition energies observed in vertically stacked dots or dots capped with ternary strain reducing layer mainly to the reduction of the strain on the surface of the sample, resulting in the larger volume of the dots. However, the direct effect of the lower strain on the transition energies is negligible.

The energies of bound states and optical transitions are most affected by the volume, decreasing as the volume increases. Their dependence on the aspect ratio is decreasing for flat dots, turning into increasing for tall dots. This is explained by the increase of the strain energy, which overruns the decrease of the quantum confinement energy.

The evolution of the transition energies in magnetic field is rather sensitive to some morphological parameters, allowing their determination from the magnetooptical measurements:
(i) The lateral elongation of the quantum dot basis has a pronounced impact on the paramagnetic splitting of higher optical transitions: an increase of the elongation leads to a decrease of the splitting. The magnitude of the effect is sufficient for the determination of the elongation from the magnetophotoluminescence measurements.
(ii) The choice of a particular vertical profile (e.g., cylinder $\rightarrow$ lens $\rightarrow$ cone) influences the diamagnetic shift rather weakly, no effect on the paramagnetic splitting has been found. It might be possible to distinguish between the extended (e.g., cone) and compact (e.g., cylinder) dot shapes from the magnetophotoluminescence measurements on single dots.
(iii) No direct effect of the aspect ratio or the basis roundness/squareness on the magnetooptical properties has been found. However, a large aspect ratio or a square basis are

factors increasing the piezoelectric field, which subsequently influences the magnetooptical properties.

The piezoelectric field reduces the rotation symmetry and elongates the wave functions. Its impact on the magnetooptical properties has been found to be very similar to that of the structural elongation.

The results of the photoluminescence studies of vertically stacked InAs/GaAs dots with several values of the number of layers and two values of the spacer thickness have been explained. The dot dimensions have been determined: the heights ranging between 2 and 3 nm, the radii between 15 and 30 nm. The measurements reveal that the transition energies decrease as the number of layers increases, which is attributed to the increasing volume. Both dimensions increase with the number of layers; the radii mainly for the thin spacer, the heights mainly for the thick spacer. The communication wavelength of 1.3 μm has been achieved for 7 layers. The smaller width of the photoluminescence bands occurring for larger number of layers has been attributed to the flatter dependence of the energy on the dimensions rather than to a better homogeneity of the dots.

The lowering of the transition energies has also been achieved using the $In_xGa_{1-x}As$ strain reducing layer. This has been attributed to the decrease of the confinement barrier at the SRL side and by the increase of the dot volume, both being about equally strong. The strain relaxation of QDs due to the presence of SRL has been found to have only a minor effect. The dot dimensions have been determined: the heights ranging between 2 and 3 nm, the radii between 15 and 25 nm. Below the 13 % In content in the SRL, the heights increase as the content increases, above 13 %, the radii decrease as the content increases. The most favorable properties, i.e., the low emission energy, and the high energy separation from the excited transition, have been achieved for In content of 13 %.

Finally, we have shown that magnetophotoluminescence spectroscopy is capable to reveal the lateral elongation of buried quantum dots. At least two well resolved photoluminescence bands are required for this purpose. Fitting our model to experimental data, we have determined the elongation for two samples of single-layer InAs/GaAs QDs. The comparison with the AFM results indicates the absence of a pronounced increase of the lateral elongation during the overgrowth.

Outlook

Considerable effort devoted recently to the studies of excitons and excitonic complexes in quantum dots, stimulated by the successful single dot experiments as well as by the potential applications in quantum computing, suggests several possibilities of extensions of the work presented in this thesis. Namely, the following items seem to be attractive:

- Calculations of the binding, exchange, and correlation energies of excitons, trions, and biexcitons in the strain-free GaAs quantum dots embedded in the AlAs matrix. The multistep fabrication process based on a combination of hierarchical self-assembly and in situ etching [11] allows a very precise determination of the dot morphology.
- The study of lateral dot molecules, important for their potential applications as solid-state quantum gates.
- The incorporation of the external electric field, which provides further information on the origin of the optical transitions. By tuning the field, an anticrossing between various transitions might be induced, providing the characteristic coupling energies.

These calculations will probably require a modification of the configuration interaction method presently used, in particular, a modified basis, better suited to the particular problem. Another option is the employment of the Hartree–Fock method, better suited for excitons with large correlation energies.

Regarding the long wavelength emitting quantum dots, several technological improvements are considered, including very thin capping layers. Theoretical description is needed for the interpretation of photoluminescence, and, if appropriate, magnetophotoluminescence spectra. It is also desirable to simulate the growth process, for which the determination of the strain field is necessary.

Most of the theoretical predictions of the magnetooptical properties require an experimental verification. The results of the calculations should be compared systematically with available experimental data. The calculations should be extended to cover a wider range of volumes in order to verify the predictions.

In the calculations, the 8kpTUB method will be used rather than the simple methods, owing to the recent advances in the quantum dot morphology determination [11, 151] as well as to the improvements of the computational performance.

Bibliography

[1] D. Leonard, M. Krishnamurthy, C. M. Reaves, S. P. DenBaars, and P. M. Petroff, Appl. Phys. Lett. **63**, 3203 (1993).

[2] D. Bimberg, in *QUEST Workshop on Quantum Structures, Colloquium Abstracts*, p. 15, Santa Barbara, 1994.

[3] A. Madhukar, Q. Xie, P. Chen, and A. Konkar, Appl. Phys. Lett. **64**, 2727 (1994).

[4] A. Hospodková, V. Křápek, K. Kuldová, J. Humlíček, E. Hulicius, J. Oswald, J. Pangrác, and J. Zeman, Physica E **36**, 106 (2007).

[5] I. E. Itskevich, M. Henini, H. A. Carmona, L. Eaves, P. C. Main, D. K. Maude, and J. C. Portal, Appl. Phys. Lett. **70**, 505 (1997).

[6] Z. I. Alferov *et al.*, Semicond. **30**, 197 (1996).

[7] M. V. Maximov *et al.*, Semicond. **31**, 124 (1997).

[8] M. V. Maximov *et al.*, Jpn. J. Appl. Phys. **36**, 4221 (1997).

[9] T. A. Fulton and G. D. Dolan, Phys. Rev. Lett. **59**, 109 (1987).

[10] R. Held, T. Heinzel, P. Studerus, K. Ensslin, and M. Holland, Appl. Phys. Lett. **71**, 2689 (1997).

[11] A. Rastelli, S. Stufler, A. Schliwa, R. Songmuang, C. Manzano, G. Costantini, K. Kern, A. Zrenner, D. Bimberg, and O. Schmidt, Phys. Rev. Lett. **92**, 166104 (2004).

[12] A. Lenz, R. Timm, H. Eisele, L. Ivanova, D. Martin, V. Vosseburger, A. Rastelli, O. G. Schmidt, and M. Dähne, phys. stat. sol. (b) **243**, 3976 (2006).

[13] I. N. Stranski and L. Krastanow, Sitzungsberichte d. Akad. d. Wissenschaften in Wien, Abt. IIb **146**, 797 (1937).

[14] V. A. Shchukin and D. Bimberg, Rev. Mod. Phys. **71**, 1125 (1999).

[15] W. Richter, Phil. Trans. R. Soc. A **344**, 453 (1993).

[16] P. Weightman, D. S. Martin, R. J. Cole, and T. Farrell, Rep. Prog. Phys. **68**, 1251 (2005).

[17] R. Songmuang, S. Kiravittaya, and O. G. Schmidt, J. Cryst. Growth **249**, 416 (2003).

[18] K. Kuldová, V. Křápek, A. Hospodková, O. B. Zrzavecká, J. Oswald, E. Hulicius, and J. Humlíček, Mat. Sci. Eng. C **26**, 983 (2006).

[19] V. Křápek, K. Kuldová, J. Oswald, A. Hospodková, E. Hulicius, and J. Humlíček, Appl. Phys. Lett. **26**, 983 (2006).

[20] K. Kuldová, V. Křápek, A. Hospodková, J. Oswald, J. Pangrác, K. Melichar, E. Hulicius, M. Potemski, and J. Humlíček, phys. stat. sol. c **3**, 3811 (2006).

[21] D. Bimberg, M. Grundmann, and N. N. Ledentsov, *Quantum dot heterostructures* (Wiley, 1999).

[22] J. Stangl, V. Holý, and G. Bauer, Rev. Mod. Phys. **76**, 725 (2004).

[23] M. Schmidbauer, T. Wiebach, H. Raidt, M. Hanke, R. Köhler, and H. Wawra, Phys. Rev. B **58**, 10523 (1998).

[24] J. Novák, V. Holý, J. Stangl, T. Fromherz, Z. Zhenyang, C. Gang, G. Bauer, and B. Struth, J. Appl. Phys. **98**, 073517 (2005).

[25] F. Heinrichsdorff, A. Krost, M. Grundmann, D. Bimberg, A. Kosogov, and P. Werner, Appl. Phys. Lett. **68**, 3284 (1996).

[26] H. Eisele, O. Flebbe, T. Kalka, C. Preinesberger, F. Heinrichsdorff, A. Krost, D. Bimberg, and M. Dähne-Prietsch, Appl. Phys. Lett. **75**, 106 (1999).

[27] X. Z. Liao, J. Zou, X. F. Duan, D. J. H. Cockayne, R. Leon, and C. Lobo, Phys. Rev. B **58**, R4235 (1998).

[28] J. Zou, X. Z. Liao, D. J. H. Cockayne, and R. Leon, Phys. Rev. B **59**, 12279 (1999).

[29] G. Binnig, C. F. Quate, and C. Gerber, Phys. Rev. Lett. **56**, 930 (1986).

[30] G. Binnig, H. Rohrer, C. Gerber, and E. Weibel, Appl. Phys. Lett. **40**, 178 (1982).

[31] G. Binnig, H. Rohrer, C. Gerber, and E. Weibel, Phys. Rev. Lett. **49**, 57 (1982).

[32] H. Z. Song, M. Kawabe, and Y. Okada, Appl. Phys. Lett. **85**, 2355 (2004).

[33] L. Ouattara, A. Mikkelsen, E. Lundgren, L. Höglund, C. Asplund, and J. Y. Andersson, J. Appl. Phys. **100**, 044320 (2006).

[34] E. E. Vdovin, A. Levin, A. Patane, L. Eaves, P. C. Main, Y. N. Khanin, Y. V. Dubrovskii, M. Henini, and G. Hill, Science **290**, 122 (2000).

[35] O. Millo, D. Katz, Y. W. Cao, and U. Banin, Phys. Rev. Lett. **86**, 5751 (2001).

[36] P. Yu and M. Cardona, *Fundamentals of Semiconductors* (Springer, 2001).

[37] R. Waser, editor, *Nanoelectronics and information technology* (Wiley, 2003).

[38] H. L. Störmer, R. Dingle, A. C. Gossard, W. Wiegmann, and R. A. Logan, Electronic properties of modulation-doped $GaAs - Al_xGa_{1-x}As$ superlattices, in *Physics of Semiconductors 1978*, edited by B. L. H. Wilson, pp. 557, 560, Inst. Phys., Bristol, 1979.

[39] S. Muto, Jap. J. Appl. Phys. **34**, L210 (1995).

[40] K. Imamura, Y. Sugiyama, Y. Nakata, S. Muto, and N. Yokoyama, Japanese Journal of Applied Physics **34**, L1445 (1995).

[41] M. Sugawara, *Self-assembled InGaAs/GaAs quantum dots* (Academic Press, 1999).

[42] Y. Arakawa and H. Sakaki, Appl. Phys. Lett. **40**, 939 (1982).

[43] M. Asada, Y. Miyamoto, and Y. Suematsu, IEEE J. Quantum Electron. **QE-22**, 1915 (1986).

[44] N. Kirstaedter *et al.*, Electron. Lett. **30**, 1416 (1994).

[45] D. Bimberg, J. Phys. D: Appl. Phys. **38**, 2055 (2005).

[46] R. L. Sellin, C. Ribbat, M. Grundmann, N. N. Ledentsov, and D. Bimberg, Appl. Phys. Lett. **78**, 1207 (2001).

[47] R. L. Sellin, C. Ribbat, D. Bimberg, F. Rinner, H. Konstanzer, M. T. Kelemen, and M. Mikulla, Electron. Lett. **38**, 883 (2002).

[48] A. R. Kovsh *et al.*, Electron. Lett. **38**, 1104 (2002).

[49] N. N. Ledentsov *et al.*, Electron. Lett. **39**, 1126 (2003).

[50] H. Saito, K. Nishi, I. Ogura, S. Sugou, and Y. Sugimoto, Appl. Phys. Lett. **69**, 3140 (1996).

[51] A. Zunger, phys. stat. sol. (b) **224**, 727 (2000).

[52] L. W. Wang, J. N. Kim, and A. Zunger, Phys. Rev. B **59**, 5678 (1999).

[53] L. W. Wang, A. J. Williamson, A. Zunger, H. Jiang, and J. Singh, Appl. Phys. Lett. **76**, 339 (2000).

[54] G. Bester, X. Wu, D. Vanderbilt, and A. Zunger, Phys. Rev. Lett. **96**, 187602 (2006).

[55] G. Bester, A. Zunger, X. Wu, and D. Vanderbilt, Phys. Rev. B **74**, 081305 (2006).

[56] G. W. Bryant and W. Jaskolski, Phys. Rev. B **67**, 205320 (2003).

[57] W. Jaskólski, M. Zieliński, G. W. Bryant, and J. Aizpurua, Phys. Rev. B **74**, 195339 (2006).

[58] S. Schulz, S. Schumacher, and G. Czycholl, Phys. Rev. B **73**, 245327 (2006).

[59] J. M. Luttinger, Phys. Rev. **102**, 1030 (1956).

[60] E. O. Kane, J. Phys. Chem. Sol **1**, 249 (1957).

[61] C. R. Pidgeon and R. N. Brown, Phys. Rev. **146**, 575 (1966).

[62] P. Pfeffer and W. Zawadzki, Phys. Rev. B **41**, 1561 (1990).

[63] S. Richard, F. Aniel, and G. Fishman, Phys. Rev. B **72**, 245316 (2005).

[64] R. Eppenga, M. F. H. Schuurmans, and S. Colak, Phys. Rev. B **36**, 1554 (1987).

[65] G. Bastard, Phys. Rev. B **24**, 5693 (1981).

[66] G. Bastard and J. A. Brum, IEEE J. Quantum Electron. **22**, 1625 (1986).

[67] M. G. Burt, J. Phys.: Condens. Matter **4**, 6651 (1992).

[68] M. G. Burt, J. Phys.: Condens. Matter **11**, R53 (1999).

[69] V. Mlinar, *Origins of scale invariance in growth processes*, PhD thesis, Universiteit Antwerpen, 2007, available online on *http://www.cmt.ua.ac.be/thesis/mlinar.pdf*.

[70] P. N. Keating, Phys. Rev. **145**, 637 (1966).

[71] R. M. Martin, Phys. Rev. B **1**, 4005 (1970).

[72] H. Jiang and J. Singh, Phys. Rev. B **56**, 7696 (1997).

[73] O. Stier, M. Grundmann, and D. Bimberg, Phys. Rev. B **59**, 5688 (1999).

[74] A. J. Williamson, L. W. Wang, and A. Zunger, Phys. Rev. B **62**, 12963 (2000).

[75] E. O. Kane, Phys. Rev. B **31**, 7865 (1985).

[76] O. L. Lazarenkova, P. von Allmen, F. Oyafuso, S. Lee, and G. Klimeck, Appl. Phys. Lett. **55**, 4193 (2004).

[77] M. A. Migliorato, A. G. Cullis, M. Fearn, and J. H. Jefferson, Phys. Rev. B **65**, 115316 (2002).

[78] V. Křápek, V. Holý, and J. Humlíček, Strain field in quantum dots, in *WDS'03 Proceedings of Contributed Papers*, p. 581, Praha, 2003.

[79] S. Christiansen, M. Albrecht, H. P. Strunk, and H. J. Maier, Appl. Phys. Lett. **64**, 3617 (1994).

[80] M. Grundmann, O. Stier, and D. Bimberg, Phys. Rev. B **52**, 11969 (1995).

[81] T. Roch, V. Holý, A. Hesse, J. Stangl, T. Fromherz, G. Bauer, T. H. Metzger, and S. Ferrer, Phys. Rev. B **65**, 245324 (2002).

[82] J.-H. Li, V. Holý, M. Meduňa, S. C. Moss, A. G. Norman, A. Mascarenhas, and J. L. Reno, Phys. Rev. B **66**, 115312 (2002).

[83] G. E. Pikus and G. L. Bir, Sov. Phys. – Solid State **1**, 1502 (1960).

[84] G. E. Pikus and G. L. Bir, *Symmetry and strain induced effects in semiconductors* (Wiley, New York, 1974).

[85] A. Schliwa, *Electronic properties of self-organized quantum dots*, PhD thesis, Technische Universität Berlin, 2007.

[86] A. Schliwa, M. Winkelnkemper, and D. Bimberg, Phys. Rev. B, submitted (2007).

[87] M. Governale and C. Unavelli, Phys. Rev. B **58**, 7816 (1998).

[88] C. Pryor and M. Flatté, Phys. Rev. Lett. **96**, 26804 (2006).

[89] V. Mlinar and F. M. Peeters, Microelectronics Journal **37**, 1427 (2006).

[90] K. Wilson, Phys. Rev. D **10**, 2445 (1974).

[91] O. Stier, *Electronic and optical properties of quantum dots and wires*, PhD thesis, Technische Universität Berlin, 2000.

[92] Landolt–Börnstein, *Numerical data and functional relationships in science and technology*, new series, Vol. III/17a (Springer, Berlin, 1982).

[93] J. Humlíček, D. Munzar, K. Navrátil, M. Lorenc, J. Oswald, J. Pangrác, and E. Hulicius, Physica E **13**, 229 (2002).

[94] C. Pryor, Phys. Rev. B **57**, 7190 (1998).

[95] V. Křápek, J. Fikar, and J. Humlíček, Electronic structure and optical properties of inas/gaas quantum dots, in *WDS'04 Proceeding of Contributed Papers*, p. 469, Praha, 2004.

[96] A. Hospodková, V. Křápek, T. Mates, K. Kuldová, J. Pangrác, E. Hulicius, J. Oswald, K. Melichar, J. Humlíček, and T. Šimeček, Journal of Crystal Growth **298**, 570 (2007).

[97] J. Humlíček, V. Křápek, and J. Fikar, in *Proceedings of 27th ICPS*, p. 753, Flagstaff, Arizona, 2004.

[98] M. A. Cusack, P. R. Briddon, and M. Jaros, Phys. Rev. B **56**, 4047 (1997).

[99] P. Harrison, *Quantum wells, wires and dots* (Wiley, Chichester, 2000).

[100] M. Sugawara, N. Hatori, M. Ishida, H. Ebe, Y. Arakawa, T. Akiyama, K. Otsubo, T. Yamamoto, and Y. Nakata, J. Phys. D: Appl. Phys. **38**, 2126 (2005).

[101] V. A. Shchukin, N. N. Ledentsov, and D. Bimberg, *Epitaxy of nanostructures (nanoscience and nanotechnology)* (Springer-Verlag, Berlin, 2004).

[102] H. Eisele, A. Lenz, C. Henning, R. Timm, M. Ternes, , and M. Dähne, J. Cryst. Growth **248**, 322 (2003).

[103] A. E. Zhukov *et al.*, Appl. Phys. Lett. **75**, 1926 (1999).

[104] O. B. Shchekin, G. Park, D. L. Huffaker, and D. G. Deepe, Appl. Phys. Lett. **77**, 466 (2000).

[105] J. Oswald, E. Hulicius, V. Vorlíček, J. Pangrác, K. Melichar, and T. Šimeček, Thin Sol. Films **336**, 80 (1998).

[106] J. Oswald, K.Kuldová, J. Zeman, E. Hulicius, S. Julian, and M. Potemski, Mat. Sci. Eng. B **69/70**, 318 (2000).

[107] K. Kuldová, J. Oswald, J. Zeman, E. Hulicius, J. Pangrác, K. Melichar, and T. Šimeček, Mat. Sci. Eng. B **88**, 247 (2002).

[108] E. C. Le Ru, P. Howe, T. S. Jones, and R. Murray, Phys. Rev. B **67**, 165303 (2003).

[109] S. Taddei, M. Colocci, A. Vinattieri, F. Bogani, S. Franchi, P. Frigeri, L. Lazzarini, and G. Salviati, Phys. Rev. B **62**, 10220 (2000).

[110] H. Born, A. R. Goňi, R. Heitz, A. Hoffmann, C. Thomsen, F. Heinrichsdorf, and D. Bimberg, phys. stat. sol. (b) **215**, 313 (1999).

[111] L. Jacak, P. Hawrylak, and A. Wojs, *Quantum dots* (Springer-Verlag, Berlin, 1998).

[112] P. P. Paskov, P. O. Holtz, B. Monemar, J. M. Garcia, W. V. Schoenfeld, and P. M. Petroff, Phys. Rev. B **62**, 7344 (2000).

[113] V. Fock, Z. Phys. **47**, 446 (1928).

[114] C. G. Darwin, Proc. Cambridge Philos. Soc. **27**, 1930 (1930).

[115] E. C. Le Ru, P. Howe, T. S. Jones, and R. Murray, phys. stat. sol. c **0**, 1221 (2003).

[116] H. Y. Liu, M. J. Steer, T. J. Badcock, D. J. Mowbray, M. S. Skolnick, P. Navaretti, K. M. Groom, M. Hopkinson, and R. A. Hogg, Appl. Phys. Lett. **86**, 143108 (2005).

[117] M. Bayer, P. Hawrylak, K. Hinzer, S. Fafard, M. Korkusinski, Z. R. Wasilewski, O. Stern, and A. Forchel, Science **291**, 451 (2001).

[118] H. J. Krenner, M. Sabathil, E. C. Clark, A. Kress, D. Schuh, M. Bichler, G. Abstreiter, and J. J. Finley, Phys. Rev. Lett. **94**, 057402 (2005).

[119] W. Sheng and J. P. Leburton, Phys. Rev. B **67**, 125308 (2003).

[120] M. Bayer *et al.*, Phys. Rev. B **65**, 195315 (2002).

[121] A. Babinski, S. Awirothananon, J. Lapointe, Z. Wasilewski, S. Raymond, and M. Potemski, Physica E **26**, 190 (2005).

[122] A. Babinski, G. Ortner, S. Raymond, M. Potemski, M. Bayer, W. Sheng, P. Hawrylak, Z. Wasilewski, S. Fafard, and A. Forchel, Phys. Rev. B **74**, 075310 (2006).

[123] A. Babinski, M. Potemski, S. Raymond, J. Lapointe, and Z. R. Wasilewski, Phys. Rev. B **74**, 155301 (2006).

[124] M. Grundmann, *Nano-Optoelectronics* (Springer, Berlin, 2000).

[125] P. Werner, K. Scheerschmidt, N. D. Zakharov, R. Hillebrand, M. Grundmann, and R. Schneider, Cryst. Res. Technol. **35**, 759 (2000).

[126] M. C. Xu, Y. Temko, T. Suzuki, and K. Jacobi, Phys. Rev. B **71**, 075314 (2005).

[127] P. Offermans, P. M. Koenraad, R. Nötzel, and J. H. Wolter, Appl. Phys. Lett. **87**, 111903 (2005).

[128] D. M. Bruls, P. M. Koenraad, H. W. M. Salemink, J. H. Wolter, M. Hopkinson, and M. S. Skolnick, Appl. Phys. Lett. **82**, 3758 (2003).

[129] Q. Gong, P. Offermans, R. Nötzel, P. M. Koenraad, and J. H. Wolter, Appl. Phys. Lett. **85**, 5697 (2004).

[130] B. Ilahi, L. Sfaxi, G. Bremond, M. Senes, X. Marie, and H.Maaref, Eur. Phys. J. Appl. Phys. **30**, 101 (2005).

[131] T. Yang, S. Tsukamoto, J. Tatebayashi, M. Nishioka, and Y. Arakawa, Appl. Phys. Lett. **85**, 2753 (2004).

[132] T. Chung, G. Walter, and N. Holonyak, Appl. Phys. Lett. **97**, 053510 (2005).

[133] G. Costantini, A. Rastelli, C. Manzano, P. Acosta-Diaz, G. Katsaros, R. Songmuang, O. G. Schmidt, H. v. Känel, and K. Kern, J. Cryst. Growth **278**, 38 (2005).

[134] G. B. Stringfellow, *Organometallic Vapor-Phase Epitaxy: Theory and Practice* (Academic Press, San Diego, 1989), p. 204.

[135] J. Maes, M. Hayne, V. V. Moshchalkov, A. Patane, M. Henini, L. Eaves, and P. C. Main, Appl. Phys. Lett. **81**, 1480 (2002).

[136] S. Godefroo, J. Maes, M. Hayne, V. V. Moshchalkov, M. Henini, F. Pulizzi, A. Patane, and L. Eaves, J. Appl. Phys. **96**, 2535 (2004).

[137] C. Cornet, C. Levallois, P. Caroff, H. Folliot, C. Labbe, J. Even, A. L. Corre, S. Loualiche, M. Hayne, and V. V. Moshchalkov, Appl. Phys. Lett. **87**, 233111 (2005).

[138] V. D. Kulakovskii, G. Bacher, R. Weigand, T. Kümmell, A. Forchel, E. Borovitskaya, K. Leonardi, and D. Hommel, Phys. Rev. Lett. **82**, 1780 (1999).

[139] D. Smirnov, S. Raymond, S. Studenikin, A. Babinski, J. Leotin, P. Frings, M. Potemski, and A. Sachrajda, Physica B **346**, 432 (2004).

[140] A. Wojs and P. Hawrylak, Phys. Rev. B **53**, 10841 (1996).

[141] V. Křápek, K. Kuldová, J. Oswald, A. Hospodková, E. Hulicius, and J. Humlíček, Electron states and magnetophotoluminescence of elongated of inas/gaas quantum dots, in *Proceedings of 28th ICPS*, p. 901, Wien, 2006.

[142] S. Awirothananon, W. D. Sheng, A. Babinski, S. Studenikin, S. Raymond, A. Sachrajda, M. Potemski, S. Fafard, G. Ortner, and M. Bayer, Jap. J. Appl. Phys. **43**, 2088 (2004).

[143] A. Wojs, P. Hawrylak, S. Fafard, and L. Jacak, Phys. Rev. B **54**, 5604 (1996).

[144] M. Bayer, A. Kuther, A. Forchel, A. Gorbunov, V. B. Timofeev, J. P. R. F. Schäfer, T. L. Reinecke, and S. N. Walck, Phys. Rev. Lett. **82**, 1748 (1999).

[145] A. R. Goñi, H. Born, R. Heitz, A. Hoffmann, C. Thomsen, F. Heinrichsdorff, and D. Bimberg, Jpn. J. Appl. Phys. **39**, 3907 (2000).

[146] V. Křápek, A. Schliwa, and D. Bimberg, Acta Physica Polonica A **112**, 339 (2007).

[147] V. Křápek, A. Schliwa, and D. Bimberg, Physica E, accepted.

[148] V. Mlinar, A. Schliwa, D. Bimberg, and F. M. Peeters, Phys. Rev. B **75**, 205308 (2007).

[149] G. Bester and A. Zunger, Phys. Rev. B **71**, 045318 (2005).

[150] R. Seguin, A. Schliwa, S. Rodt, K. Pötschke, U. W. Pohl, and D. Bimberg, Phys. Rev. Lett. **95**, 257402 (2005).

[151] F. Ding, L. Wang, S. Kiravittaya, E. Müller, A. Rastelli, and O. G. Schmidt, Appl. Phys. Lett. **90**, 173104 (2007).

List of publications

regular papers

1. O. Caha, V. Křápek, V. Holý, S. C. Moss, J.-H. Li, A. Norman, A. Mascarenhas, J. L. Reno, J. Stangl, and M. Meduňa, *X-ray diffraction on laterally modulated InAs/-AlAs short-period superlattices*, J. Appl. Phys. **96**, 4833 (2004).

2. K. Kuldová, V. Křápek, A. Hospodková, J. Oswald, J. Pangrác, K. Melichar, E. Hulicius, M. Potemski, and J. Humlíček, *1.3 μm emission from InAs/GaAs quantum dots*, phys. stat. sol. c **3**, 3811 (2006).

3. K. Kuldová, V. Křápek, A. Hospodková, O. Bonaventurová Zrzavecká, J. Oswald, E. Hulicius, and J. Humlíček, *Photoluminescence and magnetophotoluminescence of circular and elliptical InAs/GaAs quantum dots*, Mat. Sci. Eng. C **26**, 983 (2006).

4. V. Křápek, K. Kuldová, J. Oswald, A. Hospodková, E. Hulicius, and J. Humlíček, *Elongation of InAs/GaAs quantum dots from magnetophotoluminescence measurements*, Appl. Phys. Lett. **89**, 3108 (2006).

5. A. Hospodková, V. Křápek, K. Kuldová, J. Humlíček, E. Hulicius, J. Oswald, J. Pangrác, and J. Zeman, *Photoluminescence and magnetophotoluminescence of vertically stacked InAs/GaAs quantum dot structures*, Physica E **36**, 106 (2007).

6. A. Hospodková, V. Křápek, T. Mates, K. Kuldová, J. Pangrác, E. Hulicius, J. Oswald, K. Melichar, J. Humlíček, and T. Šimeček, *Lateral-shape of InAs/GaAs quantum dots in vertically correlated structures*, J. Cryst. Growth **298**, 570 (2005).

7. V. Křápek, A. Schliwa, and D. Bimberg, *Determination of quantum dot morphology from magnetooptical properties*, Acta Physica Polonica A **112**, 339 (2007).

8. V. Křápek, A. Schliwa, and D. Bimberg, *Magnetooptical properties of quantum dots: influence of the piezoelectric field*, Physica E, accepted.

reviewed conference proceedings

1. V. Křápek, V. Holý, and J. Humlíček *Strain field in quantum dots*, in WDS'03 Proceedings of Contributed Papers, Praha, 581 (2003).

2. J. Humlíček and V. Křápek, *Infrared response of heavily doped p-type Si and SiGe alloys from ellipsometric measurements*, in Proceedings of 27th ICPS, Flagstaff, 113 (2004).

3. J. Humlíček, V. Křápek, and J. Fikar, *Anisotropy of absorption and luminescence of multilayer InAs/GaAs quantum dots*, in Proceedings of 27th ICPS, Flagstaff, 753 (2004).

4. V. Křápek, J. Fikar, and J. Humlíček, *Electronic structure and optical properties of InAs/GaAs quantum dots*, in WDS'04 Proceedings of Contributed Papers, Praha, 469 (2004).

5. V. Křápek, K. Kuldová, J. Oswald, A. Hospodková, E. Hulicius, and J. Humlíček, *Electron states and magnetophotoluminescence of elongated of InAs/GaAs quantum dots*, in Proceedings of 28th ICPS, Vienna, 901 (2006).

6. A. Hospodková, V. Křápek, T. Mates, K. Kuldová, J. Pangrác, E. Hulicius, J. Oswald, K. Melichar, J. Humlíček, and T. Šimeček, *Lateral shape of InAs/GaAs quantum dots in vertically correlated structures*, in Proceedings of 13th ICMOVPE, Miyazaki, 499 (2006)

Conference presentations

1. V. Křápek, *Calculations of strain field in quantum dots*, 32th International School on the Physics of Semiconducting Compounds, Jaszowiec (Poland), 2003 (poster).

2. V. Křápek, *Strain field in quantum dots*, 12th Week of Doctoral Students, Praha, 2003 (talk).

3. V. Křápek, J. Humlíček, and J. Fikar, *Electronic structure and optical properties of quantum dots*, 13th Week of Doctoral Students, Praha, 2004 (talk).

4. V. Křápek, A. Hospodková, K. Kuldová, and J. Humlíček, *Elektronová struktura InAs/-GaAs kvantových teček (in czech)*, 2nd Workshop of Czech Nano-Team, Brno, 2004 (talk).

5. V. Křápek, K. Kuldová, A. Hospodková, O. Bonaventurová Zrzavecká, J. Fikar, and J. Humlíček, *Correlation of structural and optical properties of InAs quantum dots*, 34th International School on the Physics of Semiconducting Compounds, Jaszowiec (Poland), 2005 (poster).

6. K. Kuldová, V. Křápek, A. Hospodková, J. Oswald, J. Pangrác, K. Melichar, E. Hulicius, J. Humlíček *1.3 μm emission from InAs/GaAs quantum dots*, 4th International Conference on Quantum Dots, Chamonix-Mont Blanc (France), 2006 (poster).

7. V. Křápek, K. Kuldová, J. Oswald, A. Hospodková, E. Hulicius, and J. Humlíček, *Electron states and magnetophotoluminescence of elongated InAs/GaAs quantum dots*, 35th International School on the Physics of Semiconducting Compounds, Jaszowiec (Poland), 2006 (poster).

8. V. Křápek, K. Kuldová, J. Oswald, A. Hospodková, E. Hulicius, and J. Humlíček, *Laterální protažení InAs/GaAs kvantových teček určené pomocí magnetoluminiscence (in czech)*, Optická konference, Brno, 2006 (talk).

9. V. Křápek, K. Kuldová, J. Oswald, A. Hospodková, M. Potemski, E. Hulicius, and J. Humlíček, *Electron states and magnetophotoluminescence of elongated InAs/GaAs quantum dots*, 28th International Conference on the Physics of Semiconductors, Vienna, 2006 (poster).

10. V. Křápek, A. Schliwa, and D. Bimberg, *Interrelation of structural and magnetooptical properties of InAs/GaAs quantum dots*, 36th International School on the Physics of Semiconducting Compounds, Jaszowiec (Poland), 2007 (talk).

11. V. Křápek, A. Schliwa, and D. Bimberg, *Determination of quantum dot morphology from magnetooptical properties*, 17th International Conference on Electronic Properties of Two-Dimensional Systems, Genoa (Italy), 2007 (poster).

12. V. Křápek, K. Kuldová, J. Oswald, A. Hospodková, M. Potemski, A. Schliwa, D. Bimberg, E. Hulicius, J. Humlíček, *Lateral elongation of InAs/GaAs quantum dots determined from magnetoluminescence*, International School Magnetic Fields for Science, Cargese (France), 2007 (talk).